D I S S E R T A T I O N

Electromigration Modeling and Simulation

ausgeführt zum Zwecke der Erlangung des akademischen Grades
eines Doktors der technischen Wissenschaften

eingereicht an der Technischen Universität Wien
Fakultät für Elektrotechnik und Informationstechnik
von

Roberto Lacerda de Orio

Gerlgasse 21/15
A-1030 Wien, Österreich

Matr. Nr. 0627674
geboren am 24. April 1981 in São Paulo, Brasilien

Wien, im Juni 2010

To my parents, José Alberto and Maria Alice.
To my beloved wife, Anita, and little Clara, who
is just about to come.

Acknowledgment

I would like to express my gratitude to Prof. Siegfried Selberherr for the opportunity to study for a doctorate under his supervision, for his guidance, and all support throughout my work. I am grateful for his friendship and willingness to always make my life in Vienna easier.

I would like to thank Dr. Hajdin Ceric for his constant support, instructive suggestions, and interesting discussions during this work, and also, for always helping me with personal matters during this period, mainly when I first arrived in Austria.

I acknowledge all colleagues of the Institute for Microelectronics for the cooperation. In particular Thomas, Otmar, and Karli for the very nice discussions, help with the "get used to Austrian life", and German lessons.

I thank the staff of the Institute for Microelectronics for keeping a perfect environment of work. In particular Cerv, who has been always ready to fix all problems with my computer.

I am grateful to Prof. Jacobus W. Swart, who has been responsible for my first steps regarding scientific work.

I would like to thank my family for the continuous support during all the years of my study and for all efforts which allowed me to be where I am.

Finally, a special thanks to Anita, my beloved wife and best friend, for being always by my side. Without her support and encouragement everything would have been much harder.

Kurzfassung

Der durch Elektromigration verursachte Ausfall von Bauteilen ist eines der größten Probleme bei Zuverlässigkeitfragen in der Mikroelektronik. Die fortwährende Miniaturisierung der Verdrahtungsstrukturen führt zu größeren Stromdichten und höheren Temperaturen, welche schlussendlich einen elektromigrationsbedingten Ausfall einleiten. Als Folge dessen stellt die Elektromigration nach wie vor eine Herausforderung für die Entwicklung neuer Technologiestufen dar.

Mathematische Modellierung kann wesentlich zum Verständnis der durch Elektromigration bedingten Versagensmechanismen beitragen. Sie dient als wichtiges Werkzeug zur Erklärung verschiedener experimenteller Beobachtungen und bildet letztlich eine solide Grundlage für den Entwurf und die Herstellung zuverlässigerer Metallisierungen. Der Fokus dieser Arbeit liegt in der Entwicklung eines für numerische Simulationen geeigneten, vollständig dreidimensionalen Elektromigrationsmodells. Zur Erfüllung dieser Aufgabe wird eine detaillierte Studie früherer Modelle durchgeführt und deren wichtigsten Stärken und Schwächen werden identifiziert. Basierend auf dieser Studie ist ein vollständiges Modell entwickelt worden, das den elektromigrationsbedingten Materialtransport mit elektrothermischen und mechanischen Fragestellungen in einem allgemeinen Rahmen verbindet. Material- und Korngrenzen werden dabei als unabhängige Pfade hoher Diffusivität behandelt. Eine sorgfältige Analyse der Fehlstellendynamik an Korngrenzen wird durchgeführt und ein neues Modell für Korngrenzen vorgeschlagen. Die Modellgleichungen werden mit Hilfe der Finiten Elemente Methode numerisch gelöst. Die Diskretisierung wird detailliert erläutert und die Softwareimplementierung des zugehörigen Systems algebraischer Gleichungen in systematischer Weise beschrieben.

Elektromigration wird für realistische, dreidimensionale Dual-Damascene-Verdrahtungsstrukturen aus Kupfer simuliert. Zuerst wird die Korrektheit der Implementierung durch Vergleich der Simulationsergebnisse mit den zur Verfügung stehenden analytischen Lösungen sichergestellt. Danach werden die Auswirkungen mechanischer Belastung auf den durch Elektromigration hervorgerufenen Materialtransport präsentiert und deren Einfluss auf die extrapolierte Lebensdauer diskutiert. Zusätzlich hat auch die Mikrostruktur große Auswirkungen auf die elektromigrationsbedingte Verteilung der Bauteillebensdauer, weshalb diese Abhängigkeit ebenfalls analysiert wird. Schließlich werden mehrere Simulationen durchgeführt, um die statistischen Eigenschaften der Lebensdauerverteilung als Funktion der Kupferkorngröße zu erhalten. Dabei stellt sich heraus, dass die Berücksichtigung der Pfade hoher Diffusivität und der Mikrostruktur im Rahmen der Modellierung eine signifikante Verbesserung der Modellqualität erlaubt. Die Simulationsergebnisse zeigen, dass das vorgeschlagene Modell in der Lage ist, einige der häufigsten experimentellen Beobachtungen der elektromigrationsbedingten Materialverarmung zu erklären und zu reproduzieren, was die Vorhersagequalität des entwickelten Werkzeugs untermauert.

Abstract

Electromigration induced failure is one of the main reliability issues for the microelectronics industry. The continuous scaling of the interconnect dimensions leads to higher operating current densities and temperatures, which accentuates the electromigration failure. As a consequence, electromigration still poses challenges for the development of the new technological nodes.

Mathematical modeling can significantly contribute to the understanding of the electromigration failure mechanisms. It has become an important tool for explaining several experimental observations and, ultimately, can provide a stronger basis for design and fabrication of reliable metallizations. In the scope of this work the focus is put on the development of a fully three-dimensional electromigration model which is suitable for numerical simulations. To accomplish this task, a detailed study of previous models is carried out, and their main strengths and shortcomings are identified. Based on this study, a complete model which connects electromigration induced material transport with the electro-themal and the mechanical problem in a general framework has been developed. Material interfaces and grain boundaries are treated as independent fast diffusivity paths. A careful analysis of the vacancy dynamics in grain boundaries is performed, and a new grain boundary model is proposed. The model equations are numerically solved using the finite element method. Their discretization is presented in detail, and the implementation of the corresponding system of algebraic equations in a software tool is described in a systematic way.

Electromigration simulations are carried out in realistic three-dimensional copper dual-damascene interconnect structures. The correctness of the implementation is verified by comparing the simulation results with the available analytical solutions. The effect of mechanical stress on electromigration induced material transport is presented, and its impact on the lifetime extrapolation is discussed. Since the microstructure has a major influence on the electromigration failure, its effect on the electromigration lifetimes' distribution is analyzed. Several simulations are carried out in order to obtain the statistical properties of the electromigration lifetimes as a function of the the copper grain size statistics. The introduction of fast diffusivity paths and microstructure into the modeling framework represents a significant improvement of the model capabilities. The simulations results show that the proposed model is able to explain and reproduce some of the most common experimental observations of electromigration induced voiding, and demonstrate the predictive capability of the developed tool.

Resumo

As falhas causadas por eletromigração são um dos principais problemas de confiabilidade para a indústria de microeletrônica. A contínua redução das dimensões das interconexões resulta em elevadas densidades de corrente e temperaturas de operação, acentuando a ocorrência de tais falhas. Consequentemente, o fenômeno da eletromigração ainda impõe desafios para o desenvolvimento dos novos nós tecnológicos.

A modelagem matemática pode contribuir de maneira significante para o entendimento dos mecanismos que levam às falhas por eletromigração. Ela tem se tornado uma ferramenta importante para explicar diversas observações experimentais, gerando um nível de conhecimento melhor para o projeto e fabricação de metalizações mais confiáveis. O objetivo deste trabalho é desenvolver um modelo tridimensional de eletromigração apropriado para simulações numéricas. Para alcançar este objetivo, foi realizado um estudo detalhado dos modelos existentes e suas principais vantagens e desvantagens foram identificadas. Baseando-se neste estudo, um modelo completo, o qual conecta o transporte de material devido à eletromigração com os problemas elétrico, térmico e mecânico, foi desenvolvido. As interfaces formadas entre os diferentes materiais e contornos de grão foram independentemente tratadas como regiões de rápida difusão. Além disso, uma análise detalhada da dinâmica das vacâncias nos contornos de grão foi conduzida. Dessa forma, um novo modelo para os contornos de grão foi proposto. As equações do modelo foram resolvidas numericamente usando-se o método dos elementos finitos. A discretização das equações foi apresentada detalhadamente e a implementação do sistema de equações resultante em um software de simulação foi descrita de maneira sistemática.

Simulações tridimensionais de eletromigração foram conduzidas em interconexões que representam de forma satisfatória as interconexões de cobre reais. A implementação foi verificada comparando-se os resultados obtidos através das simulações numéricas com as soluções analíticas existentes. O efeito do estresse mecânico no transporte de material causado pela eletromigração e seu impacto na extrapolação do tempo de vida das interconexões foi discutido. Uma vez que a microestrutura tem grande influência nas falhas devido à eletromigração, o seu efeito na distribuição estatística dos tempos de vida foi analisado. Por isso, várias simulações foram executadas para se obter as propriedades estatísticas dos tempos de vida em função da distribuição estatística dos tamanhos dos grãos de cobre. A introdução das regiões de rápida difusão e da microestrutura representa uma melhoria significativa do modelo. Os resultados das simulações mostram que o modelo proposto é capaz de explicar e reproduzir algumas das observações experimentais mais comuns no que se refere à formação de cavidades e demonstram a capacidade de predição do sofware desenvolvido.

Contents

List of Figures

List of Tables

List of Symbols

B	Bulk modulus
c_p	Specific heat
$\mathbf{C}$	Elasticity tensor
C_a	Atomic concentration
C_L	Concentration of lattice sites
C_v	Vacancy concentration
C_{v0}	Equilibrium vacancy concentration in the absence of stress
C_{veq}	Equilibrium vacancy concentration
C_{im}	Trapped vacancy concentration
$\mathbf{D}$	Vacancy diffusivity tensor
D_a	Atomic diffusion coefficient
D_v	Vacancy diffusion coefficient
D_{v0}	Pre-exponential factor for vacancy diffusivity
e	Elementary charge
E	Young modulus
$\vec{E}$	Electric field
E_a	Activation energy for diffusion
f	Vacancy relaxation factor
G	Vacancy generation/annihilation term
$\vec{j}$	Current density
$\vec{J}_a$	Atomic flux
$\vec{J}_v$	Vacancy flux
k	Boltzmann constant
MTF	Mean time to failure
Q^*	Heat of transport
T	Temperature
$\vec{u}$	Displacement vector
Z^*	Effective valence
α_E	Linear temperature coefficient of the electrical conductivity
α_T	Linear temperature coefficient of the thermal conductivity
β_E	Quadratic temperature coefficient of the electrical conductivity
β_T	Quadratic temperature coefficient of the thermal conductivity

γ_{E0}	Electrical conductivity at room temperature
γ_{T0}	Thermal conductivity at room temperature
α	Thermal expansion coefficient
γ_E	Electrical conductivity
γ_T	Thermal conductivity
δ	Grain boundary/interface width
$\boldsymbol{\varepsilon}$	Total strain
$\boldsymbol{\varepsilon}^e$	Elastic strain
$\boldsymbol{\varepsilon}^v$	Electromigration induced strain
ε^{th}	Thermal strain
μ	Chemical potential
μ_v	Vacancy chemical potential
ν	Poisson ratio
ω_R	Vacancy release rate
ω_T	Vacancy trapping rate
Ω	Atomic volume
Ω_v	Vacancy volume
ρ	Electric resistivity
ρ_m	Material density
$\boldsymbol{\sigma}$	Mechanical stress
σ_{th}	Critical stress for void nucleation
τ	Vacancy relaxation time

Chapter 1

Introduction

When a sufficiently strong electric current passes through an interconnect metal, a diffusive motion of atoms and/or vacancies takes place in a direction along or opposite to the current flow. This phenomenon is called electromigration (EM) [1]. Although it had already been observed, EM became of practical interest in the late 1960's, when semiconductor companies observed EM failures in integrated circuits (ICs). Since then, failure due to EM has been one of the key issues regarding reliability in ICs.

The main goal of device scaling is to increase the operating speed. However, the interconnects pose a significant delay to signal propagation in a chip [2]. Therefore, device scaling should be accompanied by improvements in the interconnect operation. In order to reduce the delay, low interconnect resistance and capacitance is necessary, which demands high conductivity metals and interlayer materials with low permittivity. At the same time, efforts have been made in developing new integration processes and investigating materials which produce adequate characteristics and, ultimately, reduce the EM effect. These factors contributed to the substitution of aluminum as interconnect metal to aluminum–copper alloys, and later to pure copper [3]. Copper has a much higher electrical conductivity than aluminum and, moreover, is more resistant against EM failures. The introduction of copper metallizations posed several challenges which ultimately resulted in the damascene fabrication process [4].

According to the International Technology Roadmap for Semiconductors (ITRS) 2010 [5], the copper dual-damascene technology process will continue to be used for fabrication of on-chip interconnects for the next technological nodes. The metal wiring pitch in integrated logic circuits is $64\,\mathrm{nm}$ for the $32\,\mathrm{nm}$ node, and will be $44\,\mathrm{nm}$ for the $22\,\mathrm{nm}$ node. At the same time, the expected operating current densities can reach $2.11\,\mathrm{MA/cm^2}$ and $2.80\,\mathrm{MA/cm^2}$, respectively.

The interconnect structure is arranged in several levels of metallization with thousands of interlevel connections such as vias, so that the density of on-chip interconnects has increased from generation to generation of modern integrated circuits. This requires a decrease in both interconnect width and thickness and, consequently, the operating current densities increase. Due to the continuous shrinking of interconnect dimensions, high current densities and temperatures are unavoidable. Therefore, electromigration failure is likely to be even more problematic for the next generations of ICs, and the prediction of the long term interconnect behavior is a major necessity.

1.1 Dual-Damascene Fabrication Process

In a damascene process the dielectric is first deposited onto the substrate, which is then patterned and filled by metal deposition. The dual-damascene process is characterized by patterning the vias and trenches, in such a way that the metal deposition fills both at the same time [4, 6]. Figure 1.1 depicts the process steps for fabricating a typical copper dual-damascene interconnect.

First, the dielectric is deposited and patterned using standard lithography and etching techniques to form the via and trench. This is followed by the deposition of a diffusion barrier which is typically a Ta-based layer. The diffusion barrier layer has two major functions. First, it avoids that Cu atoms migrate into the interlevel dielectric (ILD), and second, it provides
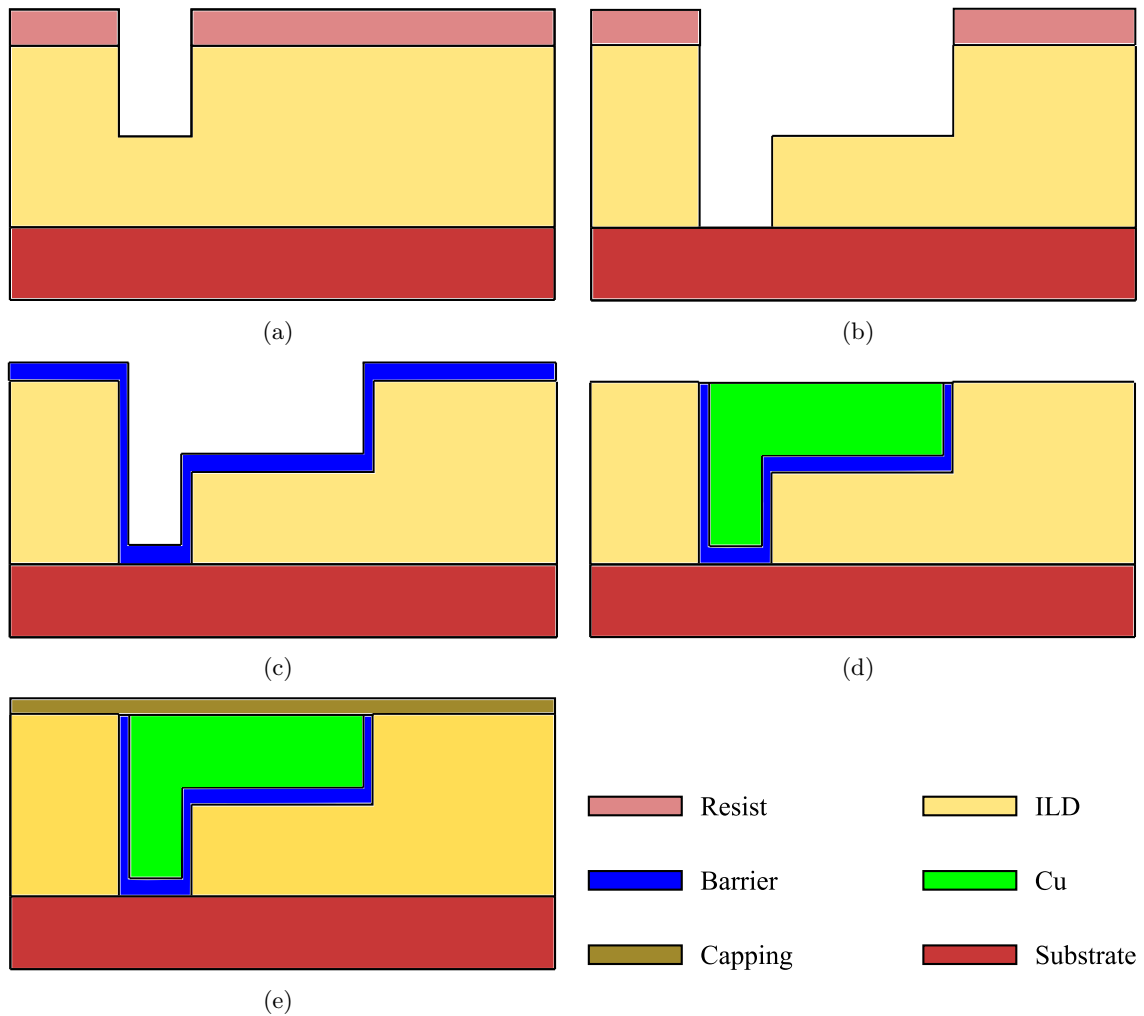
Figure 1.1: Copper dual-damascene fabrication process. (a) Via patterning. (b) Via and trench patterning. (c) Barrier layer deposition and Cu seed deposition. (d) Cu electroplating and excess removal by chemical mechanical polishing. (e) Capping layer deposition.

good adhesion to Cu [6]. After the deposition of the diffusion barrier, a thin Cu seed is deposited by physical vapor deposition (PVD) followed by the electroplating of Cu, which fills the via and trench. The excess Cu is removed by a chemical mechanical polishing process (CMP) and an etch stop layer (also called capping layer), typically SiN based, is deposited. In this way, the complete interconnect structure can be produced by repeating these process steps for each level of metallization.

1.2 The Electromigration Failure

When an electric current passes in a conductor, atoms are driven towards the anode due to the momentum transfer from the electrons to the atoms [1]. Due to the blocking boundary imposed by the barrier layer in Cu dual-damascene lines, there is an accumulation of atoms at the anode side and, at the same time, a depletion at the cathode end. Atom accumulation at the anode leads to the development of a compressive stress, while the depletion of atom at the cathode yields a tensile stress. This stress development can results in two distinct failures. If the compressive stress is sufficiently high and the surrounding dielectrics are weak, metal extrusion may form, causing short circuits [7]. On the other hand, a sufficiently high tensile stress leads to void formation, which can grow and span the line or via, so that the line resistance significantly increases and the interconnect fails [8]. Normally, the critical stress for extrusion formation is larger than that for void formation, and the latter is the dominant failure mechanism.

Electromigration induced failures normally present two distinctive phases. In the first one no electromigration generated voids can be observed in the interconnect and no significant resistance change of the line is detected [9]. This phase lasts until a void is nucleated and is visible in scanning electron microscopy (SEM) pictures. Then, the second phase starts, where the void can evolve in several different ways, until it finally grows to a critical size causing a significant resistance increase or completely severing the interconnect line [10, 11]. Thus, the total electromigration lifetime is the sum of the time for a void to nucleate plus the time for the void to develop.

Figure 1.2 shows two typical failures in a copper dual-damascene line [12]. In the first case the void nucleates right under the via, so that the failure tends to occur soon after nucleation. Thus, the time to failure is dominated by the nucleation period. In turn, if the void nucleates away from the via, the void has first to migrate towards the via, where it then grows to cause the failure. Therefore, the lifetime is dominated by the void evolution phase [12].

Figure 1.3 shows the electromigration lifetime, normalized to the expected lifetime for the $1\,\mu$m technology node, as a function of the interconnect cross sectional area [13, 14]. As the dimensions of the interconnects decrease, the electromigration lifetime also decreases, because the reduction of via and line dimensions requires a smaller critical void to cause the failure [13]. Moreover, as the line width is reduced beyond $100\,$nm, the growth of copper grains during the line fabrication is also reduced, leading to smaller grain sizes [15, 16, 17]. Consequently, the interconnect line changes from a bamboo-like to polycrystalline structure, so that grain boundary diffusion provides an additional path for mass transport [18]. Another contribution for shorter electromigration lifetimes comes from the introduction of low-k interlevel dielectrics [2, 12].

(a)

(b)
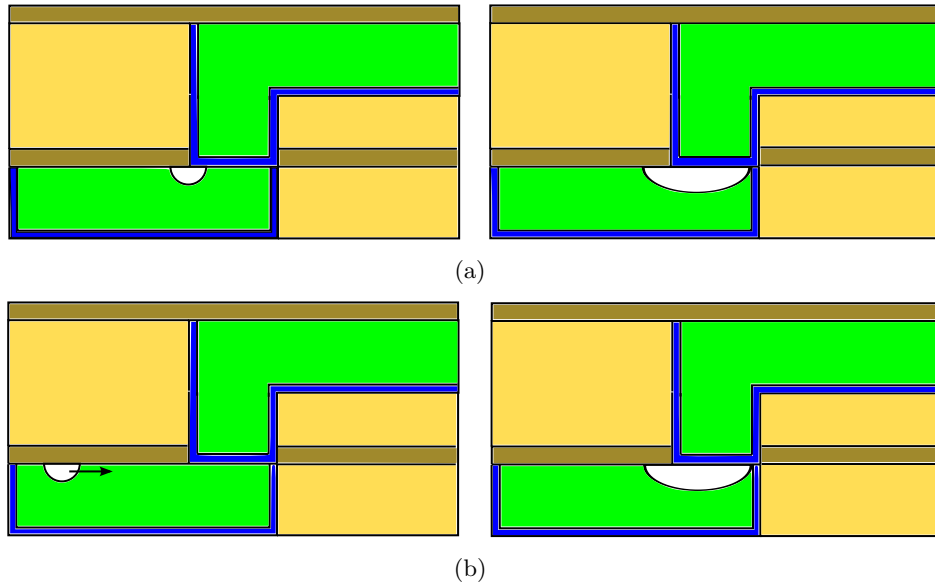
Figure 1.2: Failures in a damascene line. (a) Failure dominated by the void nucleation phase. (b) Failure dominated by void nucleation migration and growth.
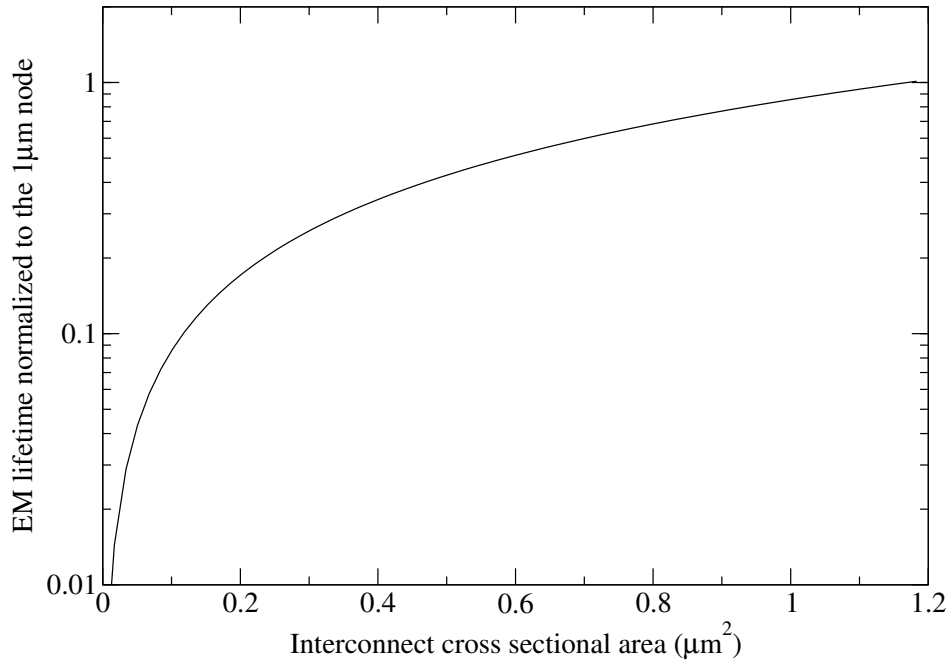
Figure 1.3: EM lifetime variation as a function of the interconnect dimensions. This curve is calculated based on equation (1.13).

1.2.1 Experimental Lifetime Estimation

EM tests are carried out using simple structures and stress conditions which accelerate the EM failure. This can be performed by stressing an interconnect line at significantly higher current density and temperature than those found at use condition. Typically, current densities in the order of 1 to 10 MA/cm^2 are used, and the test temperature lies in the range from 170 to 350 °C [19]. Under such conditions, interconnect failure is obtained much faster than it would be possible at use conditions. An important issue here is that the results from the EM experiments have to be related to the real operating conditions, which means that the lifetimes obtained from the accelerated tests have to be extrapolated to the use conditions. In addition, only a limited number of interconnect structures are tested, whereas often hundreds of millions of interconnects exist on a chip. Therefore, the extrapolation needs to take into account, how to assess on-chip reliability from the EM sample structures.

In copper interconnects EM failures are primarily caused by void growth at the cathode end of the line [20]. As the void grows, the electric current is forced to pass through the highly resistive barrier layer, which leads to an increase of the line resistance. When this increase reaches a given threshold value, the line is considered to have failed. In this way, the EM lifetime of a given interconnect structure is determined by monitoring its resistance change.

Due to the statistical character of EM lifetimes, it is necessary to carry out EM experiments on a number of test structures. The lifetimes obtained from these experiments are statistically analyzed and regularly presented in probability plots following a certain distribution which is characterized by a mean time to failure (MTF) and standard deviation (σ) [21].

EM lifetimes are normally described using a lognormal distribution [22]. However, it has been discussed whether this choice is the most appropriate one [23], and it is argued that EM lifetimes are more correctly described by a multi-lognormal distribution. This has been recently confirmed by several EM experiments [8, 24, 25]. It should be pointed out that the understanding of the electromigration lifetime distribution is crucial for the extrapolation of the times to failure obtained empirically from accelerated tests to real operating conditions, as performed by a modified form of the Black equation [19, 22].

1.2.2 The Impact of Material Interfaces

As show in Figure 1.1, the copper line is completely embedded in a barrier layer and in a capping layer in the dual-damascene technology. EM tests have shown that the quality of these interfaces is of crucial importance for the EM lifetimes [26, 27, 28, 29]. Therefore, since the introduction of copper interconnects, their surface and interface EM properties have been extensively studied.

The adhesion between the copper and the surrounding layers is significantly influenced by the choice of processes and materials, so that several combinations have been investigated [30]. Good adhesion is characterized by a tightly bonded interface, which reduces the diffusion along this path and, consequently, increases EM lifetimes. In contrast, the weak bonding between the copper and surrounding layers forms a poorly adhering interface, which leads to

higher diffusivities. This increases material transport prior to void nucleation and also speeds-up void evolution and growth, resulting in shorter EM lifetimes. Moreover, the critical stress for void nucleation can be significantly lower at sites of weak adhesion.

The interface between copper and the capping layer is considered to be the dominant diffusivity path in dual-damascene interconnects. This has been confirmed by *in situ* SEM experiments which have shown that void nucleation, migration, and growth occur mainly along the copper/capping layer interface [31, 32, 33]. The properties of this particular interface play, therefore, a key role for the electromigration failure.

SiN and SiC based films are widely used as capping materials for copper interconnects. One of the major tasks during process development is to find capping layer materials, as well as pre-clean and deposition techniques that yield good interface adhesion to obtain adequate EM performance. Recently, Zschech *et al.* showed that the bonding strength of the copper/capping layer interface can be increased by using a metallic coating, such as CoWP, before the SiN capping layer deposition [28]. For such a structure they measured an EM activation energy of $1.9 - 2.4$ eV, which is much higher than the $0.9 - 1.2$ eV typically obtained for the standard SiN capping layers. This significant reduction in material transport, and also reduced void growth rates, is explained by a Cu/CoWP interface presenting an epitaxy-like transition (i.e. non-interrupted array of parallel lattice planes) between the copper and the capping layer, formed by metallic Cu-Co bonding and a highly ordered interface. Similar results were obtained by Yan *et al.* using Cu_3Sn coatings [27].

Strengthening the copper/capping layer interface is especially valuable in narrow lines, where due to the bamboo copper grain structure the activation energy for failure is close to the bulk value. This results in a very large EM lifetime. However, as the copper grain size decreases with the line width beyond the 65 nm node, and the lines present again polycrystalline structure, grain boundary diffusion becomes more important and is likely to dominate the failure mechanism [18].

Regarding the barrier layer, tantalum is the most commonly used material. A good adhesion has been observed between copper and tantalum, so that a high activation energy, about 2.1 eV has been reported [19]. Nevertheless, some works have found relatively low activation energies, approximately 1.0 eV, for this interface [13, 34]. This can be explained by the oxidation of the copper surface, so that the adhesion between the oxidized copper and tantalum layer is reduced, becoming a path for rapid diffusion.

From these observations, one can see that the quality of interfaces in copper interconnects is very sensitive to process variations. Any oxygen which is allowed to diffuse to the copper surface will reduce the adhesion and lead to increased diffusion, consequently, reducing the EM lifetime. Poor cleaning practice prior to the application of the capping layer has also been found to degrade the interconnect lifetime [35].

1.2.3   Effect of Microstructure

The microstructure of conductor lines depends on many parameters, such as the core material deposition technique, the barrier layer material and its deposition technique, the copper seed layer deposition technique and thickness, and the line width. As an example, for a given line

width, the grain size may differ significantly, when the copper deposition technique changes from chemical vapor deposition (CVD) to electroplating [36].

In polycrystalline lines the network of grains provides grain boundaries running parallel to the electric current, so that grain boundary diffusion may significantly contribute to material diffusion. Moreover, the microstructure provides grain boundary triple points, which are sites of flux divergence, where voids are seen to nucleate. Grain boundary diffusion was certainly the dominant transport mechanism in Al interconnects. For Cu lines, however, this is not so evident, because diffusion along interfaces appears as the dominant mechanism. Nevertheless, it has been shown that larger Cu grains lead to longer EM lifetimes compared to lines with smaller grains [36].

The microstructure influence on EM failure tends to be reduced as the copper grain sizes are comparable to the line width. In this case, the interconnect presents a bamboo-like structure and, therefore, grain boundaries cannot provide a continuous path for fast diffusion. However, local variations of the microstructure affect Cu diffusivity along the copper/capping layer interface, which dependens on the orientation of individual grains. In this way, the difference in interfacial diffusion of neighboring grains leads to flux divergences located at the intersection of the copper/capping layer interface with the grain boundary formed by these grains.

From the above observation, it is argued that the texture of the line can have a significant impact on the electromigration behavior [37]. It was observed that lines with a stronger (111) texture have longer EM lifetimes [36, 38]. This is attributed to the lower Cu diffusivity at (111) oriented grains in comparison to (100) and (110) surfaces [39]. Moreover, the texture distribution is seen to have an important effect for both void nucleation [40, 41] and evolution [42].

Fayad *et al.*[43] showed that the lognormal standard deviation of EM lifetimes can be explained by the dependence of the diffusion along the copper/capping layer interface on the orientation of the grains. Moreover, copper grain sizes seem to follow lognormal distributions in typical dual-damascene process technology [20]. Therefore, it has been argued that the lognormal distribution of EM lifetimes is related to microstructure features [44].

1.3 Empirical and Semi-Empirical Models

As already mentioned EM lifetimes obtained under accelerated tests have to be extrapolated to operating conditions. This extrapolation has to properly take into account relevant EM physical parameters and, therefore, it is normally carried out based on empirical and semi-empirical expressions.

1.3.1 Black's Equation

Based on a very simple model, Black [45, 46, 47] was the first to derive an expression for the time to failure of a metal line subjected to electromigration. He considered that the mean time to failure, MTF, is inversely proportional to the rate of mass transport, R_m,

$$MTF \propto \frac{1}{R_m}, \tag{1.1}$$

and that the rate of mass transport is proportional to the momentum transfer between thermally activated ions and conducting electrons,

$$R_m \propto n_e \Delta p N_a, \tag{1.2}$$

where n_e is the density of conducting electrons, Δp is the momentum transfer from the electrons to the metal atoms, and N_a is the density of thermally activated ions. Furthermore, assuming that both the electron density as well as the momentum transfer are proportional to the current density, j,

$$n_e \propto j, \ \Delta p \propto j, \tag{1.3}$$

and that the activated ions follow an Arrhenius law

$$N_a \propto \exp\left(-E_a/kT\right), \tag{1.4}$$

the mean time to failure is modeled as

$$MTF = \frac{A}{j^2} \exp\left(\frac{E_a}{kT}\right), \tag{1.5}$$

where A is a constant which comprises the material properties and the geometry of the interconnect [45, 47], E_a is the activation energy, T is the temperature, and k is Boltzmann's constant. It was observed that not all experimental results followed (1.5), but they could be fitted by allowing a variable current density exponent, n, which can be experimentally determined. Therefore, Black's equation was modified to [48]

$$MTF = \frac{A}{j^n} \exp\left(\frac{E_a}{kT}\right). \tag{1.6}$$

It is interesting to note that the original equation (1.5) predicted a failure time proportional to the inverse square of the current density, even though mass transport due to electromigration had been shown to be linearly dependent on the current density [1]. This issue was discussed by several authors [48, 49], however, the explanation for the square dependence was elucidated only several years later, when various theoretical works [50, 51, 52, 53, 54, 55] considerably contributed to a better understanding of the electromigration behavior. An exponent close to 1 indicates that the lifetime is dominated by the void growth mechanisms, i.e. the time for a void to grow and lead to failure represents the major portion of the lifetime [51, 52], while a value close to 2 indicates that void nucleation is the dominant phase of the electromigration lifetime [50, 53, 54, 55].

Since equation (1.6) connects the EM time to failure with the material transport mechanism via the activation energy parameter, and the current density dependence via the exponent n. Thus, these parameters can be experimentally determined from the accelerated tests. Taking the logarithm of (1.6) yields

$$\ln MTF = \ln A - n \ln j + \frac{E_a}{kT}. \tag{1.7}$$

Testing an interconnect at several temperatures, the mean time to failure can be plotted as a function of the temperature, as shown in Figure 1.4(a). For a constant current density,
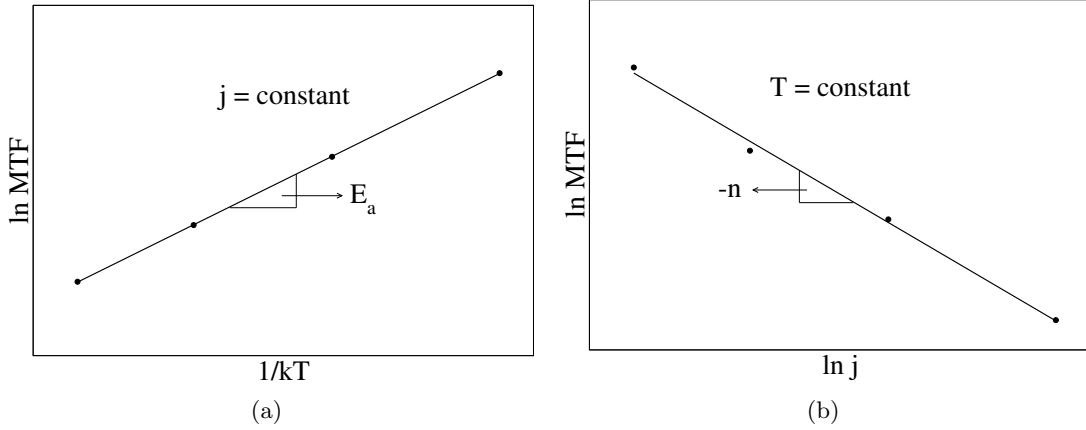
Figure 1.4: Extraction of activation energy and current density exponent from EM tests. (a) Activation energy calculation. (b) Current density exponent determination.

(1.7) shows that the logarithm of the mean time to failure varies linearly with the inverse of temperature, therefore, the activation energy can be extracted from the measurement of the angular coefficient in Figure 1.4(a). The current density exponent n can be determined in a similar way. Varying the current density and keeping the test temperature constant, the coefficient angular of the plot $\ln MTF$ versus $\ln j$ determines the current density exponent, as shown in Figure 1.4(b).

This method of parameter extraction together with equation (1.6) has been used for lifetime estimation and extrapolation to operating conditions for 40 years now. However, in a recent publication Lloyd [56] discussed this application of the modified equation (1.6) and concluded that it may lead to significant errors in the lifetime extrapolation. These errors arise from the assumption that the fitting parameters A, E_a, and n obtained under accelerated tests are also valid at real operating conditions, so that they can be directly applied for the lifetime extrapolation. As Lloyd [56] shows, the experimental determination of the above parameters does not consider important additional temperature and also pre-existing stress dependences, which yields incorrect parameter values and, consequently, lifetime extrapolation.

Black's equation provides useful insight into electromigration failure, however, it does not allow a thorough understanding of the underlying physics related to the electromigration behavior for which more sophisticated physically based models are required.

1.3.2   Resistance Increase and Void Growth

EM experiments normally use a given resistance increase as failure criterion. For a void spanning the entire cross sectional area of a line, the total resistance of a damascene line, as shown in Figure 1.5, is given by

$$R = \frac{\rho_{barrier}\Delta l}{A_{barrier}} + \frac{\rho_{Cu}(L - \Delta l)}{A_{Cu}}, \tag{1.8}$$

where $\rho_{barrier}$ is the electrical resistivity and $A_{barrier}$ is the cross sectional area of the barrier layer, ρ_{Cu} is the electrical resistivity and A_{Cu} is the cross sectional area of the copper line,
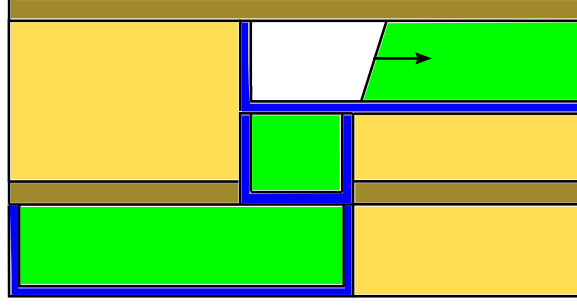
Figure 1.5: Void growth in a single-damascene copper interconnect.

L is the line length, and Δl is the length of the void. Thus, this equation relates resistance increase with void size. In turn, void size is connected to mass transport, which is expressed in the form [57]

$$J_a = C_a v_d = C_a \frac{\delta}{h} \frac{D_a}{kT} Z^* e \rho j, \tag{1.9}$$

where C_a is the atomic concentration, $v_d = \Delta l / \Delta t$ is the drift velocity, δ is the width of the interface which controls mass transport, h is the line height, D_a is the atomic diffusivity of the interface which dominates the EM transport, Z^* is the effective valence, e is the elementary charge, ρ is the electrical resistivity, and j is the current density.

The atomic flux can also be written as [22]

$$J_a = \frac{C_a \Delta V}{A_{Cu} \Delta t}, \tag{1.10}$$

where ΔV is the change of the void volume in a time Δt. Combining (1.9) and (1.10) yields

$$\Delta t = \frac{hkT}{\delta D_a Z^* e \rho j A_{Cu}} \Delta V, \tag{1.11}$$

so that a given test time t is related to the void volume V_{void},

$$t = \frac{hkT}{\delta D_a Z^* e \rho j A_{Cu}} V_{void}. \tag{1.12}$$

Equation (1.12) is commonly used for estimation of the void growth time. In turn, a critical void volume is related to the line resistance according to (1.8). Thus, the time to failure for a given resistance increase criterion can be determined.

An interesting application of such an approach was performed by Hauschildt *et al.* [20, 22]. For a void spanning the entire line width, w, and assuming a rectangular void shape, the void volume becomes $V_{void} = w A_{void}$, and (1.12) yields

$$t = \frac{whkT}{\delta D_a Z^* e \rho j A_{Cu}} A_{void}, \tag{1.13}$$

where A_{void} is the area of the void, which can be measured using SEM pictures. EM tests were then carried out and stopped after a given test time (called t-based by the authors) or

after a certain resistance increase (R-based). In both cases, the void area mean value and standard deviation were determined. For the R-based tests the mean time to failure MTF can be determined which, in turn, can be used for the t-based experiments. Finally, using the void area statistical distribution of both tests and applying (1.13) a new distribution is obtained following [20, 22]

$$t = \frac{A^{R-based}}{A^{t-based}} MTF.$$
(1.14)

Hence, once the statistics of the void area distribution for both test types is known, the distribution of the EM lifetimes can be estimated.

Equation (1.9) is also commonly used to extract the diffusivity from void drift experiments [57]. The drift velocity of the void boundary in Figure 1.5 is

$$v_d = \frac{\delta}{h} \frac{Z^* D_a}{kT} e\rho j = \frac{\Delta l}{\Delta t},$$
(1.15)

which for a given test time t_{test} with a corresponding void length l_{void} can be rearranged as

$$Z^* D_a = \frac{hkT}{\delta e\rho j} \frac{l_{void}}{t_{test}}.$$
(1.16)

Since D_a can be expressed by an Arrhenius relationship, the activation energy for diffusion can be extracted from a plot $\ln(Z^* D_a)$ versus $1/kT$ [38].

1.3.3 EM Lifetime Extrapolation

As already pointed out, the lognormal distribution generally provides a good fit to EM lifetimes [22]. The mean time to failure and the standard deviation of a lognormal distribution are calculated, respectively, by

$$\ln MTF = \frac{1}{N} \sum_{i=1}^{N} \ln TTF_i,$$
(1.17)

and

$$\sigma = \sqrt{\frac{1}{N-1} \sum_{i=1}^{N} (\ln TTF_i - \ln MTF)^2},$$
(1.18)

where TTF_i is the time to failure of the i-th test structure and N is the number of test structures. The cumulative failure frequency of the i-th structure is given by [19]

$$h_i = \frac{i - 0.3}{N + 0.4},$$
(1.19)

which is then sorted in ascending order of failure times and presented in a probability plot.

The probability density function (PDF) of the logonormal distribution has the form

$$PDF(t) = \frac{1}{\sigma t \sqrt{2\pi}} \exp\left[-\frac{(\ln t - \ln MTF)^2}{2\sigma^2}\right],$$
(1.20)

and the corresponding cumulative distribution function CDF,

$$CDF(t) = \int_0^t PDF(\tau)\, d\tau = \Phi\left(\frac{\ln t - \ln MTF}{\sigma}\right), \tag{1.21}$$

which represents the probability of failure until some defined time t. Here, Φ is the integral of the Gaussian function,

$$\Phi(x) = \frac{1}{\sqrt{2\pi}} \int_{-\infty}^x \exp(-\frac{y^2}{2})\, dy. \tag{1.22}$$

The EM lifetime extrapolation from accelerated tests to operating conditions is based on Black's equation (1.6), and is given by [19, 22]

$$TTF_{oper} = MTF_{test} \left(\frac{j_{test}}{j_{oper}}\right)^n \exp\left[\frac{E_a}{k}\left(\frac{1}{T_{oper}} - \frac{1}{T_{test}}\right) + \Phi^{-1}(s)\,\sigma\right], \tag{1.23}$$

where s is the cumulative failure percentage accepted at the real operating condition and Φ^{-1} is the inverse function of Φ. The last term in (1.23) is necessary to extrapolate the 50% cumulative failure of the accelerated test to the very small failure percentiles (about 0.01%) allowed under operating conditions [20].

Note that this extrapolation procedure has an exponential dependence on the standard deviation of accelerated lifetimes, which might dominate the failure extrapolation over the mean time to failure. Therefore, in order to increase the interconnect lifetime at use conditions, it is necessary to increase the mean time to failure as well as to reduce the standard deviation ($\Phi(s)^{-1} < 0$ for very small failure percentiles s).

1.4 TCAD for Electromigration Simulation

Since the late 1960s, several models have been proposed to describe electromigration. Mathematical modeling can significantly contribute to the understanding of EM failure mechanisms. It is an important tool for explaining several experimental observations and, ultimately, it can provide an improved basis for design and fabrication of reliable metallizations. The main problem is that EM is influenced by a wide diversity of physical phenomena and depends on a large number of intrinsic and extrinsic effects. Moreover, the complex interconnect geometries and technological process related features of modern interconnects, such as a typical dual-damascene line, make modeling even more challenging.

Several of the available models are based on simplifying assumptions, so that analytical solutions can be obtained. However, as the development and improvement of different experimental techniques has allowed a deeper analysis of the EM failure, the complexity of the models has gradually increased, in order to be able to reproduce these experimental observations. Such complex models cannot be analytically solved and, therefore, numerical solutions are now required. At the same time, the development of computational methods and resources has allowed to model complex systems and carry out numerical simulations in an efficient way. Thus, the use of TCAD (Technology Computer-Aided Design) tools for EM simulation in interconnect lines has become more popular.

As already mentioned, EM failures can normally be described by a void nucleation and a void evolution phase. Since each of these phases are related to different physical phenomena, it is convenient to treat them separately. A schematic design of such a TCAD tool for EM simulation is then shown in Figure 1.6.
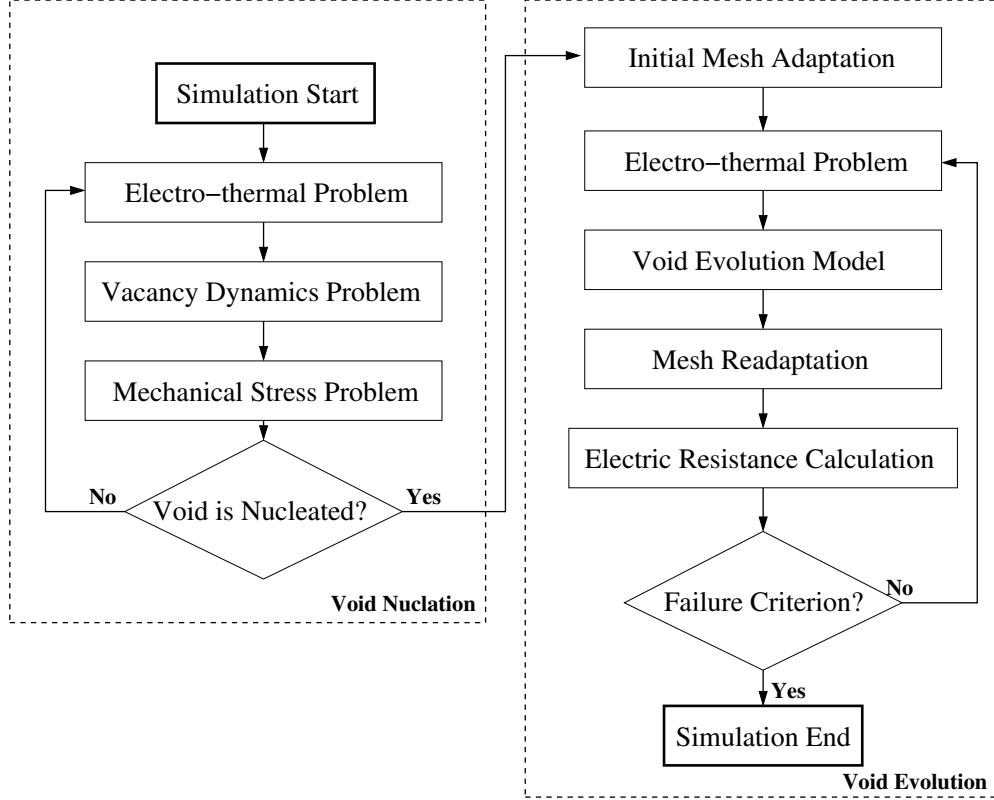
Figure 1.6: Schematic design of a TCAD tool for EM simulation.

1.5   Outline of this Work

In the scope of this work, the focus is put on the development of a fully three-dimensional continuum EM model which is suitable for implementation in a TCAD tool and for numerical simulations. In this way, it is possible to study the EM behavior in realistic three-dimensional interconnect structures. This demands a careful study of the available models, so that their main strengths and, at the same time, their main shortcomings can be identified. Based on this analysis, one is able to extend and further improve these models by taking into account the most relevant effects for EM simulation.

In Chapter 2 the physical phenomena related to electromigration are discussed, starting with a basic derivation of the EM driving force based on a quantum mechanical theory. Next, a general description of the available material transport paths along an interconnect line is given. Then, a detailed analysis of several EM models is presented. First, the simple one-dimensional models are presented, which are followed by more advanced models as

their complexity gradually increases. Then, the void nucleation condition followed by a void evolution model is discussed.

In Chapter 3 the developed EM model is presented. First, the calculation of the electric potential and temperature distribution in an interconnect line is described. This is followed by a discussion of the material transport equations, where emphasis is put on the importance of fast diffusivity paths on the EM induced transport. Also, a detailed derivation of the influence of mechanical stress on the vacancy diffusivity is presented. Next, the connection between EM induced transport and production of mechanical stress is discussed, which is followed by the derivation of a new grain boundary and interface model. The mechanical deformation equations are then presented. Finally, an overview of the complete set of equations, which composes the EM model, is given.

Chapter 4 is devoted to the description of the numerical discretization of the physical model. It starts with the presentation of basic concepts of the finite element method and gives a general formulation for discretization of a three-dimensional domain with tetrahedrons. Then, the numerical discretization of the set of equations which form the EM model derived in Chapter 3 is presented in some detail. This is followed by the description of the TCAD tool developed for EM simulations. Here, the implementation of the algebraic system of equations is described, and all calculations are presented, which are performed during the assembly process of the system of equations for each set of equations composing the model.

In Chapter 5 several simulation studies of electromigration are carried out, starting with the presention of the set of material and simulation parameters which are required in the simulation examples. The developed model and its implementation is verified by simulating the EM transport in a simple interconnect line and comparing it with some of the analytical solution of the models described in Chapter 2. This is then repeated with the inclusion of mechanical stress into the calculations. Next, an original study of the effect of the mechanical stress on the vacancy diffusivity and its effect on the total EM transport is performed. This is followed by a discussion of the importance of fast diffusivity paths regarding the EM failure development. Here, emphasis is put on the role of material interfaces as fast paths for diffusion. Following, the effect of redundant vias in dual-damascene interconnect structures is analyzed. Then, a detail discussion of the impact of the microstructure on EM failure is given.

Finally, conclusions and suggestions for future works are presented in Chapter 6.

Chapter 2

Physics of Electromigration

In this chapter the main physical phenomena related to electromigration are described. First, the electromigration driving force as a result of the action of the "wind force" is derived. Next, the role of the several paths for atomic migration in an interconnect line is discussed and the material transport equations are presented. Several earlier continuum models of electromigration are then described. Here, the impact of mechanical stress is explained. The void nucleation condition is discussed in detail and, finally, the basic void evolution equations and associated numerical methods are briefly presented.

2.1   The Electromigration Driving Force

Electromigration is the atomic migration caused by the action of microscopic forces on mobile defects. These microscopic forces arise due to the local electric field and electron transport in a conductor [58].

Typically, atomic diffusion is a random process, in the sense that there is no preference in the direction of atomic jumps [59]. However, in the process of making an atomic jump, when the atom is in the saddle point and it is out of the lattice equilibrium position, it is subject to a larger electron scattering, in such a way that the momentum transfer from the electron to the atom biases the atomic jump in the direction of the electron flow [60, 61]. The force caused by this momentum transfer from the electron to the atom ion is the so-called "wind force".

Using a semiclassical ballistic model of scattering, Huntington and Grone [1] derived for the wind force

$$\vec{F}_{wind} = -\frac{n\rho_d}{n_d\rho}\frac{m_0}{m^*}e\vec{E}, \tag{2.1}$$

where n is the density of conduction electrons, n_d is the density of defects, ρ_d is the defect resistivity, ρ is the metal resistivity, m_0 and m^* are the free-electron mass and effective electron mass, respectively, e is the elementary charge, and $\vec{E}$ is the macroscopic electric field. Upon deriving this equation, Huntington and Grone [1] assumed that the electrons are scattered by the atomic defects alone and that the defects are decoupled from the lattice. A

more general expression for the wind force is given by quantum mechanics theory [62]

$$\vec{F}_{wind} = -\sum_{\vec{k}} \delta f(\vec{k}) \int |\psi(\vec{k})|^2 \nabla_{\vec{R}} V d\vec{r}, \tag{2.2}$$

where V is the electron-point defect interaction potential and $\psi(\vec{k})$ is the electron scattering wave function for an electron incident upon the defect complex. $\delta f(\vec{k})$ is the perturbed electron distribution function caused by the applied field, which has the form [62]

$$\delta f(\vec{k}) = e\tau \vec{E} \cdot \vec{v} \frac{\partial f(\varepsilon)}{\partial \varepsilon}, \tag{2.3}$$

where τ is the transport relaxation time, $\vec{v} = \hbar \vec{k}/m_0$ is the velocity, and ε is the energy of an electron.

In addition to the wind force, there is a second contribution to the force acting on an atom due to the direct action of the macroscopic electric field on the migration ion, the so-called "direct force" [63]. Therefore, the total driving force acting on a metal ion can be written as the sum of the direct force and the wind force,

$$\vec{F} = \vec{F}_{direct} + \vec{F}_{wind} = (Z_{direct} + Z_{wind})e\vec{E}, \tag{2.4}$$

where Z_{direct} is the direct valence, Z_{wind} is the wind valence. The direct valence Z_{direct} is the nominal valence of the metal, when screening effects are neglected. However, much controversy has appeared, when screening effects are taken into account [63]. In turn, Z_{wind} accounts for the magnitude and direction of the momentum exchange between the conducting electrons and the metal ions.

It is convenient to write equation (2.4) as

$$\vec{F} = Z^* e\vec{E}, \tag{2.5}$$

where $Z^* = (Z_{direct} + Z_{wind})$ is called effective valence. In this way, the microscopic, quantum mechanical effects of the electromigration phenomenon are comprised in the effective valence parameter, which can be theoretically calculated and experimentally measured [1, 61, 62, 64, 65, 66, 67]. Table 2.1 shows the effective valence values for metals commonly used in interconnect structures close to their melting temperature [67].

Table 2.1: Wind and effective valence values.

Metal	Calculated Z_{wind}	Measured Z^*
Al	-3.11	-3.4
Al(Cu)	-5.29	-6.8
Cu	-3.87	-5.0
Ag	-3.51	-8.0
Ta	0.35	-

Using the Nernst-Einstein relation, the drift velocity, $\vec{v_d}$, of metal atoms and the atomic flux due to electromigration are calculated, respectively, by

$$\vec{v_d} = \frac{D_a}{kT}\vec{F} = \frac{D_a}{kT}Z^*e\vec{E}, \tag{2.6}$$

and

$$\vec{J_a} = C_a\vec{v_d} = \frac{D_aC_a}{kT}Z^*e\vec{E} = \frac{D_aC_a}{kT}Z^*e\rho\vec{j}, \tag{2.7}$$

where D_a is the atomic diffusivity, C_a is the atomic concentration, k is Boltzmann's constant, and T is the temperature. The last equality in (2.7) is written in terms of the current density $\vec{j}$, since $\vec{E} = \rho\vec{j}$.

From (2.6) and (2.7) one can see that the sign of the effective valence determines the direction of atomic migration. A negative value means that the atoms diffuse in a direction opposite to the external electric field, or current density, i.e. in the same direction of the electron flow. Also, the mass flow is directly proportional to the current density and to the atomic diffusion coefficient. This means that the total material transport due to electromigration is a function of the available atomic diffusivity paths.

2.2 Diffusivity Paths

There are several possible diffusivity paths in an interconnect line, so the total material transport is determined by the sum of the mass transport taking place along each of these paths. Typically, the material flux through these paths is taken into account by setting an effective diffusion coefficient of the form [4, 21]

$$D_{eff} = D_l + f_{gb}D_{gb} + f_iD_i + f_cD_c, \tag{2.8}$$

where D_{eff} is the effective diffusivity, D_l, D_{gb}, D_i, D_c are the diffusion coefficients for diffusion through the lattice, grain boundary, material interfaces and dislocation cores ("pipe diffusion"), respectively, and f_{gb}, f_i, f_c denote the corresponding fractions of atoms diffusing along these paths.

For a typical dual-damascene interconnect the effective diffusivity is given by [68, 69]

$$D_{eff} = D_l + \delta_{gb}\frac{(w-d)}{wd}D_{gb} + \delta_i\frac{2(w+h)}{wh}D_i + \rho_ca_cD_c, \tag{2.9}$$

where δ_{gb}, δ_i are the grain boundary and interfaces thicknesses, respectively, d is the average grain diameter, ρ_c is the dislocation density, a_c is the cross sectional area of a dislocation core, w is the line width, and h is the line height. The diffusion coefficients are expressed by the Arrhenius law

$$D = D_0 \exp\left(-\frac{E_a}{kT}\right), \tag{2.10}$$

where D_0 is the pre-exponential factor and E_a is the activation energy. From these equations one can see that the effective diffusivity is determined by the dominant diffusion mechanism, i.e. by the fastest diffusivity path. The fastest diffusivity path depends on several factors, like the temperature, the microstructure, and the quality of the interface between the metal and

adjacent layers. Typically, lattice diffusion has the highest activation energy, being the slowest path for mass transport, while the activation energy for diffusion along grain boundaries and interfaces is somewhat lower. In general, surfaces have the lowest values, being the fastest diffusivity paths.

Equation (2.9) allows to examine the relative influence of each path on the material transport due to electromigration. For example, when the linewidth is larger than the grain size, $w > d$, it is expected that grain boundaries form a continuous path in such a way that grain boundary diffusion might significantly contribute to the total mass transport along the line. On the other hand, interfacial diffusion becomes more and more important when the linewidth is less than the average grain size, $w < d$ ("bamboo-like structures"), since there is no continuous path for atomic transport along grain boundaries.

For aluminum based interconnects, the activation energy for grain boundary diffusion is significantly lower than that for interfacial diffusion. This is attributed to the formation of a stable native oxide on the aluminum surface, which reduces the interfacial diffusivity [3]. Thus, for polycrystalline lines diffusion along grain boundaries is expected to be the dominant transport mechanism. For a bamboo-like structure the interfacial diffusion becomes the dominant path, as mentioned above.

In turn, the activation energy for interfacial diffusion in copper seems to be lower than for diffusion along the grain boundary [13, 70]. Consequently, the interface between copper and surrounding layers is the main diffusivity path, for both polycrystalline and bamboo lines. Nevertheless, it has been suggested that there should be a significant contribution of grain boundary diffusion to the total electromigration induced mass transport in copper polycrystalline lines [18, 71]. This may become a key issue for the new technological nodes (32 nm and below), since the copper lines are expected to have polycrystalline structures at such small dimensions [18].

2.3 Electromigration Induced Material Transport

Although electromigration refers to the transport of material caused by the momentum transfer from conducting electrons to metal atoms [1], the total atomic migration is influenced by other physical mechanisms. Electromigration constitutes a diffusion-convection problem, where atomic transport along the interconnect line occurs due to a combination of several driving forces. Since the atomic migration occurs via a vacancy exchange mechanism, the material transport can be, in general, described in terms of vacancies as

$$\vec{J_v} = \frac{D_v C_v}{kT} \left(\nabla \mu_v + |Z^*| e \rho \vec{j} \right). \tag{2.11}$$

$\vec{J_v}$ is the vacancy flux, D_v is the vacancy diffusivity, C_v is the vacancy concentration, and μ_v is the chemical potential of vacancies.

In sites of flux divergence vacancies can accumulate or vanish depending on the sign of the divergence, and the material balance is given by the usual continuity equation

$$\frac{\partial C_v}{\partial t} = -\nabla \cdot \vec{J_v} + G, \tag{2.12}$$

where G represents a generation or annihilation term.

Equations (2.11) and (2.12) are the basic continuum equations which describe the total mass transport along an interconnect line due to electromigration and accompanying driving forces.

The model proposed by Shatzkes and Lloyd [50] was the first that rigorously derived the interconnect lifetime with an inverse square dependence on current density. Considering only the influence of diffusion and electromigration on the vacancy flux, the continuity equation (2.12) along the interconnect length direction can be written as

$$\frac{\partial C_v}{\partial t} = D_v \frac{\partial^2 C_v}{\partial x^2} - \frac{D_v |Z^*| e \rho j}{kT} \frac{\partial C_v}{\partial x}, \tag{2.13}$$

where D_v is the vacancy diffusivity, Z^* is the effective charge number, e is the elementary charge, $\vec{E}$ is the electric field, Q^* is the heat of transport, f is the vacancy relaxation factor, Ω is the atomic volume, σ is the hydrostatic stress, k is Boltzmann's constant, and T is the temperature. Here, the source term $G = 0$ is used.

For a semi-infinite line under the boundary conditions

$$C_v(-\infty, t) = C_{v0} \quad \text{and} \quad J_v(0, t) = 0, \tag{2.14}$$

which means that the vacancy concentration at $x = -\infty$ is fixed at an initial equilibrium value, C_{v0}, and that there is a perfect blocking boundary ($J_v = 0$) at $x = 0$, the solution of (2.13) at the blocking boundary is given by Laplace transformation [50]

$$\frac{C_v(0, t)}{C_{v0}} = 1 + \text{erf}(\beta) + 2 \left\{ \beta^2 [1 + \text{erf}(\beta)] + \frac{\beta}{\sqrt{\pi}} \exp(-\beta^2) \right\}, \tag{2.15}$$

where

$$\beta = \frac{|Z^*| e \rho j}{2kT} \sqrt{D_v t}, \tag{2.16}$$

and

$$\text{erf}(x) = \frac{2}{\sqrt{\pi}} \int_0^x \exp(-x^2) \, dt, \tag{2.17}$$

is the error function.

Assuming that the failure occurs, when the vacancy concentration reaches a given critical value C_{vf} significantly higher than the initial equilibrium value C_{v0}, and that $\beta \gg 0$, then (2.15) is approximated [50] by

$$C_{vf}/C_{v0} \approx 4\beta^2 = \left(\frac{|Z^*| e \rho j}{kT} \right)^2 D_v t_f. \tag{2.18}$$

Since the diffusion coefficient is expressed by the Arrhenius law

$$D_v = D_{v0} \exp\left(-\frac{E_a}{kT} \right), \tag{2.19}$$

where D_{v0} is the pre-exponential factor for vacancy diffusivity, (2.18) yields the mean time to failure of the form

$$MTF = \frac{AT^2}{j^2} \exp\left(\frac{E_a}{kT} \right). \tag{2.20}$$

Note that this equation is similar to the original Black's equation (1.5), except for the multiplying term T^2, and it also predicts a mean time to failure with an inverse square current density dependence. This is a result of the assumption that the failure takes place, when the vacancy concentration reaches a given critical value, which corresponds, in fact, to a void nucleation condition.

A similar model to (2.13) had already been proposed by Rosenberg and Ohring [72] including a source term, so that

$$\frac{\partial C_v}{\partial t} = D_v \frac{\partial^2 C_v}{\partial x^2} - D_v \frac{|Z^*|eE}{kT} \frac{\partial C_v}{\partial x} - \frac{C_v - C_{v0}}{\tau}, \tag{2.21}$$

where C_{v0} is the equilibrium vacancy concentration and τ is the characteristic vacancy relaxation time. The last term of the right-hand side of this equation represents a source function which models vacancy annihilation and generation. It means that vacancies are annihilated, if their concentration is larger than the equilibrium value, or produced, if their concentration is smaller than the equilibrium one. The vacancy relaxation time, τ, characterizes the efficiency of the sites acting as sinks/sources, in such a way that smaller values of τ result in shorter times for the vacancy concentration to reach the steady state condition, and vice versa. As a consequence, high vacancy supersaturation cannot be reached near vacancy sinks, since vacancies are annihilated as soon as the local vacancy concentration becomes higher than its equilibrium value.

The aforementioned models, where material transport only due to gradients of concentration and due to electromigration itself is considered, have two main shortcomings: first, the time scale to reach the steady state vacancy supersaturation lies, at most, in the order of minutes, which is too short compared to the typical failure times. Second, the maximum vacancy supersaturation is very low, in such a way that the energy barrier for void formation would be extremely high. This hinders void formation by means of vacancy condensation and, therefore, a critical vacancy concentration cannot be used to determine the failure of the interconnect. As will be shown in the next sections, these shortcomings can only be resolved with the introduction of mechanical stress in the model equations.

2.4   Electromigration and Mechanical Stress

There are three major sources of mechanical stress in passivated interconnect lines. The first is the thermal stress, resulting from the difference in thermal expansion between the passivation and metal upon cooling from high deposition temperatures. Metalization processing can expose an integrated circuit to temperatures of more than 500 °C. The second source of stress is nonequilibrium film growth. As wafer curvature measurements have shown, this source of stress is even more important than the thermal stress. The third major source of stress is the electromigration itself. Although the measurements significantly contribute to the understanding of thin film stresses, they are, in most cases, limited to simple test structures. Furthermore, the detailed stress distribution within a material cannot be experimentally determined. For the dual-damascene technology high tensile stresses at interfaces, such as in the metal/capping layer interface, are generally critical, and electromigration can either increase or reduce this local tensile stress.

The choice of passivating film material and corresponding process technology causes tensile or compressive stress in the interface between the passivating film and the interconnect metal. Interfacial compressive stress diminishes electromigration along interfaces by reducing the diffusivity [73]. However, numerous experimental observations have shown that tensile stress in the interface increases the possibility of failure [74]. Increased thickness and rigidity of the capping layer prevent relaxation of both thermal and electromigration induced stress, which results in dielectric cracking and metal extrusion.

The evolution of mechanical stress in interconnect lines depends on whether or not vacancies can be created or annihilated such that their equilibrium is maintained. For mechanical stresses to develop, there must be both a volume expansion or contraction of the line with respect to the surrounding material and a mechanical constraint applied by the surrounding material. As atoms exchange place with vacancies and travel towards the anode end of the line, there is a flow of vacancies towards the cathode end. In the absence of vacancy sources and sinks, this would result in a vacancy supersaturation on the cathode end and a deficiency at the anode end. Since there is a small relaxation of the lattice surrounding a vacancy, vacancy accumulation would produce volume contraction at the cathode. In turn, the depletion of vacancies would produce volume expansion at the anode end. However, due to the constraints imposed by the surrounding layers, namely, the capping layer, the barrier layer, and the passivation in copper dual-damascene interconnects, these volumetric changes cannot be accommodated, which results in the development of mechanical stress in the line. At the cathode end tensile stress is produced, while compressive stress develops at the anode end of the line. As will be shown below, this stress gradient acts as an additional driving force for material transport and must be taken into account in the vacancy flux equation. Moreover, mechanical stress is a key parameter for the void nucleation condition.

2.4.1 The Blech Effect

Blech [75, 76, 77] designed an experiment where conductor islands were deposited onto a titanium nitride (TiN) film and stressed at a high current density. As the conductor resistivity was much lower than that of the TiN layer, the conductor stripe would carry most of the current and the resulting movement of the ends of the stripe could be measured. In this way, the electromigration induced drift velocity is determined by

$$v_d = \frac{D_a |Z^*| e \rho j}{kT}. \tag{2.22}$$

Blech observed that only the upstream end (in relation to the electron flow) of the line moved according to (2.22), and that the upstream end stopped moving, when the stripe was reduced to a certain length. Also, he observed that no drift could be detected below a threshold current density.

These observations can be explained by considering the flux due to electromigration and the gradient of the chemical potential via a gradient of mechanical stress [75, 76, 77, 78] according to

$$J_v = \frac{D_v C_v}{kT} \left(|Z^*| e \rho j - \Omega \frac{\partial \sigma}{\partial x} \right), \tag{2.23}$$

where Ω is the atomic volume, and σ is the hydrostatic stress. This equation shows that a gradient of mechanical stress acts as driving force against electromigration. Thus, electromigration stops, when the opposing stress gradient, commonly referred to as "back stress", equals the electromigration driving force, so that $J_v = 0$. This steady-state condition is the so-called "Blech Condition", given by

$$\frac{\partial \sigma}{\partial x} = \frac{|Z^*|e\rho j}{\Omega}. \tag{2.24}$$

Integrating (2.24) over the length of the interconnect line yields

$$\sigma(x) = \sigma_0 + \frac{|Z^*|e\rho j}{\Omega}x, \tag{2.25}$$

where σ_0 is the stress at $x = 0$. This equation shows that the stress varies linearly along the line, when the backflow flux equals the electromigration flux.

Given that the maximum stress the conductor line can withstand is σ_{th}, a critical product for electromigration failure can be stated as

$$(jL)_c = \frac{\Omega(\sigma_{th} - \sigma_0)}{|Z^*|e\rho}. \tag{2.26}$$

This is the so-called "Blech Product". The critical product provides a measure of the interconnect resistance against electromigration failure and several experimental works have reported that the critical product for modern copper interconnects is in the range from 2000 to 10000 A/cm [79, 80, 81, 82].

From the above expression, for a given current density, j, a critical line length can be determined, so that shorter lines will not fail due to electromigration. This is known as "Blech Length", given by

$$l_B = \frac{\Omega(\sigma_{th} - \sigma_0)}{|Z^*|e\rho j}. \tag{2.27}$$

Similarly, for a given line length, L, the maximum current density that can be applied for which electromigration failure does not occur is

$$j_c = \frac{\Omega(\sigma_{th} - \sigma_0)}{|Z^*|e\rho L}. \tag{2.28}$$

An important consequence of the Blech effect is that the jL product during electromigration tests has to be significantly higher than the critical product $(jL)_c$ for the corresponding test structure. Otherwise, the test structure might fail at a later time than it would normally do, giving a false sense of safety [83]. Another point to be mentioned is that the presence of residual stresses from the fabrication process reduces the stress which has to be produced by electromigration in order to reach the maximum value a line can withstand. This results in smaller values for the Blech length and for the maximum operating current density than that given by (2.27) and (2.28), respectively [83].

2.4.2 Models of Stress Build-up due to Electromigration

Although Blech had shown that electromigration transport was closely related to mechanical stress development, the first model that connected the rate of stress generation to electromigration was proposed by Kirchheim [53]. He added the gradient of mechanical stress as a driving force in the total vacancy flux equation, so that

$$J_v = -D_v \left(\frac{\partial C_v}{\partial x} - \frac{|Z^*|e\rho j}{kT}C_v + \frac{f\Omega}{kT}C_v\frac{\partial \sigma}{\partial x} \right), \qquad (2.29)$$

where $f = \Omega_v/\Omega$. Thus, the continuity equation can be written as

$$\frac{\partial C_v}{\partial t} = -\frac{\partial}{\partial x}\left[-D_v \left(\frac{\partial C_v}{\partial x} - \frac{|Z^*|e\rho j}{kT}C_v + \frac{f\Omega}{kT}C_v\frac{\partial \sigma}{\partial x} \right) \right] - \frac{C_v - C_{veq}}{\tau}. \qquad (2.30)$$

The last term is a generation/annihilation function similar to that proposed by Rosenberg and Ohring [72], as shown in Section 2.3. However, Kirchheim used the more general expression for the equilibrium vacancy concentration in a grain boundary [84]

$$C_{veq} = C_{v0} \exp\left[\frac{(1-f)\Omega\sigma}{kT} \right], \qquad (2.31)$$

which connects the equilibrium vacancy concentration with mechanical stress.

The volumetric strain in a grain produced by the generation of vacancies is [53]

$$\frac{\Delta V}{V} = (1-f)\Omega\frac{\delta}{d}\Delta C_v, \qquad (2.32)$$

where $(1-f)\Omega$ is the volume change due to lattice relaxation, when a vacancy is treated as a substitutional atom with smaller volume ($0 < f < 1$), δ is the grain boundary thickness, d is the grain diameter, and ΔC_v is the generated vacancy concentration. Thus, the strain rate is given by [53]

$$\frac{1}{V}\frac{\partial V}{\partial t} = (1-f)\Omega\frac{\delta}{d}\frac{C_v - C_{veq}}{\tau}, \qquad (2.33)$$

which together with Hooke's law yields [53]

$$\frac{\partial \sigma}{\partial t} = B(1-f)\Omega\frac{\delta}{d}\frac{C_v - C_{veq}}{\tau}, \qquad (2.34)$$

where B is the appropriate modulus.

This equation shows that the stress build-up is related to the deviation of the vacancy concentration from its equilibrium value and that τ can have a significant impact on the stress development. It is important to note that this model allows different mechanisms of vacancy annihilation or generation to be described, such as annihilation/production in the grain boundary itself, in adjacent grain boundaries or at dislocations within the grain bulk. These lead to smaller, median, and larger values of the characteristic vacancy relaxation time τ, respectively.

Equations (2.30) and (2.34) compose a non-linear system of differential equations, which has to be solved numerically. Nevertheless, Kirchheim derived analytical solutions for some

limiting cases and identified three main phases for vacancy and stress evolution [53]. The first phase corresponds to a short period of time, where the initial stress is very low. Therefore, the equilibrium vacancy concentration remains unaffected and the vacancy concentration develops until a quasi steady-state condition is reached. The quasi steady-state phase is quite long, and the vacancy concentration does not change very much, while the stress grows linearly with time. It lasts until the stress becomes large enough to affect the equilibrium vacancy concentration. Then, a non-linear increase of stress with time is observed and the vacancy concentration approximately follows the development of the equilibrium vacancy concentration, which means that vacancies and stresses are in equilibrium and the true steady-state condition has been reached.

Moreover, Kirchheim [53] showed that, if the electromigration lifetime is determined by the time to reach a certain critical stress, the current density exponent of Black's equation varies from $n = 1$ at low stresses (the time to failure is determined by the quasi steady-state period) to $n = 2$ for higher critical stresses (the time to reach the true steady-state condition determines the lifetime).

A somewhat simplified model for the stress development in a line subject to electromigration was derived by Korhonen *et al.* [54]. They consider that the generation/recombination of vacancies by dislocation climb mechanisms either in grain boundaries or at lattice dislocations changes the concentration of lattice sites, C_L, producing stress according to Hooke's law

$$\frac{dC_L}{C_L} = -\frac{d\sigma}{B}. \tag{2.35}$$

Using the source term [55, 85]

$$G = \frac{\partial C_L}{\partial t}, \tag{2.36}$$

the vacancy continuity equation can be written as

$$\frac{\partial C_v}{\partial t} = -\frac{\partial J_v}{\partial x} - \frac{C_L}{B}\frac{\partial \sigma}{\partial t}. \tag{2.37}$$

Assuming that the vacancy concentration is in equilibrium with the mechanical stress via [84]

$$C_v = C_{veq} = C_{v0}\exp\left(\frac{\Omega\sigma}{kT}\right), \tag{2.38}$$

(2.37) becomes

$$\left(\frac{C_v B\Omega}{C_L kT} + 1\right)\frac{C_L}{B}\frac{\partial \sigma}{\partial t} = \frac{\partial}{\partial x}\left[\frac{D_v C_v}{kT}\left(\Omega\frac{\partial \sigma}{\partial x} - |Z^*|e\rho j\right)\right], \tag{2.39}$$

when J_v given by (2.23) is used.

Korhonen *et al.* observed that $(C_v/C_L)(B\Omega/kT) \ll 1$ at typical electromigration test conditions. This means that most of the transported vacancies initiate climbing dislocation processes which produce mechanical stress, while just a very small number of vacancies is needed to maintain the local equilibrium concentration [54]. Thus, the above approximation leads to

$$\frac{\partial \sigma}{\partial t} = \frac{\partial}{\partial x}\left[\frac{D_a B\Omega}{kT}\left(\frac{\partial \sigma}{\partial x} - \frac{|Z^*|e\rho j}{\Omega}\right)\right], \tag{2.40}$$

where $D_a = D_v C_v / C_L$ [86].

For a line of length L with blocking boundary conditions

$$J_v(0,t) = J_v(-L,t) = 0, \tag{2.41}$$

and assuming a constant D_a, the solution of (2.40) is given by [54, 87]

$$\sigma(x,t) = \frac{|Z^*|e\rho j L}{\Omega} \left[\frac{1}{2} + \frac{x}{L} - 4 \sum_{n=0}^{\infty} m_n^{-2} \exp\left(-m_n^2 \frac{\kappa}{L^2} t\right) \cos\left(m_n \frac{x}{L}\right) \right], \tag{2.42}$$

where

$$\kappa = \frac{D_a B \Omega}{kT}, \tag{2.43}$$

and $m_n = (2n+1)\pi$.

Following the same approach as Korhonen *et al.*, Clement *et al.* [55, 85] derived an equivalent equation in terms of vacancies,

$$\frac{\partial C_v}{\partial t} = \frac{D_a B \Omega}{kT} \left(\frac{\partial^2 C_v}{\partial x^2} - \frac{|Z^*|e\rho j}{kT} \frac{\partial C_v}{\partial x} \right). \tag{2.44}$$

This equation has the same form as (2.13) from the Shatzkes and Lloyd formulation, but with D_v replaced by $D_a B \Omega / kT$. Since it was assumed that vacancies are in equilibrium with stress, the stress can be calculated from (2.38) as

$$\sigma(x,t) = \frac{kT}{\Omega} \ln\left[\frac{C_v(x,t)}{C_{v0}} \right], \tag{2.45}$$

where $C_v(x,t)$ is determined by the solution of (2.44).

Assuming that the electromigration failure is determined by the time to reach a given stress magnitude, the above models predict a mean time to failure of the form

$$MTF = \frac{B(T)}{j^2} \exp\left(\frac{E_a}{kT} \right), \tag{2.46}$$

where an inverse square dependence of the current density is again obtained. The coefficient $B(T)$ is temperature dependent, so that $B(T) \propto T^2$ for Korhonen's formulation [54] and $B(T) \propto T^3$ according to Clement's formulation [85].

Figure 2.1 shows the stress development with time at $x = 0$ according to Korhonen's solution, (2.42). Note that the time scale of stress build-up is in the order of several hours, rather than a few minutes as predicted by the models of Section 2.3. This shows the importance of taking into account the mechanical stress in the model, including the stress dependence in the sink/source term of the continuity equation. The stress distribution along the line for several times is presented in Figure 2.2. At steady-state the stress varies linearly, as predicted by Blech [75, 76, 77]. One can see that high stress can develop in the interconnect line, which is a critical requirement for void nucleation [88, 89].

These models were very successful in explaining the origin of mechanical stress and calculating the hydrostatic stress which develops in a metal line due to electromigration. However,
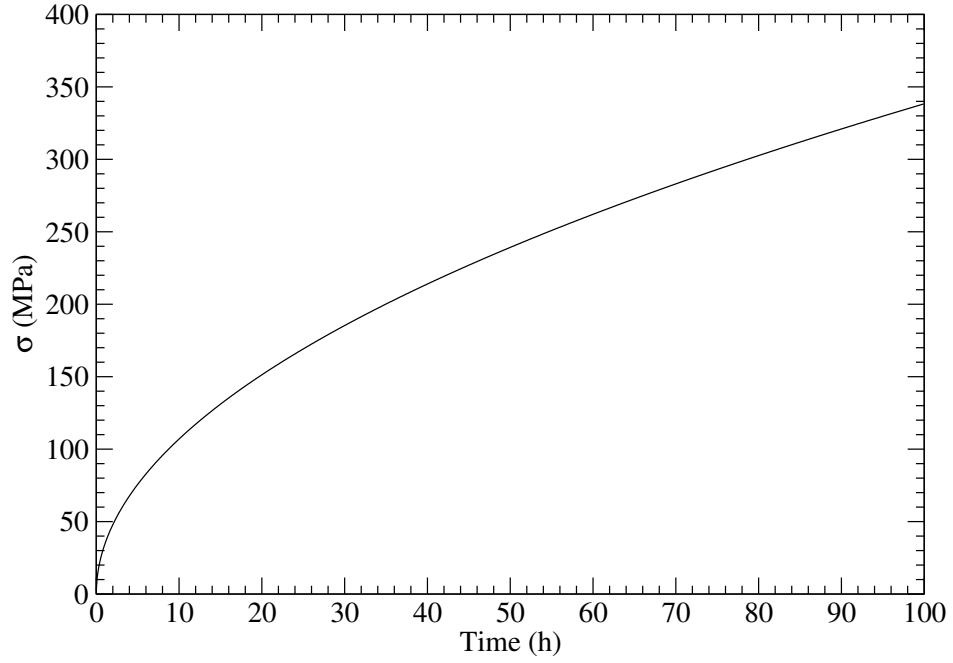
Figure 2.1: Stress build-up at $x = 0$ according to Korhonen's model.
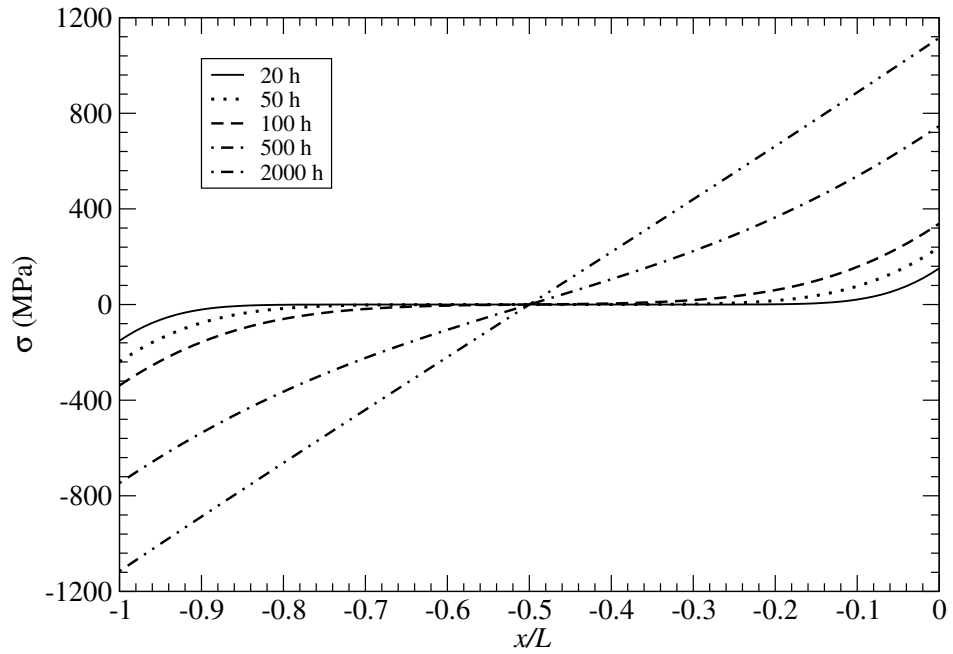
Figure 2.2: Stress build-up along the interconnect at different times.

they are based on several simplifying assumptions and are applicable to simple interconnect lines only. For example, the mechanical properties of the line and the effect of the constraints imposed by the surrounding materials are all taken into account by the modulus B in the equations above. Therefore, a more general description of the problem is required, in order to better understand the mechanical stress distribution and its effects on the interconnect structures.

The connection between material transport with mechanical stress in a general framework was first proposed by Povirk [90] and Rzepka *et al.* [91]. In these works mass accumulation or depletion in the metal line leads to an inelastic strain rate of the form

$$\frac{\partial \varepsilon_{ij}^v}{\partial t} = \Omega \left(\nabla \cdot \vec{J_v} \right) \delta_{ij}, \tag{2.47}$$

where δ_{ij} is Kronecker's symbol.

Sarychev *et al.* [92] extended this formulation considering that the total inelastic strain rate has a contribution from vacancy accumulation/depletion and a contribution from vacancy generation/annihilation, yielding

$$\frac{\partial \varepsilon_{ij}^v}{\partial t} = \frac{1}{3}\Omega \left[f\nabla \cdot \vec{J_v} + (1-f)G \right] \delta_{ij}. \tag{2.48}$$

Assuming that the metal line deforms elastically, that is

$$\sigma_{ij} = \sum_{kl} C_{ijkl}\varepsilon_{kl}, \tag{2.49}$$

where C_{ijkl} is the stiffness tensor, and using the small displacement approximation,

$$\varepsilon_{ij} = \frac{1}{2}\left(\frac{\partial u_i}{\partial x_j} + \frac{\partial u_j}{\partial x_i} \right), \qquad i,j = 1,2,3, \tag{2.50}$$

from the mechanical equilibrium equation,

$$\sum_{j=1}^{3} \frac{\partial \sigma_{ij}}{\partial x_j} = 0, \qquad i = 1,2,3, \tag{2.51}$$

the deformation of the line as a function of the inelastic strain produced by electromigration can be calculated by [92]

$$\mu\nabla^2 u_i + (\lambda + \mu)\frac{\partial}{\partial x_i}\left(\nabla \cdot \vec{u} \right) = B\frac{\partial}{\partial x_i}\text{tr}(\varepsilon_{ij}^v), \quad i = 1,2,3, \tag{2.52}$$

where $\vec{u} = (u_1, u_2, u_3)$ is the displacement vector, λ and μ are the Lamé constants, B is the bulk modulus, and $\text{tr}(\varepsilon_{ij}^v)$ refers to the trace of the electromigration induced strain.

The key characteristic of Sarychev's approach is that it forms a three-dimensional self-consistent model which connects material balance with line deformation. In this way, the impact of the complete interconnect geometry and imposed boundary conditions on the stress evolution can be described. Furthermore, all components of the stress tensor can be determined. Sarychev's model was the basis of several works on simulation of stress evolution due to electromigration [93, 94, 95, 96] in two-dimensional lines.

A different approach was proposed by Sukharev *et al.* [97, 98, 99, 100], who introduced the concept of plated atoms to describe the atom exchange between bulk and interfaces. He suggested that the event of vacancy generation or annihilation is simultaneously accompanied by atom plating or removal from the grain boundary region, respectively. Therefore, the rate of atom plating/removal is given by the same source function as for vacancies,

$$G_{int} = -\frac{C_v^{int} - C_{veq}}{\tau}. \tag{2.53}$$

However, considering the plated atoms to be immobile (the atomic mobility is far smaller than the vacancy mobility), the plated atom continuity equations for bulk and interfaces, respectively, are given by [97]

$$\begin{aligned} \frac{\partial C_{pl}^{bulk}}{\partial t} &= 0, \\ \frac{\partial C_{pl}^{int}}{\partial t} + G_{int} &= 0, \end{aligned} \tag{2.54}$$

where C_{pl} is the plated atom concentration.

Using this concept, the electromigration induced strain is written as [97]

$$\varepsilon_{ij}^v = \Omega\left[-(1-f)(C_v - C_{v0}) + (C_{pl} - C_{pl0})\right]\delta_{ij}, \tag{2.55}$$

where C_{pl0} is the plated atom concentration at zero stress. This equation shows a close connection between the local strain with the vacancy concentration and the plated atom concentration. However, Sukharev *et al.* observed that the increment of the plated atom concentration is the major responsible cause for stress build-up [97].

2.5 Void Nucleation

Initially, void nucleation was attributed to the accumulation of vacancies at sites of flux divergence caused by their drift due to electromigration. As the vacancy concentration at a particular site reached a certain critical magnitude, vacancy condensation would lead to the formation of a void [50, 51, 52, 98, 101, 102, 103, 104]. However, an unrealistically high vacancy supersaturation would be necessary for spontaneous void formation by vacancy condensation [72, 105]. Therefore, according to classical thermodynamics homogeneous void nucleation by a vacancy condensation mechanism cannot be supported under electromigration.

Meanwhile, several works investigated the impact of mechanical stress on void nucleation at various conditions [106, 107, 108, 109]. The importance of mechanical stress build-up in an interconnect line under electromigration was recognized, so that the development of a critical stress became the major criterion for void formation [53, 54, 85, 95, 110]. Nevertheless, the stress threshold value is still an open issue, varying from work to work.

Gleixner *et al.* [89] carried out a thorough analysis of the nucleation rates at various locations within an interconnect line. For a copper dual-damascene interconnect, the free energy change upon creation of an embryo of volume V_e is given, in general, by

$$\Delta F = -\sigma V_e + \gamma_s A_{Cu} + (\gamma_{cap} - \gamma_i)A_i - \gamma_{gb}A_{gb}, \tag{2.56}$$

where ΔF is the Helmholtz free energy per unit volume of the embryo, σ is the stress, γ_s, γ_{cap}, γ_{cap}, and γ_{gb} are the surface free energies of the metal, capping layer, Cu/capping layer interface, and grain boundary, respectively, and the $A's$ are the areas of the surfaces created or destroyed upon formation of the embryo. The energy barrier for void nucleation, ΔF^*, is then given by the condition

$$\Delta F^* = \Delta F|_{\partial(\Delta F)} = 0, \tag{2.57}$$

which determines a critical embryo volume. For homogeneous nucleation the barrier is given by [89]

$$\Delta F^* = \frac{16\pi\gamma_s^3}{3\sigma^2}. \tag{2.58}$$

According to Backer-Döring nucleation theory a nucleation event takes place when a vacancy sticks to a critical embryo. In this way, the nucleation can be expressed as [111]

$$I = Rn_sZ, \tag{2.59}$$

where R is the sticking rate of vacancies, n_s is the number of vacancies in the matrix at the surface of a critical embryo, and Z represents the number of critical embryos. The number of critical embryos per unit volume is a function of the energy barrier, [111]

$$Z = \frac{1}{\Omega\,n}\left(\frac{\Delta F^*}{3\pi kT}\right)^{1/2} \exp\left(-\frac{\Delta F^*}{kT}\right), \tag{2.60}$$

where n is the number of vacancies in a critical embryo. The sticking rate of vacancies can be related to the exchange frequency of the diffusive process [89],

$$R = \nu \exp\left(-\frac{U_d}{kT}\right), \tag{2.61}$$

where ν is the frequency of vibration of the atoms, and U_d is the activation energy of the jump process. Combining (2.59), (2.60), and (2.61) yields

$$I = \nu \exp\left(-\frac{U_d}{kT}\right) \frac{1}{\Omega\,n}\left(\frac{\Delta F^*}{3\pi kT}\right)^{1/2} \exp\left(-\frac{\Delta F^*}{kT}\right) n_s. \tag{2.62}$$

Figure 2.3 shows the rate of homogeneous nucleation as function of the temperature for different levels of stress. One can see that the nucleation rate is very small, and even a very high temperature and a high stress cannot significantly increase the nucleation rate. Gleixner *et al.* obtained small rates for nucleation at grain boundaries, at the metal/capping layer interface, and even at the metal/capping layer interface intersected by a grain boundary [89]. Therefore, none of these mechanisms can lead to void formation.

The small rate for nucleation at the metal/capping layer interface intersected by a grain boundary is particularly interesting, since voids are frequently observed to nucleate at such locations [10]. This apparent discrepancy was solved by Flinn [88], who suggested that a void could form at a pre-existing free surface. Free surfaces can result from contamination
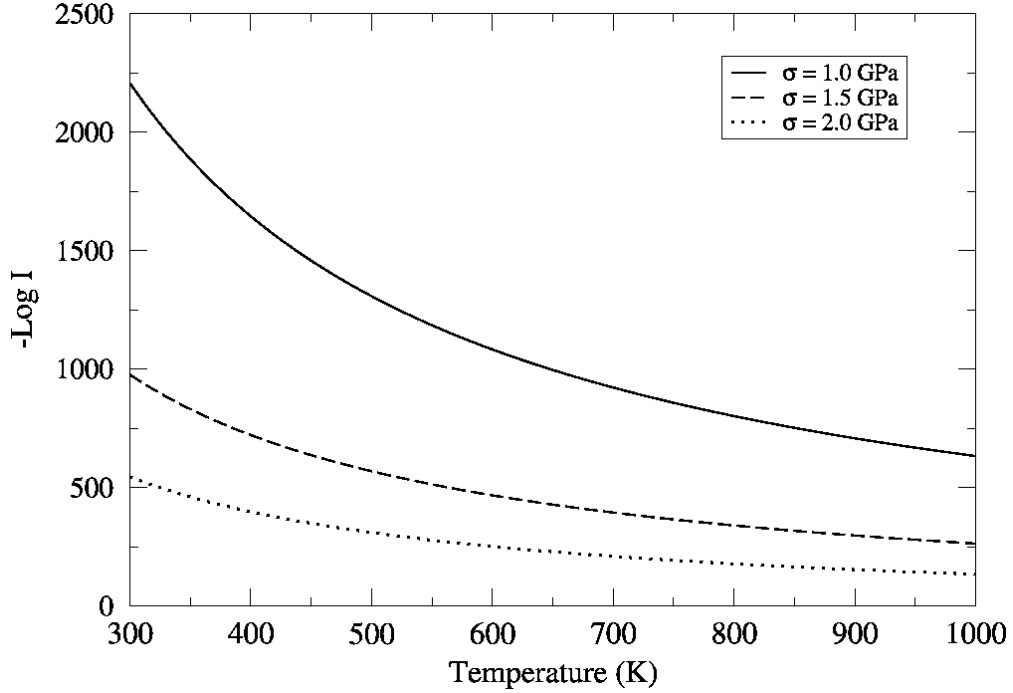
Figure 2.3: Homogeneous nucleation rate dependence on temperature and hydrostatic stress. The nucleation rate is small, even at high temperatures and stresses.

during the line fabrication process, which hinders the bounding of the surrounding layer to the metal surface. In this way, assuming a circular flaw of radius R_p the critical stress for void nucleation is given by [88]

$$\sigma_{th} = \frac{2\gamma_s}{R_p}. \tag{2.63}$$

Clemens *et al.* [112] showed that the above equation is valid as long as the void grows in the contaminated region. However, it is possible that the void extends beyond the flaw area, as shown by Figure 2.4, once the equilibrium contact angle, θ_c, is reached. The equilibrium contact angle is determined by interfacial energy balance, and lies in the range $0 < \theta_c < 90°$. In this case, the threshold stress is given by [89, 112]

$$\sigma_{th} = \frac{2\gamma_s \sin\theta_c}{R_p}, \tag{2.64}$$

which may represent a small decrease in the nucleation energy barrier compared to (2.63).

The critical stress is significantly reduced as the flaw area increases. For instance, for a flaw radius as small as 10 nm the critical stress is $\sigma_{th} \approx 340$ MPa [110], which can be certainly reached by thermal stresses alone. Considering that the contaminated region can extend trough the whole line width, for a 100 nm wide line the critical stress becomes $\sigma_{th} \approx 70$ MPa. Experimental works have reported values of critical stress for void nucleation of about the same order of magnitude [82, 113]. Such a stress value is quite low and can be easily obtained in an interconnect line under electromigration.
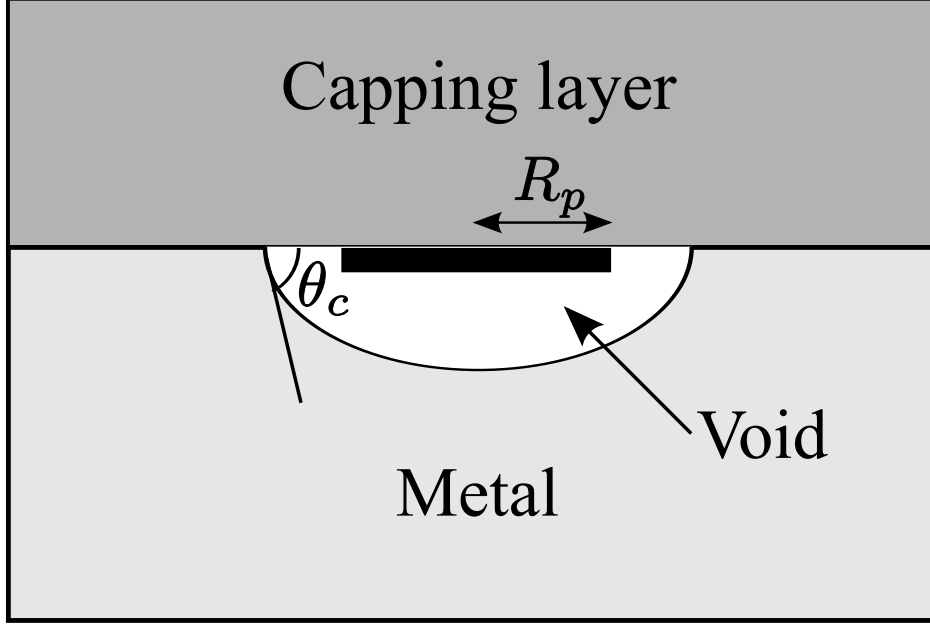
Figure 2.4: Schematic void nucleation at an interface site of weak adhesion.

2.6 On the Void Evolution

The development of fatal voids, i.e. voids that trigger the line failure, is the ultimate cause for the electromigration induced interconnect failure [22, 81]. The failure criterion is typically set as a maximum resistance increase tolerated for the corresponding interconnect line. Once a void is nucleated it can evolve, until it causes a significant resistance increase or even completely severs the line.

The void evolution phase can encompass several processes: a void can migrate along the interconnect [10, 114], interact with the local microstructure [10, 38, 71] and grow, or even heal [10, 11], undergo morphologic changes, assuming wedge-like shape or slit-like shape [27], before it definitely triggers interconnect failure. Furthermore, multiple voids can form in a line, so that their migration and agglomeration at a specific critical site can be the mechanism responsible for the interconnect failure [31, 32, 114].

The void surface acts as an additional path for atomic migration. The chemical potential of an atom on the void surface is given by [115, 116, 117]

$$\mu_s = \mu_0 + \Omega \left(w - \gamma_s \kappa \right), \tag{2.65}$$

where μ_0 is a reference chemical potential, $w = \left(\boldsymbol{\sigma} : \boldsymbol{\varepsilon} \right) / 2$ is the elastic energy density of the material adjacent to the void, γ_s is the surface free energy, and κ is the curvature of the void surface. Thus, the atomic flux along the void surface due to gradients in chemical potential plus electromigration has the form

$$\vec{J}_s = -\frac{D_s \delta_s}{kT} \left(\nabla_s \mu_s + e|Z^*|\vec{E}_s \right), \tag{2.66}$$

31

where D_s is the surface diffusivity, δ_s is the surface thickness, $\vec{E}_s$ is the electric field tangential to the void surface, and ∇_s denotes the gradient along the surface. By mass conservation the normal velocity at any point on the surface is given by [116, 117]

$$v_n = -\nabla_s \cdot \vec{J}_s. \tag{2.67}$$

Void evolution due to electromigration is a complex dynamic process, for which modeling is a challenging task and, moreover, represents a moving boundary problem. Analytical solutions can only describe the asymptotic behavior of the moving boundary [105, 118, 119, 120, 121, 122, 123], since, in general, the shape changes which the void experiences cannot be analytically resolved. Therefore, a more general treatment demands the application of numerical methods and special techniques for tracking the void.

The most commonly used numerical method is based on sharp interface models [124, 125, 126, 127, 128], which requires an explicit tracking of the void surface and, consequently, a continuous remeshing procedure. As the void migrates, grows, and changes shape this explicit tracking becomes very demanding. Therefore, it can be satisfactorily applied only for simple two-dimensional cases and cannot be further extended. This shortcoming can be overcome with the introduction of the so-called diffuse interface model (or phase field model) [116, 117, 129, 130, 131, 132, 133] or the level set method [134, 135, 136, 137, 138]. The main advantage of these approaches is that the void is implicitly represented by a field parameter or level set function, so that void evolution is implicitly determined by the calculation of these functions. Thus, the demanding explicit void surface tracking can be avoided.

Chapter 3

A General TCAD Electromigration Model

In the previous chapter the various physical phenomena related to electromigration were described and several physically based models were presented. Most of these models, however, are either based on several simplifying assumptions in order to obtain analytical expressions or can only be applied for simulation of simple interconnect geometries. Thus, they cannot cope with the complex modern interconnect structures, as that shown in Figure 3.1. Thus, in this chapter a general electromigration model for implementation in a TCAD tool for simulation of realistic three-dimensional interconnect structures is developed.
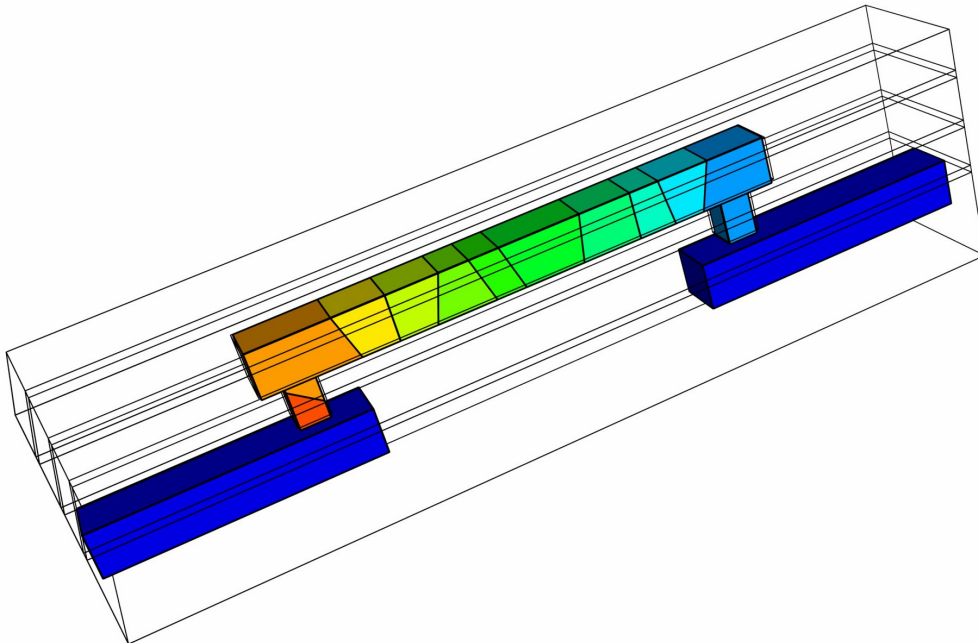
Figure 3.1: Dual-damascene interconnect structure.

Since the electromigration simulation requires a multiphysics approach, the model equations can be most conveniently separated in smaller blocks. Starting with the description of the electro-thermal problem, the distributions of electric potential, electric field, current density, and temperature in the interconnect can be determined. Then, the material transport equations are presented. Here, an approach for taking into account the effect of grain boundaries and material interfaces as fast diffusivity paths is described. Moreover, the influence of the mechanical stress on the diffusivity is discussed and the equation for the strain evolution as a result of material transport is derived. The dynamic behavior of grain boundary and material interfaces acting as sites for vacancy generation and annihilation is treated in detail. Then, the mechanical equations which describe the line deformation and the corresponding stress build-up are explained. Finally, a brief model overview is given, where the blocks of equations are presented, which have to be numerically solved for electromigration simulations.

3.1 Electro-Thermal Problem

Denoting the electric potential at any point in the line by φ and the electrical conductivity by γ_E, the current density can be calculated from Ohm's law as

$$\vec{j} = \gamma_E \vec{E} = -\gamma_E \nabla \varphi, \tag{3.1}$$

where the electric field is related to the electric potential by

$$\vec{E} = -\nabla \varphi. \tag{3.2}$$

Since the electric charge should obviously be conserved, one can write

$$\nabla \cdot \vec{j} = 0, \tag{3.3}$$

which together with (3.1) yields an equation written for the electric potential,

$$\nabla \cdot (\gamma_E \nabla \varphi) = 0. \tag{3.4}$$

Note that (3.4) reduces to the Laplace equation,

$$\nabla^2 \varphi = 0, \tag{3.5}$$

if the electrical conductivity is constant along the line.

The temperature distribution is determined by the solution of the thermal problem

$$\nabla \cdot (\gamma_T \nabla T) = \rho_m c_p \frac{\partial T}{\partial t} - p, \tag{3.6}$$

where γ_T is the material thermal conductivity, ρ_m is the mass density, and c_p is the specific heat. Here, p is the electrical power loss density, given by

$$p = \gamma_E E^2 = \gamma_E \left(\nabla \varphi \right)^2, \tag{3.7}$$

which accounts for the Joule heating and couples the electrical with the thermal problem.

Both, the electrical and thermal conductivity are treated as temperature dependent parameters, following the form

$$\gamma(T) = \frac{\gamma_0}{1 + \alpha(T - T_0) + \beta(T - T_0)^2},$$ (3.8)

where γ_0 is the conductivity for a given reference temperature T_0. Here, α and β are the linear and quadratic temperature coefficients, respectively.

The equations (3.4) and (3.6), together with (3.7) and (3.8), compose a non-linear system of equations, whose solution provides the voltage, electric field, current density, and temperature distributions in an interconnect line. It should be pointed out that special attention must be taken in setting the thermal boundary conditions. In order to properly consider the effect of Joule heating, a sufficient big portion of dielectric surrounding must be included in the simulation. A thermal reservoir can be implemented by a Dirichlet boundary condition for the temperature.

3.2 Material Transport Equations

For a proper analysis of the total material transport which occurs in an interconnect line during electromigration, the various driving forces for atomic migration have to be considered. As in copper metallizations atomic migration occurs via vacancy diffusion mechanisms, the total material transport can be equivalently written in terms of vacancies. Thus, the combination of the driving forces leads to the total vacancy flux of the form [53, 92]

$$\vec{J}_v = -D_v \left(\nabla C_v + \frac{|Z^*|e}{kT} C_v \nabla \varphi - \frac{Q^*}{kT^2} C_v \nabla T + \frac{f\Omega}{kT} C_v \nabla \sigma \right).$$ (3.9)

In this equation the first term describes a diffusional effect, the second term represents electromigration, the third term represents the material transport which occurs due to thermal gradients in the interconnect, and the last term accounts for the atomic migration caused by gradients of mechanical stress.

Two mechanisms contribute to a local change in vacancy concentration. In the first one vacancies accumulate or vanish due to the existence of flux divergences. In the second, the vacancy concentration is altered by the production or recombination of vacancies in the presence of source/sink mechanisms. Thus, material balance is described by the continuity equation

$$\frac{\partial C_v}{\partial t} = -\nabla \cdot \vec{J}_v + G,$$ (3.10)

where G is a function which models vacancy generation and annihilation processes. Vacancy generation or annihilation is related to the change of lattice sites. Therefore, this term is active only at the appropriate interfaces, like grain boundaries and material interfaces [139].

3.2.1 Fast Diffusivity Paths

In Chapter 2 the role of diffusivity paths for material transport was discussed. It is clear that diffusion occurs along the various available paths and must be taken into account. Using the

simple effective diffusion model is rather inconvenient for TCAD analysis, since one is not able to completely separate and understand the effect of each path on the distribution of material in the interconnect line. Consequently, a realistic picture of the mechanical stress distribution is not possible either. Moreover, each path has also a different effective valence [21, 140], since the wind force depends on the electronic configuration surrounding an atom [58].

Thus, for generality of the model, the diffusion coefficient, D_v, and the effective valence, Z^*, in (3.9) must be independently set for each region of the interconnet. In this way, combining (3.9) and (3.10) one obtains

$$\frac{\partial C_v^{bulk}}{\partial t} = \nabla \cdot \left[D_v^{bulk} \left(\nabla C_v^{bulk} + \frac{|Z_{bulk}^*|e}{kT} C_v^{bulk} \nabla \varphi - \frac{Q^*}{kT^2} C_v^{bulk} \nabla T + \frac{f\Omega}{kT} C_v^{bulk} \nabla \sigma \right) \right], \quad (3.11)$$

for the bulk and

$$\frac{\partial C_v^{int}}{\partial t} = \nabla \cdot \left[D_v^{int} \left(\nabla C_v^{int} + \frac{|Z_{int}^*|e}{kT} C_v^{int} \nabla \varphi - \frac{Q^*}{kT^2} C_v^{int} \nabla T + \frac{f\Omega}{kT} C_v^{int} \nabla \sigma \right) \right] + G_{int}, \quad (3.12)$$

for interfaces which for copper dual-damascene interconnects can be either grain boundaries, the copper/capping layer interface or the copper/barrier layer interface.

3.2.2   Anisotropic Diffusivity: Diffusion Dependence on Stress

Residual mechanical stresses are introduced on interconnect lines as a result of the fabrication process flow [141]. These stresses can be very high, significantly affecting the diffusion coefficient of the interconnect metal atoms [142].

Typically, the diffusion dependence on stress is taken into account through a simple modification of the usual diffusion coefficient expression (2.10) to [54, 97]

$$D(\sigma) = D_0 \exp \left(\frac{-E_a + \Omega\sigma}{kT} \right). \quad (3.13)$$

In this way, (3.13) describes the effect of a scalar hydrostatic stress on the scalar diffusion coefficient. However, Flynn [143] pointed out that, for a homogeneously deformed cubic crystal with strain field ε_{kl}, there is an additional contribution proportional to ε_{kl} to the diffusion of the form

$$D_{ij} = D(0)\delta_{ij} + \sum_{kl} d_{ijkl}\varepsilon_{kl}, \quad (3.14)$$

where d_{ijkl} is the elastodiffusion tensor, which can be experimentally determined. Here, the simple scalar diffusivity is replaced by a tensorial quantity. Consequently, in the presence of a stress field the diffusivity can now become anisotropic, depending on the properties of d_{ijkl}.

Based on microscopic lattice theory, Dederichs and Schroeder [142] showed that the diffusivity in a simple face-centered cubic crystal (fcc) follows

$$D_{ij} = \frac{1}{2} \sum_h R_i^h R_j^h \Gamma^h, \quad (3.15)$$

where $\vec{R}^h$ is the jump vector for a hop h and Γ^h is the corresponding jump rate. From classical thermodynamics the jump rate is given by [59, 144]

$$\Gamma^h = \nu \exp\left[-\frac{E_m^h(\boldsymbol{\varepsilon})}{kT}\right], \tag{3.16}$$

where ν is the Debye frequency ($\sim 10^{13}$ s^{-1} for metals [144]) and E_m^h is the migration energy barrier. The presence of an external strain field affects the jump rate by changing the migration energy barrier according to [145]

$$E_m^h(\boldsymbol{\varepsilon}) = E_m(0) + \Omega \boldsymbol{\varepsilon}_I^h \cdot (\mathbf{C}\boldsymbol{\varepsilon}), \tag{3.17}$$

where $E_m(0)$ is the migration energy barrier in the absence of an external field, $\boldsymbol{\varepsilon}_I^h$ is the induced strain, $\mathbf{C}$ is the elasticity tensor, and $\boldsymbol{\varepsilon}$ is the applied external strain. For a fcc crystal the elasticity tensor has the form [146]

$$\mathbf{C} = \begin{bmatrix} C_{11} & C_{12} & C_{12} & 0 & 0 & 0 \\ C_{12} & C_{11} & C_{12} & 0 & 0 & 0 \\ C_{12} & C_{12} & C_{11} & 0 & 0 & 0 \\ 0 & 0 & 0 & C_{44} & 0 & 0 \\ 0 & 0 & 0 & 0 & C_{44} & 0 \\ 0 & 0 & 0 & 0 & 0 & C_{44} \end{bmatrix}. \tag{3.18}$$

Combining (3.16) and (3.17) one obtains

$$\Gamma^h = \Gamma_0 \exp\left[-\frac{\Omega \boldsymbol{\varepsilon}_I^h \cdot (\mathbf{C}\boldsymbol{\varepsilon})}{kT}\right], \tag{3.19}$$

with

$$\Gamma_0 = \nu \exp\left[-\frac{E_m(0)}{kT}\right]. \tag{3.20}$$

Considering a single vacant point defect in a crystal lattice, the local volumetric strain induced by the presence of this vacancy is given by

$$\frac{\Omega_v - \Omega}{\Omega} = f - 1 = \varepsilon_{11}^I + \varepsilon_{22}^I + \varepsilon_{33}^I, \tag{3.21}$$

where Ω_v is the vacancy volume and ε_{11}^I, ε_{22}^I, and ε_{33}^I are the induced strains in the given directions. Due to the symmetry of a vacant point defect

$$\varepsilon_{11}^I + \varepsilon_{22}^I + \varepsilon_{33}^I = 3\varepsilon_I, \tag{3.22}$$

which together with (3.21) yields

$$\varepsilon_I = -\frac{1-f}{3}. \tag{3.23}$$

Thus, the induced strain tensor becomes

$$\boldsymbol{\varepsilon}_I = \begin{bmatrix} \varepsilon_I & & \\ & \varepsilon_I & \\ & & \varepsilon_I \end{bmatrix} \tag{3.24}$$

and the induced strain vector is determined by

$$\varepsilon_I^h = |\boldsymbol{\varepsilon}_I \cdot \vec{r}_h|, \tag{3.25}$$

where $\vec{r}_h$ is a jump unit vector for a hop h.

Normalizing (3.15) with the jump distance λ and summing over the z nearest neighbors ($z = 12$ for fcc crystals) one obtains

$$D_{ij} = \frac{1}{2}\lambda^2 \sum_{h=1}^{z} \frac{R_i^h}{\lambda}\frac{R_j^h}{\lambda}\Gamma^h = \frac{1}{2}\lambda^2 \sum_{h=1}^{z} r_i^h r_j^h \Gamma^h. \tag{3.26}$$

Substituting (3.19) in this equation, the diffusivity tensor in the presence of a external stress field is determined through the expression

$$D_{ij} = \frac{3}{Z}D_0 \sum_{h=1}^{z} r_i^h r_j^h \exp\left[-\frac{\Omega\varepsilon_I^h \cdot (\mathbf{C}\boldsymbol{\varepsilon})}{kT}\right], \tag{3.27}$$

where D_0 is given by [144]

$$D_0 = \frac{1}{6}\lambda^2 z \Gamma_0. \tag{3.28}$$

In order to take into account the anisotropy of diffusion, the scalar diffusivity, D_v, in the flux equation (3.9) is replaced by the stress dependent diffusivity tensor $\mathbf{D}$ yielding

$$\vec{J}_v = -\mathbf{D}\left(\nabla C_v + \frac{|Z^*|e}{kT}C_v\nabla\varphi - \frac{Q^*}{kT^2}C_v\nabla T + \frac{f\Omega}{kT}C_v\nabla\sigma\right), \tag{3.29}$$

with $\mathbf{D}$ calculated via (3.27). In this way, the development of mechanical stress can lead to anisotropic diffusion in the interconnect line, therefore, affecting the material transport along the line under electromigration.

3.3 Electromigration Induced Stress

Given an ideal crystal lattice as shown in Figure 3.2(a), the effect of introducing a vacancy which replaces an atom is schematically presented in Figure 3.2(b). It shows that, if the volume of a vacancy is different from the atom one, a change in vacancy concentration induces strain in the lattice due to its relaxation. Since in a typical interconnect structure the metal line is fully embedded in a passivation layer, this strain field cannot be accommodated, thus, leading to the development of mechanical stress.

As previously described in Section 3.2, the change in vacancy concentration at any point of an interconnect occurs either by a vacancy-atom exchange mechanism or, at interfaces, also by the production or annihilation of vacancies by a source/sink mechanism. This means that the strain induced by electromigration has two contributions: a migration component associated with the vacancy-atom exchange process, and a component related to vacancy production/annihilation.
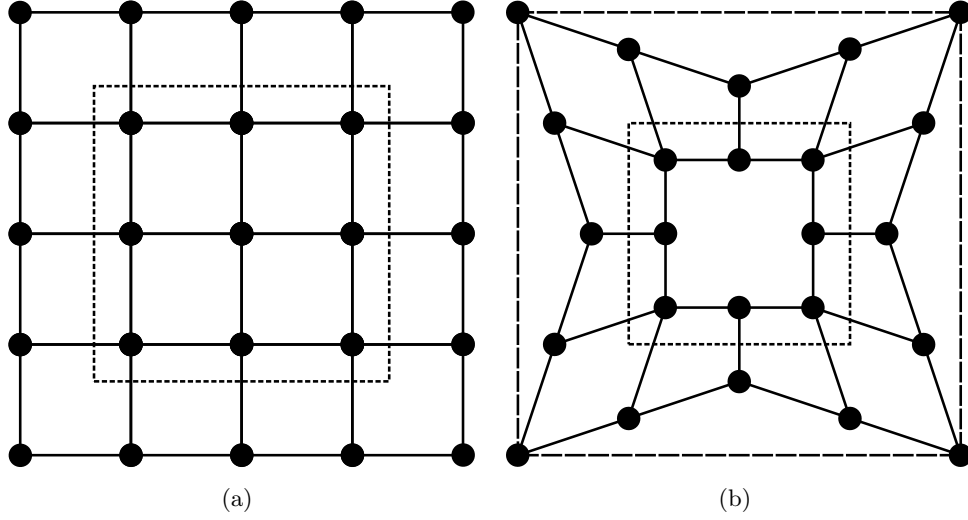
Figure 3.2: Effect of a vacancy in an ideal crystal lattice. (a) Initial lattice. (b) Deformed lattice.

3.3.1 Strain due to Vacancy Migration

When an atom is exchanged for a vacancy, the neighboring atoms relax, leading to a total volume change given by

$$\Delta V = \Omega_v - \Omega = -(1-f)\Omega. \tag{3.30}$$

Given a test volume V, the relative volume change associated with a change in vacancy concentration ΔC_v is [147]

$$\frac{\Delta V}{V} = -(1-f)\Omega\Delta C_v, \tag{3.31}$$

so that the volumetric strain has the form

$$\frac{\Delta V}{V} = \varepsilon_{11}^m + \varepsilon_{22}^m + \varepsilon_{33}^m = 3\varepsilon^m = -(1-f)\Omega\Delta C_v, \tag{3.32}$$

where ε^m refers to the migration strain.

Taking the time derivative of the above equation one gets

$$\frac{\partial \varepsilon^m}{\partial t} = -\frac{1}{3}(1-f)\Omega\frac{\partial C_v}{\partial t}, \tag{3.33}$$

and, since for the test volume the atom-vacancy exchange is governed by the continuity equation

$$\frac{\partial C_v}{\partial t} = -\nabla \cdot \vec{J}_v, \tag{3.34}$$

the components of the migration strain rate is given by

$$\frac{\partial \varepsilon_{ij}^m}{\partial t} = \left[\frac{1}{3}(1-f)\Omega\nabla \cdot \vec{J}_v\right]\delta_{ij}. \tag{3.35}$$

39

3.3.2 Strain due to Vacancy Generation/Annihilation

The generation or annihilation of vacancies is accompanied by a change in the concentration of lattice sites, so that $\Delta C_v = \Delta C_L$ [139]. Thus, the relative volume change of a given test volume due to the addition or removal of lattice sites through a change in the local vacancy concentration ΔC_v by means of generation/annihilation processes is [147]

$$\frac{\Delta V}{V} = f\Omega\Delta C_v, \tag{3.36}$$

where $f\Omega$ accounts for the vacancy volume. Following the same procedure as described above, the strain rate is given by

$$\frac{\partial \varepsilon^g}{\partial t} = \frac{1}{3}f\Omega\frac{\partial C_v}{\partial t}, \tag{3.37}$$

where ε^g refers to the strain produced due to vacancy generation/annihilation processes.

Since the change in vacancy concentration is given by generation or annihilation processes

$$\frac{\partial C_v}{\partial t} = G, \tag{3.38}$$

which leads to the generation/annihilation strain rate components

$$\frac{\partial \varepsilon^g_{ij}}{\partial t} = \left[\frac{1}{3}f\Omega G\right]\delta_{ij}. \tag{3.39}$$

3.3.3 Total Electromigration Strain

The total strain induced by electromigration is given by the sum of the vacancy migration and vacancy generation/annihilation components,

$$\varepsilon^v_{ij} = \varepsilon^m_{ij} + \varepsilon^g_{ij}. \tag{3.40}$$

Taking the time derivative of (3.40), and using (3.35) and (3.39), the total strain rate produced by electromigration is given by

$$\frac{\partial \varepsilon^v_{ij}}{\partial t} = \frac{1}{3}\Omega\left[(1-f)\nabla \cdot \vec{J_v} + fG\right]\delta_{ij}. \tag{3.41}$$

Since ε^v_{ij} is a diagonal tensor with equal entries, one can write (3.41) in terms of the trace of the strain tensor

$$\frac{\partial \varepsilon^v}{\partial t} = \Omega\left[(1-f)\nabla \cdot \vec{J_v} + fG\right]. \tag{3.42}$$

Given the dependence of the electromigration induced strain on the source function G, the modeling approach for mechanisms of generation and annihilation of vacancies becomes of crucial importance.

3.4 Vacancy Sinks and Sources

Grain boundaries, dislocations and interfaces can act as sinks and sources for vacancies in metals [148]. Given the importance of the vacancy generation and annihilation processes for material transport and mechanical stress build-up in the interconnect lines, a detailed model for treating grain boundaries and material interfaces as sites of vacancy generation or annihilation is presented.

3.4.1 Grain Boundary Model

The grain boundary is modeled as a separate medium of width δ embedded in a bulk, as depicted in Figure 3.3. Following the work of Fisher [149], the model takes into account two main mechanisms: vacancy diffusion along the grain boundary, which is considered a path of high diffusivity, and material exchange between the grain boundary and the grain bulk. Therefore, the vacancy dynamics inside the grain boundary can be described by

$$\frac{\partial C_v^{gb}}{\partial t} = -\frac{\partial J_v^{gb}}{\partial l} - \frac{1}{\delta}\left(J_{v,2} - J_{v,1}\right), \tag{3.43}$$

where C_v^{gb} is the grain boundary vacancy concentration, J_v^{gb} is the vacancy flux along the grain boundary distance l, and $J_{v,1}, J_{v,2}$ are the fluxes from both sides of the grain boundary.

The last term in (3.43) connects the change in grain boundary vacancy concentration to the diffusing flux from/to the bulk. The difference $J_{v,2} - J_{v,1}$ corresponds to an actual loss/gain of vacancies, which is localized at the region representing the grain boundary. Thus,
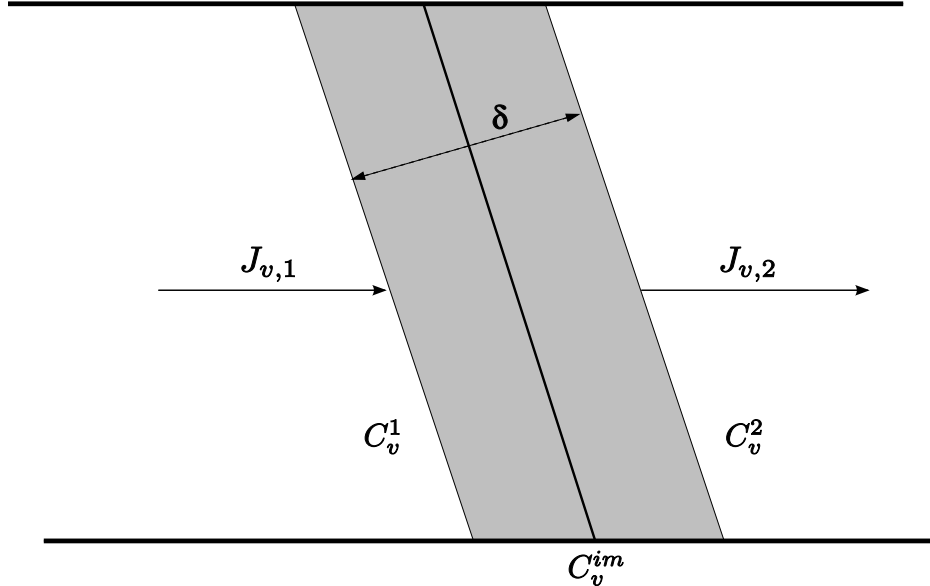
Figure 3.3: Grain boundary model.

the vacancy generation/annihilation rate is given by

$$G = -\frac{J_{v,2} - J_{v,1}}{\delta}. \tag{3.44}$$

This loss/gain of vacancies can be described by a trapped vacancy concentration in the grain boundary, defined as C_{im}, in such a way that the generation/annihilation rate can be expressed as a function of the rate change of the trapped vacancy concentration as

$$G = \frac{\partial C_{im}}{\partial t}. \tag{3.45}$$

By treating the grain boundary as a region with the capability of absorbing or releasing vacancies, the fluxes in equation (3.44) can be expressed in terms of trapping and releasing events in a similar way to [150]. This yields [110]

$$J_{v,1} = \omega_T(C_{veq} - C_{im})C_v^1 - \omega_R C_{im}, \tag{3.46}$$

$$J_{v,2} = -\omega_T(C_{veq} - C_{im})C_v^2 + \omega_R C_{im}, \tag{3.47}$$

where ω_T is the trapping rate of vacancies, ω_R is the release rate, C_v^1, C_v^2 are the vacancy concentration in each grain section, and C_{veq} is the equilibrium vacancy concentration inside the grain boundary, given by

$$C_{veq} = C_{v0} \exp\left(\frac{\sigma_{nn}\Omega}{kT}\right). \tag{3.48}$$

C_{v0} is the equilibrium vacancy concentration in the absence of stress and σ_{nn} is the stress component normal to the grain boundary.

Substituting (3.46) and (3.47) in (3.44) and (3.45) one obtains

$$G = \frac{\partial C_{im}}{\partial t} = \frac{\omega_T(C_v^1 + C_v^2)}{\delta} \left\{ C_{veq} - C_{im} \left[1 + \frac{2\omega_R}{\omega_T(C_v^1 + C_v^2)} \right] \right\}. \tag{3.49}$$

For convenience, (3.49) is rewritten

$$\frac{\partial C_{im}}{\partial t} = \frac{1}{\tau_{gb}} \left\{ C_{veq} - C_{im} \left[1 + \frac{2\omega_R}{\omega_T(C_v^1 + C_v^2)} \right] \right\}, \tag{3.50}$$

with

$$\frac{1}{\tau_{gb}} = \frac{\omega_T(C_v^1 + C_v^2)}{\delta}. \tag{3.51}$$

τ_{gb} represents the characteristic time of a vacancy annihilation or generation process and it characterizes the efficiency of the grain boundary acting as a vacancy sink/source. The smaller the value of τ_{gb}, the more efficient is the source/sink mechanism and, according to (3.10), the faster the steady state condition for the vacancy concentration is reached.

As in the numerical implementation the grain boundary is represented by the interface between two grains ($\delta \to 0$), the approximation $C_v^1 \sim C_v^2 = C_v$ can be used, so that (3.50) and (3.51) is further simplified to

$$\frac{\partial C_{im}}{\partial t} = \frac{1}{\tau_{gb}} \left[C_{veq} - C_{im} \left(1 + \frac{\omega_R}{\omega_T C_v} \right) \right], \tag{3.52}$$

and

$$\frac{1}{\tau_{gb}} = \frac{2\omega_T C_v}{\delta}. \tag{3.53}$$

Note that under the condition

$$\frac{\omega_R}{\omega_T C_v} \ll 1, \tag{3.54}$$

equation (3.52) reduces to the Rosenberg-Ohring generation/annihilation function given in (2.21).

3.4.2 Material Interfaces

Using the same concept to that described above for the grain boundary model, one can derive a similar expression for the source function for the material interfaces of a dual-damascene interconnect. A schematic representation of a material interface is shown in Figure 3.4.

Since the copper/capping layer and the copper/barrier layer interface act as blocking boundaries for copper diffusion, the flux $J_{v,2}$ vanishes, so that (3.44) becomes

$$G = \frac{J_{v,1}}{\delta}. \tag{3.55}$$

Applying (3.46) in the above equation yields an expression similar to (3.52),

$$G = \frac{\partial C_{im}}{\partial t} = \frac{1}{\tau_i} \left[C_{veq} - C_{im} \left(1 + \frac{\omega_R}{\omega_T C_v} \right) \right], \tag{3.56}$$
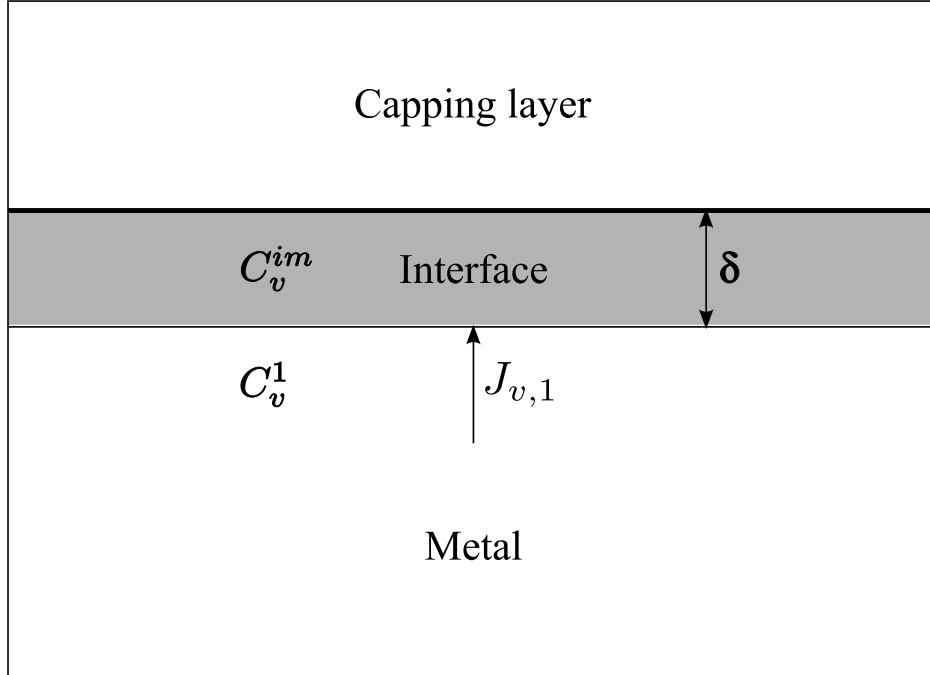
Figure 3.4: Interface model.

but the characteristic generation/annihilation time is now given by

$$\frac{1}{\tau_i} = \frac{\omega_T C_v}{\delta}. \tag{3.57}$$

The grain boundary and material interface model presented here is quite general and can be used for every interface of an interconnect structure.

3.5 Mechanical Deformation

It has been shown that material transport due to electromigration produces local strain, which leads to the deformation of the interconnect line. This deformation is described by the displacement field, $\vec{u}$, of points in the line with respect to a stress-free initial configuration. Assuming that the displacements from the reference configuration are small, the line deformation is characterized by the total strain [151]

$$\varepsilon_{ij} = \frac{1}{2}\left(\frac{\partial u_i}{\partial x_j} + \frac{\partial u_j}{\partial x_i}\right), \qquad i,j = 1,2,3 \tag{3.58}$$

which can be written in matrix notation as

$$\boldsymbol{\varepsilon} = \mathbf{S}\mathbf{u}, \tag{3.59}$$

with

$$\boldsymbol{\varepsilon} = \begin{bmatrix} \varepsilon_{11} & \varepsilon_{22} & \varepsilon_{33} & \gamma_{12} & \gamma_{23} & \gamma_{31} \end{bmatrix}^T, \tag{3.60}$$

where symmetry of the strain tensor is assumed and the engineering shear strains [151]

$$\gamma_{ij} = 2\varepsilon_{ij}, \quad i \neq j \tag{3.61}$$

are used. The strain operator $\mathbf{S}$ is given by [151]

$$\mathbf{S} = \begin{bmatrix} \dfrac{\partial}{\partial x_1} & 0 & 0 \\ 0 & \dfrac{\partial}{\partial x_2} & 0 \\ 0 & 0 & \dfrac{\partial}{\partial x_3} \\ \dfrac{\partial}{\partial x_2} & \dfrac{\partial}{\partial x_1} & 0 \\ 0 & \dfrac{\partial}{\partial x_3} & \dfrac{\partial}{\partial x_2} \\ \dfrac{\partial}{\partial x_3} & 0 & \dfrac{\partial}{\partial x_1} \end{bmatrix}. \tag{3.62}$$

The total strain has contributions from different sources: the elastic distortion of the line, the thermal strain, and the strain induced by variations in vacancy concentration. Thus, one can write, respectively,

$$\boldsymbol{\varepsilon} = \boldsymbol{\varepsilon}^e + \boldsymbol{\varepsilon}^{th} + \boldsymbol{\varepsilon}^v, \tag{3.63}$$

where

$$\varepsilon^{th} = \alpha(T - T_0)\mathbf{I}, \tag{3.64}$$

is the thermal strain, and

$$\varepsilon^{v} = \frac{1}{3}\varepsilon^{v}\mathbf{I}, \tag{3.65}$$

is the electromigration induced strain, with ε^{v} determined from equation (3.42).

Assuming an elastic deformation of the interconnect, which means that Hooke's law applies, the stress is related to the elastic strain by

$$\boldsymbol{\sigma} = \mathbf{C}\varepsilon^{e}, \tag{3.66}$$

which together with (3.63) yields

$$\boldsymbol{\sigma} = \mathbf{C}(\varepsilon - \varepsilon_0), \tag{3.67}$$

where

$$\varepsilon_0 = \varepsilon^{th} + \varepsilon^{v}, \tag{3.68}$$

represents the total inelastic strain. Here, the stresses should satisfy the mechanical equilibrium equations [151]

$$\begin{aligned}
\frac{\partial\sigma_{11}}{\partial x_1} + \frac{\partial\sigma_{21}}{\partial x_2} + \frac{\partial\sigma_{31}}{\partial x_3} &= 0, \\
\frac{\partial\sigma_{12}}{\partial x_1} + \frac{\partial\sigma_{22}}{\partial x_2} + \frac{\partial\sigma_{32}}{\partial x_3} &= 0, \\
\frac{\partial\sigma_{13}}{\partial x_1} + \frac{\partial\sigma_{23}}{\partial x_2} + \frac{\partial\sigma_{33}}{\partial x_3} &= 0,
\end{aligned} \tag{3.69}$$

since it is assumed that there are no external forces acting on the line during electromigration. Equation (3.69) can be conveniently expressed by the form

$$\nabla \cdot \boldsymbol{\sigma} = 0. \tag{3.70}$$

3.6 Model Summary

The developed electromigration model consists of several submodels. The electrical and temperature distribution in the interconnect is determined by the system of equations

$$\nabla \cdot (\gamma_E \nabla \varphi) = 0, \tag{3.71}$$

$$\nabla \cdot (\gamma_T \nabla T) = \rho_m c_p \frac{\partial T}{\partial t} - \gamma_E \left(\nabla \varphi\right)^2, \tag{3.72}$$

with temperature dependent conductivities

$$\gamma(T) = \frac{\gamma_0}{1 + \alpha(T - T_0) + \beta(T - T_0)^2}. \tag{3.73}$$

The vacancy flux is given by

$$\vec{J}_v = -\mathbf{D}\left(\nabla C_v + \frac{|Z^*|e}{kT}C_v\nabla\varphi - \frac{Q^*}{kT^2}C_v\nabla T + \frac{f\Omega}{kT}C_v\nabla\sigma\right), \tag{3.74}$$

which takes into account all driving forces for vacancy transport. The vacancy dynamics is then described by the equations

$$\frac{\partial C_v}{\partial t} = -\nabla \cdot \vec{J}_v + G, \tag{3.75}$$

$$G = \frac{\partial C_{im}}{\partial t} = \frac{1}{\tau} \left[C_{veq} - C_{im} \left(1 + \frac{\omega_R}{\omega_T C_v} \right) \right] = \frac{1}{\tau} \left(C_{veq} - q C_{im} \right), \tag{3.76}$$

where the latter is calculated at grain boundaries and interfaces only.

The trace of the total electromigration strain is calculated by

$$\frac{\partial \varepsilon^v}{\partial t} = \Omega \left[(1 - f) \nabla \cdot \vec{J}_v + fG \right], \tag{3.77}$$

which together with (3.75) and (3.76) can be conveniently expressed as

$$\frac{\partial \varepsilon^v}{\partial t} = -\Omega(1 - f) \frac{\partial C_v}{\partial t} + \Omega \frac{\partial C_{im}}{\partial t}. \tag{3.78}$$

The resultant line deformation and mechanical stress is determined by the set of equations

$$\varepsilon = \mathbf{Su}, \tag{3.79}$$

$$\nabla \cdot \boldsymbol{\sigma} = 0, \tag{3.80}$$

$$\boldsymbol{\sigma} = \mathbf{C}(\varepsilon - \varepsilon_0), \tag{3.81}$$

where

$$\varepsilon_0 = \frac{1}{3} \varepsilon^v \mathbf{I}. \tag{3.82}$$

The solution of these equations allows a complete cycle of simulation of electromigration in general three-dimensional interconnet structures.

Chapter 4

Numerical Implementation

The mathematical description of physical phenomena very frequently consits of partial differential equations (PDE's) defined in a given domain of interest. Usually, these equations can be analytically solved only for very simple problems. Thus, for complex geometries and problems, involving variable material properties and general boundary conditions, numerical methods have to be applied.

Considering the model proposed in Chapter 3, the finite element method (FEM) has been chosen as numerical solving procedure. It presents a solid mathematical formulation for solving several types of PDE's and can handle complex geometries with different types of boundary conditions. Moreover, since it was originally devised for solving mechanical problems, it is rather convenient for the model implementation.

This chapter begins with a brief introduction to the finite element method, where the basic ideas are presented. A rigorous mathematical treatment is beyond the scope of this work and can be found elsewhere [151, 152, 153, 154]. Then, the discretization of the model equations given in Chapter 3 is presented, followed by the description of the numerical implementation in a TCAD simulation tool.

4.1 The Finite Element Method

Consider the PDE

$$L[u(\vec{r})] = f(\vec{r}), \tag{4.1}$$

defined in a domain Ω, where $L[\cdot]$ represents a linear differential operator, $u(\vec{r})$ is the unknown function to be determined, and $f(\vec{r})$ is a given source function. The finite element method consists in discretizing the continuum problem (4.1), so that an approximate solution can be found by solving an algebraic system of equations.

Two main approaches for obtaining the approximate solution are the Ritz method and Galerkin's method [152]. The Ritz method is based on a variational formulation of the PDE, which corresponds to a minimization problem of a functional [152]. Since Galerkin's method allows for more general variational formulations [152], Galerkin's approach is used throughout this work.

4.1.1 Galerkin's Method

Multiplying (4.1) by a function $v(\vec{r})$, which is called test or trial function, and integrating over the simulation domain gives the variational formulation

$$\int_\Omega v(\vec{r}) L[u(\vec{r})] d\Omega = \int_\Omega v(\vec{r}) f(\vec{r}) d\Omega. \tag{4.2}$$

Using the notation

$$(a, b) = \int_\Omega a(\vec{r}) b(\vec{r}) d\Omega, \tag{4.3}$$

(4.2) can be written as

$$(L[u], v) = (f, v). \tag{4.4}$$

In order to obtain the corresponding discrete problem, the simulation domain, Ω, is divided in a set of m elements, $T_1, T_2, ..., T_m$, which do not overlap, i.e. $\forall i \neq j : T_i \cap T_j = 0$. The mesh obtained by such a domain discretization is represented by

$$T_h(\Omega) = \bigcup_{i=1}^{m} T_i. \tag{4.5}$$

Further, one defines a set P of grid points, also called nodes, with each point $p_k \in P$ being described by a unique global index $k = 1, 2, ..., N$, where N is the total number of grid points in the mesh.

The approximate solution, $u_h(\vec{r})$, for the unknown function, $u(\vec{r})$, is given by [152]

$$u_h(\vec{r}) = \sum_{i=1}^{N} u_i N_i(\vec{r}), \tag{4.6}$$

where $N_i(\vec{r})$ are the so-called basis (or shape) functions. The approximate solution of (4.4) is determined by the coefficients u_i, which represent the value of the unknown function at the node i. At the node i, where the point is given by the coordinates $\vec{r}_i$, the basis functions must satisfy the condition

$$N_j(\vec{r}_i) = \delta_{ij}, \qquad i, j = 1, ..., N. \tag{4.7}$$

Typically, the basis functions are chosen to be low order polynomials.

Substituting (4.6) in (4.4), and choosing $v = N_j(\vec{r})$ one obtains

$$\left(L[\sum_{i=1}^{N} u_i N_i], N_j \right) = (f, N_j), \qquad j = 1, ..., N, \tag{4.8}$$

and since $L[\cdot]$ is a linear operator and the coefficients u_i are constants one can write

$$\sum_{i=1}^{N} u_i \left(L[N_i], N_j \right) = (f, N_j), \qquad j = 1, ..., N. \tag{4.9}$$

Equation (4.9) is, in fact, a linear system of N equations with N unknowns, $u_1, u_2, ..., u_N$. Thus, it can be written in matrix notation as

$$\mathbf{A}\mathbf{x} = \mathbf{b}, \tag{4.10}$$

where $\mathbf{A} = (a_{ij})$ is called stiffness matrix, given by the elements

$$a_{ij} = (L[N_i], N_j) = \int_\Omega L[N_i(\vec{r})]N_j(\vec{r})d\Omega, \qquad i, j = 1, ..., N, \tag{4.11}$$

$\mathbf{x} = (u_1, ..., u_N)^T$ is the vector of unknown coefficients, and $\mathbf{b} = (b_1, ..., b_N)^T$ is the load vector, given by

$$b_j = (f, N_j) = \int_\Omega f(\vec{r})N_j(\vec{r})d\Omega, \qquad j = 1, ..., N. \tag{4.12}$$

4.1.2 Assembly

Applying the finite element method to solve a given PDE leads to an algebraic system of equations. In order to solve this system of equations, the global stiffness matrix, $\mathbf{A}$, and the load vector, $\mathbf{b}$, have to be determined. However, instead of computing them using directly (4.11) and (4.12), in practice they are computed by summing the contributions from the different elements [152, 153, 154] according to

$$a_{ij} = \sum_{T \in T_h(\Omega)} (L[N_i], N_j)_T = \sum_{T \in T_h(\Omega)} \int_T L[N_i(\vec{r})]N_j(\vec{r})d\Omega, \qquad i, j = 1, ..., N \tag{4.13}$$

$$b_j = \sum_{T \in T_h(\Omega)} (f, N_j)_T = \sum_{T \in T_h(\Omega)} \int_T f(\vec{r})N_j(\vec{r})d\Omega, \qquad j = 1, ..., N. \tag{4.14}$$

Note that $(L[N_i], N_j)_T = 0$ unless both N_i and N_j belong to the same element T. Thus, the calculations (4.13) and (4.14) can be limited to the nodes of the element T, so that $i, j = 1, ..., N_V$, where N_V is the number of vertices of the element. In this way, for each element $T \in T_h(\Omega)$, a $N_V \times N_V$ matrix is obtained, which is called element stiffness or nucleus matrix. Thus, the general system matrix, $\mathbf{A}$, can be computed by first computing the nucleus matrices for each $T \in T_h(\Omega)$ and then summing the contributions from each element according to (4.13) [152]. The right-hand side vector, $\mathbf{b}$, is computed in the same way. This process of constructing the general system matrix is called assembly [152]. The main advantage of this assembly process is that it greatly simplifies the computation of the system matrix and right-hand side vector, since (4.11) and (4.12) can be easily calculated for each element of the domain discretization.

4.1.3 Shape Function

The shape function is the function which interpolates the solution between the discrete values obtained at the mesh nodes. Therefore, appropriate functions have to be used and, as already mentioned, low order polynomials are typically chosen as shape functions. In this work linear shape functions are used.

For three-dimensional finite element simulations it is convenient to discretize the simulation domain using tetrahedrons, as depicted in Figure 4.1. Thus, linear shape functions must be defined for each tetrahedron of the mesh, in order to apply the Galerkin method described in Section 4.1.1.
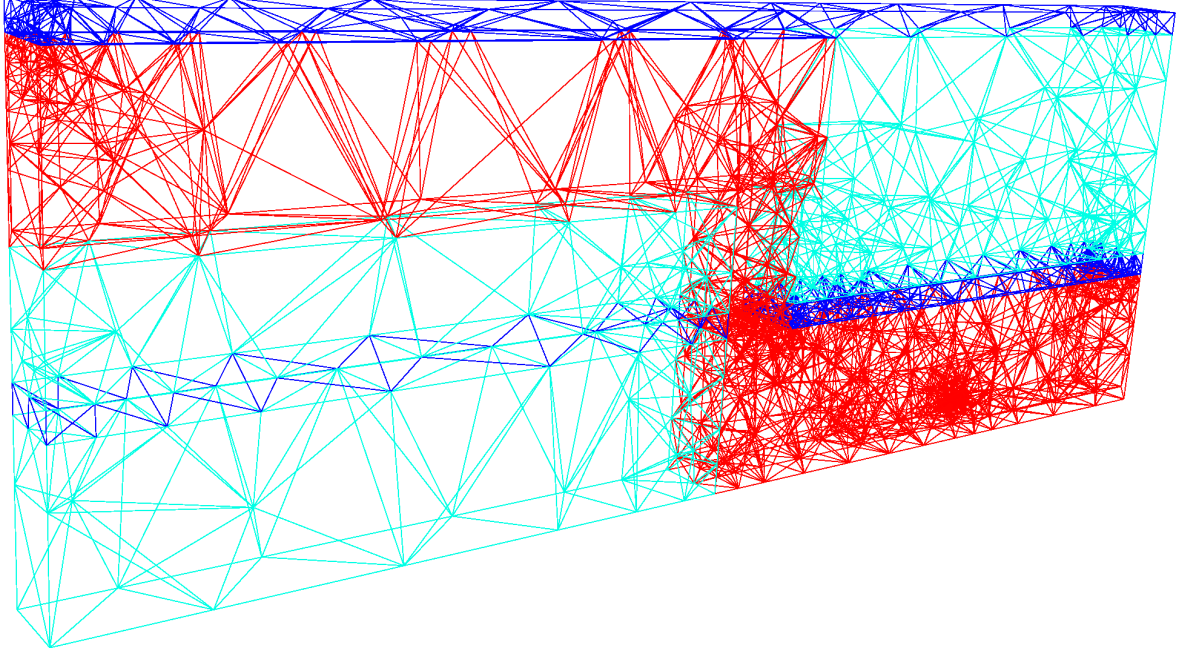
Figure 4.1: Finite element mesh of a three-dimensional interconnect structure discretized with tetrahedrons.

Consider a tetrahedron in a cartesian system as depicted in Figure 4.2(a). The linear shape function of the node i has the form [153]

$$N_i(x, y, z) = a_i + b_i x + c_i y + d_i z, \tag{4.15}$$

where $i = 1, ..., 4$. The coefficients, a_i, b_i, c_i, and d_i for each nodal basis function of the tetrahedral element can be calculated considering the condition [152]

$$N_j(\vec{r_i}) = \delta_{ij}, \qquad i, j = 1, ..., 4. \tag{4.16}$$

As a result, a system of 4 equations for the 4 unknown coefficients is obtained. This procedure has to be repeated for all tetrahedrons of the mesh, so that the basis functions of all grid nodes are determined. Furthermore, in order to obtain the discrete system of equations (4.9), the shape functions have to be derived and integrated, as shown by (4.11) and (4.12).

The calculations can be significantly simplified by carring out a coordinate transformation. A tetrahedron in a transformed coordinate system is shown in Figure 4.2(b). Each point (x, y, z) of the tetrahedron in the original coordinate system can be mapped to a corresponding

point (ξ, η, ζ) in the transformed coordinate system [155]

$$
\begin{aligned}
x &= x_1 + (x_2 - x_1)\xi + (x_3 - x_1)\eta + (x_4 - x_1)\zeta, \\
y &= y_1 + (y_2 - y_1)\xi + (y_3 - y_1)\eta + (y_4 - y_1)\zeta, \\
z &= z_1 + (z_2 - z_1)\xi + (z_3 - z_1)\eta + (z_4 - z_1)\zeta,
\end{aligned}
\tag{4.17}
$$

which in matrix form leads to the Jacobian matrix

$$
\mathbf{J} = \begin{bmatrix}
x_2 - x_1 & x_3 - x_1 & x_4 - x_1 \\
y_2 - y_1 & y_3 - y_1 & y_4 - y_1 \\
z_2 - z_1 & z_3 - z_1 & z_4 - z_1
\end{bmatrix}.
\tag{4.18}
$$

In this way, the nodal basis functions for the tetrahedron in the transformed coordinate system are given by [155]

$$
\begin{aligned}
N_1^t(\xi, \eta, \zeta) &= 1 - \xi - \eta - \zeta, \\
N_2^t(\xi, \eta, \zeta) &= \xi, \\
N_3^t(\xi, \eta, \zeta) &= \eta, \\
N_4^t(\xi, \eta, \zeta) &= \zeta.
\end{aligned}
\tag{4.19}
$$

These shape functions are rather simple, so that the derivatives and integrals required for the finite element formulation can be readily evaluated in the transformed coordinate system. Given a function $f(x, y, z)$, the gradient in the transformed coordinates is of the form

$$
\nabla^t f = \begin{bmatrix} \dfrac{\partial f}{\partial \xi} & \dfrac{\partial f}{\partial \eta} & \dfrac{\partial f}{\partial \zeta} \end{bmatrix}^T,
\tag{4.20}
$$

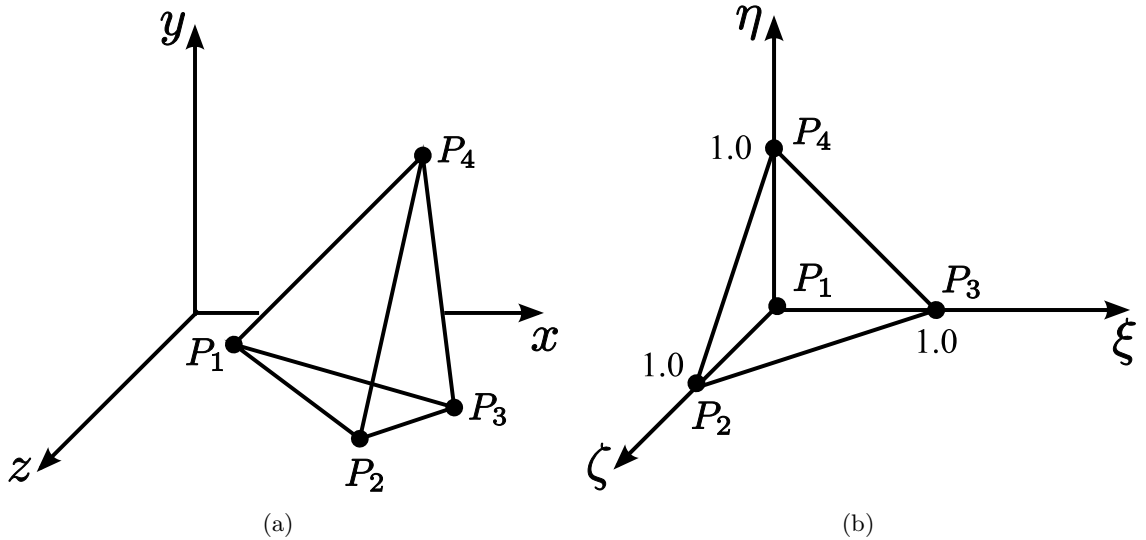(a)   (b)

Figure 4.2: Tetrahedral finite element. (a) Original coordinate system. (b) Transformed coordinate system.

where the derivatives are calculated via the chain rule by

$$
\begin{aligned}
\frac{\partial f}{\partial \xi} &= \frac{\partial f}{\partial x}\frac{\partial x}{\partial \xi} + \frac{\partial f}{\partial y}\frac{\partial y}{\partial \xi} + \frac{\partial f}{\partial z}\frac{\partial z}{\partial \xi}, \\
\frac{\partial f}{\partial \eta} &= \frac{\partial f}{\partial x}\frac{\partial x}{\partial \eta} + \frac{\partial f}{\partial y}\frac{\partial y}{\partial \eta} + \frac{\partial f}{\partial z}\frac{\partial z}{\partial \eta}, \\
\frac{\partial f}{\partial \zeta} &= \frac{\partial f}{\partial x}\frac{\partial x}{\partial \zeta} + \frac{\partial f}{\partial y}\frac{\partial y}{\partial \zeta} + \frac{\partial f}{\partial z}\frac{\partial z}{\partial \zeta}.
\end{aligned}
\tag{4.21}
$$

These equations can be expressed in matrix notation as

$$
\begin{bmatrix} \dfrac{\partial f}{\partial \xi} \\[2mm] \dfrac{\partial f}{\partial \eta} \\[2mm] \dfrac{\partial f}{\partial \zeta} \end{bmatrix}
=
\begin{bmatrix} \dfrac{\partial x}{\partial \xi} & \dfrac{\partial y}{\partial \xi} & \dfrac{\partial z}{\partial \xi} \\[2mm] \dfrac{\partial x}{\partial \eta} & \dfrac{\partial y}{\partial \eta} & \dfrac{\partial z}{\partial \eta} \\[2mm] \dfrac{\partial x}{\partial \zeta} & \dfrac{\partial y}{\partial \zeta} & \dfrac{\partial z}{\partial \zeta} \end{bmatrix}
\cdot
\begin{bmatrix} \dfrac{\partial f}{\partial x} \\[2mm] \dfrac{\partial f}{\partial y} \\[2mm] \dfrac{\partial f}{\partial z} \end{bmatrix},
\tag{4.22}
$$

or

$$
\nabla^t f = \mathbf{J}^T \nabla f,
\tag{4.23}
$$

where $\mathbf{J}^T$ is the transpose of the Jacobian matrix. Thus, the gradient in the original coordinate system can be calculated using the transformed coordinate gradient by

$$
\nabla f = \left(\mathbf{J}^T\right)^{-1} \nabla^t f = \mathbf{\Lambda} \nabla^t f,
\tag{4.24}
$$

where $\mathbf{\Lambda} = \left(\mathbf{J}^T\right)^{-1}$.

Performing such a coordinate transformation significantly simplifies the practical implementation of the FEM. The nodal shape functions in the transformed coordinates are fixed and known in advance, thus, it is not necessary to solve the system of equations formed by (4.15) and (4.16) for each element of the mesh. Only the Jacobian matrix has to be determined, and the required calculations for the finite element formulation can be easily evaluated.

4.2   Discretization of the Model Equations

In this section the discretization of the equations to be solved during electromigration simulation is presented. The corresponding set of equations is summarized in Section 3.6.

4.2.1   Discretization of Laplace's Equation

The electric potential is calculated from equation (3.71). Multiplying it by a test function $N_p = N_p(\vec{r})$, and integrating over the domain Ω one obtains

$$
\int_{\Omega} \left[\nabla \cdot (\gamma_E \nabla \varphi)\right] N_p \; d\Omega = 0, \qquad p = 1, ..., N.
\tag{4.25}
$$

Using Green's formula [152]

$$\int_\Omega v\nabla^2 w \; d\Omega + \int_\Omega \nabla v \cdot \nabla w \; d\Omega = \int_\Gamma v\frac{\partial w}{\partial \vec{n}} \; d\Gamma, \tag{4.26}$$

where $\partial w/\partial\vec{n}$ represents the normal derivative in the outward normal direction to the boundary Γ, and assuming a Neumann boundary condition, i.e. vanishing normal derivatives, on Γ, equation (4.25) can be written as

$$- \int_\Omega \gamma_E \nabla\varphi \cdot \nabla N_p \; d\Omega = 0, \qquad p = 1, ..., N. \tag{4.27}$$

Since the electrical conductivity γ_E depends on the temperature according to (3.73) and varies along the simulation domain, it is part of the integrand in (4.27). However, in a single element the conductivity is assumed to be constant, being determined by the average of the temperature on the element nodes, i.e. $\gamma_E = \gamma_E(\bar{T})$ with

$$\bar{T} = \frac{T_1 + T_2 + T_3 + T_4}{4}, \tag{4.28}$$

for a tetrahedral element. Applying the discretization for the electric potential as in (4.6),

$$\varphi(\vec{r}, t = t_n) = \varphi^n = \sum_{i=1}^{4} \varphi_i^n N_i(\vec{r}), \tag{4.29}$$

where φ_i^n is the electric potential of the node i at a time t_n, equation (4.27) for a single element becomes

$$- \gamma_E \sum_{i=1}^{4} \varphi_i^n \int_T \nabla N_i \cdot \nabla N_p \; d\Omega = 0, \qquad p = 1, ..., 4. \tag{4.30}$$

Using the shorthand notation

$$K_{ip} = \int_T \nabla N_i \cdot \nabla N_p \; d\Omega$$
$$= \det(\mathbf{J}) \int_0^1 \int_0^{1-\xi} \int_0^{1-\xi-\eta} \boldsymbol{\Lambda}\nabla^t N_i^t \cdot \boldsymbol{\Lambda}\nabla^t N_p^t \; d\zeta d\eta d\xi, \tag{4.31}$$

where the last term is the calculation in the transformed coordinate system, (4.30) is rewritten as

$$- \gamma_E \sum_{i=1}^{4} \varphi_i^n K_{ip} = 0, \qquad p = 1, ..., 4, \tag{4.32}$$

which corresponds to a discrete system of 4 equations with 4 unknowns, i.e. the electric potential at each node of the tetrahedral element.

4.2.2 Discretization of the Thermal Equation

For convenience, the thermal equation (3.72) is rewritten here as

$$\rho_m c_p \dot{T} - \nabla \cdot (\gamma_T \nabla T) - \gamma_E (\nabla \varphi)^2 = 0, \tag{4.33}$$

where the notation $\dot{T} = \partial T / \partial t$ is used. Following the same procedure as for Laplace's equation, one multiplies (4.33) by $N_p(\vec{r})$ and integrates over the domain Ω, which together with Green's formula (4.26) and a Neumann boundary condition yields the weak formulation

$$\int_\Omega \rho_m c_p \dot{T} N_p \, d\Omega + \int_\Omega \gamma_T \nabla T \cdot \nabla N_p \, d\Omega - \int_\Omega \gamma_E (\nabla \varphi)^2 N_p \, d\Omega = 0, \quad p = 1, ..., N. \tag{4.34}$$

The thermal equation (4.33) corresponds to a parabolic problem. Besides the spatial discretization, a discretization in time has also to be performed. A simple choice is the backward Euler method

$$\dot{T} = \frac{T^n - T^{n-1}}{\Delta t_n}, \tag{4.35}$$

where $\Delta t_n = t^n - t^{n-1}$ is the time step. Applying now the spatial discretization for the temperature variable

$$T^n = \sum_{j=1}^4 T_j^n N_j(\vec{r}), \tag{4.36}$$

and the electric potential discretization (4.29), equation (4.34) is written for a single element as

$$\rho_m c_p \sum_{j=1}^4 T_j^n \int_T N_j N_p \, d\Omega - \rho_m c_p \sum_{j=1}^4 T_j^{n-1} \int_T N_j N_p \, d\Omega + \Delta t_n \gamma_T \sum_{j=1}^4 T_j^n \int_T \nabla N_j \cdot \nabla N_p \, d\Omega$$

$$- \Delta t_n \gamma_E \sum_{i=1}^4 \sum_{q=1}^4 \varphi_i^n \varphi_q^n \int_T (\nabla N_i \cdot \nabla N_q) N_p \, d\Omega = 0, \qquad p = 1, ..., 4. \tag{4.37}$$

Using the integral notations (4.31),

$$M_{jp} = \int_T N_j N_p \, d\Omega = \det(\mathbf{J}) \int_0^1 \int_0^{1-\xi} \int_0^{1-\xi-\eta} N_j^t N_p^t \, d\zeta d\eta d\xi, \tag{4.38}$$

and

$$\Theta_{iqp} = \int_T (\nabla N_i \cdot \nabla N_q) N_p \, d\Omega$$

$$= \det(\mathbf{J}) \int_0^1 \int_0^{1-\xi} \int_0^{1-\xi-\eta} \left(\mathbf{\Lambda} \nabla^t N_i^t \cdot \mathbf{\Lambda} \nabla^t N_q^t \right) N_p^t \, d\zeta d\eta d\xi, \tag{4.39}$$

(4.37) can be expressed as

$$\rho_m c_p \sum_{j=1}^4 T_j^n M_{jp} - \rho_m c_p \sum_{j=1}^4 T_j^{n-1} M_{jp} + \Delta t_n \gamma_T \sum_{j=1}^4 T_j^n K_{jp}$$

$$- \Delta t_n \gamma_E \sum_{i=1}^4 \sum_{q=1}^4 \varphi_i^n \varphi_q^n \Theta_{iqp} = 0, \qquad p = 1, ..., 4. \tag{4.40}$$

This is the discrete system of equations, which has to be solved each time step in order to obtain the temperature at each node of the element.

4.2.3   Discretization of the Vacancy Balance Equation

The combination of (3.74) with (3.75) and (3.76) yields the vacancy balance equation

$$
\frac{\partial C_v}{\partial t} + \nabla \cdot \left[-D_v \left(\nabla C_v + \frac{|Z^*|e}{kT} C_v \nabla \varphi - \frac{Q^*}{kT^2} C_v \nabla T + \frac{f\Omega}{kT} C_v \nabla \sigma \right) \right]
$$
$$
+ \frac{1}{\tau} \left(q C_{im} - C_{veq} \right) = 0, \tag{4.41}
$$

for which the weak formulation of the form

$$
\int_\Omega \frac{\partial C_v}{\partial t} N_p \, d\Omega + D_v \left[\int_\Omega \nabla C_v \cdot \nabla N_p \, d\Omega + \frac{|Z^*|e}{k\bar{T}} \int_\Omega C_v \left(\nabla \varphi \cdot \nabla N_p \right) \, d\Omega \right.
$$
$$
\left. - \frac{Q^*}{k\bar{T}^2} \int_\Omega C_v \left(\nabla T \cdot \nabla N_p \right) \, d\Omega + \frac{f\Omega}{k\bar{T}} \int_\Omega C_v \left(\nabla \sigma \cdot \nabla N_p \right) \, d\Omega \right] \tag{4.42}
$$
$$
+ \int_\Omega \frac{1}{\tau} \left(q C_{im} - C_{veq} \right) N_p \, d\Omega = 0, \quad p = 1, ..., N,
$$

is obtained under the assumption of a Neumann boundary condition. Applying the electric potential and the temperature discretization, (4.29) and (4.36), respectively, together with

$$
C_v^n = \sum_{k=1}^{4} C_{v,k}^n N_k(\vec{r}), \tag{4.43}
$$

$$
\sigma^n = \sum_{l=1}^{4} \sigma_l^n N_l(\vec{r}), \tag{4.44}
$$

$$
C_{im}^n = \sum_{m=1}^{4} C_{im,m}^n N_m(\vec{r}), \tag{4.45}
$$

and the backward Euler time discretization, the vacancy balance equation discretized in a single element is given by

$$
\sum_{k=1}^{4} C_{v,k}^n \int_T N_k N_p \, d\Omega - \sum_{k=1}^{4} C_{v,k}^{n-1} \int_T N_k N_p \, d\Omega + \Delta t_n D_v \left[\sum_{k=1}^{4} C_{v,k}^n \int_T \nabla N_k \cdot \nabla N_p \, d\Omega \right.
$$
$$
+ \frac{|Z^*|e}{k\bar{T}} \sum_{i=1}^{4} \sum_{k=1}^{4} \varphi_i^n C_{v,k}^n \int_T \left(\nabla N_i \cdot \nabla N_p \right) N_k \, d\Omega
$$
$$
- \frac{Q^*}{k\bar{T}^2} \sum_{j=1}^{4} \sum_{k=1}^{4} T_j^n C_{v,k}^n \int_T \left(\nabla N_j \cdot \nabla N_p \right) N_k \, d\Omega \tag{4.46}
$$
$$
+ \left. \frac{f\Omega}{k\bar{T}} \sum_{l=1}^{4} \sum_{k=1}^{4} \sigma_l^n C_{v,k}^n \int_T \left(\nabla N_l \cdot \nabla N_p \right) N_k \, d\Omega \right]
$$
$$
+ \frac{\Delta t_n}{\tau} \left(q \sum_{m=1}^{4} C_{im,m}^n \int_T N_m N_p \, d\Omega - C_{veq} \int_T N_p \, d\Omega \right) = 0, \qquad p = 1, ..., 4
$$

under the assumption that τ, q, and C_{veq} are constant inside an element.

Using the shorthand notation (4.31), (4.38), (4.39), and

$$V_p = \int_T N_p \, d\Omega = \det(\mathbf{J}) \int_0^1 \int_0^{1-\xi} \int_0^{1-\xi-\eta} N_p^t \, d\zeta d\eta d\xi, \tag{4.47}$$

(4.46) is written as

$$\sum_{k=1}^4 C_{v,k}^n M_{kp} - \sum_{k=1}^4 C_{v,k}^{n-1} M_{kp} + \Delta t_n D_v \left[\sum_{k=1}^4 C_{v,k}^n K_{kp} + \frac{|Z^*|e}{k\bar{T}} \sum_{i=1}^4 \sum_{k=1}^4 \varphi_i^n C_{v,k}^n \Theta_{ipk} \right.$$
$$\left. - \frac{Q^*}{k\bar{T}^2} \sum_{j=1}^4 \sum_{k=1}^4 T_j^n C_{v,k}^n \Theta_{jpk} + \frac{f\Omega}{k\bar{T}} \sum_{l=1}^4 \sum_{k=1}^4 \sigma_l^n C_{v,k}^n \Theta_{lpk} \right] \tag{4.48}$$
$$+ \frac{\Delta t_n}{\tau} \left(q \sum_{m=1}^4 C_{im,m}^n M_{mp} - C_{veq} V_p \right) = 0, \qquad p = 1, ..., 4.$$

In the above derivation the vacancy diffusivity is treated as a scalar diffusion coefficient. In order to take into account the anisotropy of diffusivity due to the mechanical stress, as presented in Section 3.2.2, a diffusivity tensor must be applied. This requires a slight modification of (4.48) to

$$\sum_{k=1}^4 C_{v,k}^n M_{kp} - \sum_{k=1}^4 C_{v,k}^{n-1} M_{kp} + \Delta t_n \left[\sum_{k=1}^4 C_{v,k}^n K_{kp} + \frac{|Z^*|e}{k\bar{T}} \sum_{i=1}^4 \sum_{k=1}^4 \varphi_i^n C_{v,k}^n \Theta_{ipk} \right.$$
$$\left. - \frac{Q^*}{k\bar{T}^2} \sum_{j=1}^4 \sum_{k=1}^4 T_j^n C_{v,k}^n \Theta_{jpk} + \frac{f\Omega}{k\bar{T}} \sum_{l=1}^4 \sum_{k=1}^4 \sigma_l^n C_{v,k}^n \Theta_{lpk} \right] \tag{4.49}$$
$$+ \frac{\Delta t_n}{\tau} \left(q \sum_{m=1}^4 C_{im,m}^n M_{mp} - C_{veq} V_p \right) = 0, \qquad p = 1, ..., 4.$$

where the diffusivity tensor $\mathbf{D}$ is now incorporated into K_{kp} and Θ_{ipk}, given by

$$K_{ip} = \int_T \mathbf{D}\nabla N_i \cdot \nabla N_p \, d\Omega, \tag{4.50}$$

and

$$\Theta_{ipk} = \int_T \left(\mathbf{D}\nabla N_i \cdot \nabla N_p \right) N_k \, d\Omega. \tag{4.51}$$

At material interfaces and grain boundaries the trapped vacancy concentration is governed by (3.76), rewritten here as

$$\frac{\partial C_{im}}{\partial t} - \frac{1}{\tau} \left(C_{veq} - qC_{im} \right) = 0. \tag{4.52}$$

The finite element formulation of this equation follows the same procedure described above, which yields the discretization

$$\sum_{m=1}^{4} C_{im,m}^{n} M_{mp} - \sum_{m=1}^{4} C_{im,m}^{n-1} M_{mp}$$

$$+ q \frac{\Delta t_n}{\tau} \sum_{m=1}^{4} C_{im,m}^{n} M_{mp} - \frac{\Delta t_n}{\tau} C_{veq} V_p = 0, \qquad p = 1, ..., 4. \tag{4.53}$$

4.2.4 Discretization of the Mechanical Equations

The deformation in a three-dimensional body is expressed by the displacement field

$$\vec{d}(\vec{r}) = \begin{bmatrix} u(\vec{r}) \\ v(\vec{r}) \\ w(\vec{r}) \end{bmatrix}, \tag{4.54}$$

where $u(\vec{r})$, $v(\vec{r})$, and $w(\vec{r})$ are the displacements in the x, y, and z direction, respectively. The displacement is discretized on a tetrahedral element as [151]

$$\vec{d}(\vec{r}) = \sum_{i=1}^{4} \vec{d_i} N_i(\vec{r}), \tag{4.55}$$

which leads to the components discretization

$$u(\vec{r}) = \sum_{i=1}^{4} u_i^n N_i(\vec{r}), \quad v(\vec{r}) = \sum_{i=1}^{4} v_i^n N_i(\vec{r}), \quad w(\vec{r}) = \sum_{i=1}^{4} w_i^n N_i(\vec{r}). \tag{4.56}$$

Applying this discretization in the strain-displacement relationship (3.79), the components of the strain tensor can be written as

$$\varepsilon = \mathbf{Bd} = \begin{bmatrix} \mathbf{B_1} & \mathbf{B_2} & \mathbf{B_3} & \mathbf{B_4} \end{bmatrix} \mathbf{d}, \tag{4.57}$$

where $\mathbf{B_i}$ is the matrix of the derivatives of the shape functions for the node i [151]

$$\mathbf{B_i} = \begin{bmatrix} \dfrac{\partial N_i}{\partial x} & 0 & 0 \\ 0 & \dfrac{\partial N_i}{\partial y} & 0 \\ 0 & 0 & \dfrac{\partial N_i}{\partial z} \\ \dfrac{\partial N_i}{\partial y} & \dfrac{\partial N_i}{\partial x} & 0 \\ 0 & \dfrac{\partial N_i}{\partial z} & \dfrac{\partial N_i}{\partial y} \\ \dfrac{\partial N_i}{\partial z} & 0 & \dfrac{\partial N_i}{\partial x} \end{bmatrix}, \quad i = 1, \dots, 4, \tag{4.58}$$

and the displacement matrix

$$\mathbf{d} = \begin{bmatrix} \vec{d_1} \\ \vec{d_2} \\ \vec{d_3} \\ \vec{d_4} \end{bmatrix}. \tag{4.59}$$

Using (4.57), the stress-strain equation (3.81) can written as a function of the displacements according to

$$\boldsymbol{\sigma} = \mathbf{C}(\boldsymbol{\varepsilon} - \boldsymbol{\varepsilon}_0) = \mathbf{CBd} - \mathbf{C}\boldsymbol{\varepsilon}_0. \tag{4.60}$$

Applying the principle of virtual work, the work of internal stresses on a continuous elastic body is given by [151]

$$W_{in} = \int_{\Omega} \boldsymbol{\varepsilon}^T \boldsymbol{\sigma} \; d\Omega, \tag{4.61}$$

where $\boldsymbol{\varepsilon}^T$ is the transposed strain tensor. Combining (4.57), (4.60), and (4.61) the work on a finite element is written as

$$W_{in}^{el} = \mathbf{d}^T \int_T \left(\mathbf{B}^T \mathbf{CBd} - \mathbf{B}^T \mathbf{C}\boldsymbol{\varepsilon}_0 \right) d\Omega. \tag{4.62}$$

From energy balance the internal work should be equal to the work done by external forces, i.e. $W_{in} = W_{ext}$, and, since during electromigration there are no external forces ($W_{ext} = 0$), one obtains

$$\int_T \left(\mathbf{B}^T \mathbf{CBd} - \mathbf{B}^T \mathbf{C}\boldsymbol{\varepsilon}_0 \right) d\Omega = 0, \tag{4.63}$$

or

$$\int_T \mathbf{B}^T \mathbf{CBd} \; d\Omega = \int_T \mathbf{B}^T \mathbf{C}\boldsymbol{\varepsilon}_0 \; d\Omega, \tag{4.64}$$

which can be conveniently expressed as

$$\mathbf{Kd} = \mathbf{f_{in}}, \tag{4.65}$$

where

$$\mathbf{K} = \int_T \mathbf{B}^T \mathbf{CB} \; d\Omega, \tag{4.66}$$

is the so-called stiffness matrix, and

$$\mathbf{f_{in}} = \int_T \mathbf{B}^T \mathbf{C}\boldsymbol{\varepsilon}_0 \; d\Omega, \tag{4.67}$$

is the internal force vector.

Equation (4.65) forms a linear system of equations of 12 equations with 12 unknowns (the three displacement components u, v, and w for each tetrahedron node). The inelastic strain $\boldsymbol{\varepsilon}_0$ determines the internal force vector according to the electromigration induced strain given by (3.78).

4.3   Simulation in FEDOS

FEDOS (Finite Element Diffusion and Oxidation Simulator) is a finite element based framework for simulating fabrication processes to be used in the microelectronics industry [155, 156]. It integrates the basic functionality required for finite element analysis, namely, assembly routines, linear and non-linear solvers, input and output operations, etc, so that the equations derived in Section 4.2 can be conveniently implemented.

Since electromigration constitutes a multi-physics problem, it is convenient to divide it into smaller subproblems and to solve each one separately. The resulting simulation scheme is depicted in Figure 4.3. The electro-thermal problem is governed by partial differential equations for the electric potential, φ, and for the temperature, T. The variables of interest for the vacancy dynamics are the vacancy concentration, C_v, and the trapped vacancy concentration at grain boundaries and interfaces, C_{im}. The mechanical problem is formulated in terms of the displacement field, $\vec{d}$, however, the mechanical stress obtained from the solution of the mechanical problem is the variable of interest here. Each subproblem is solved for the corresponding variable, while the variables of the other subproblems are fixed.
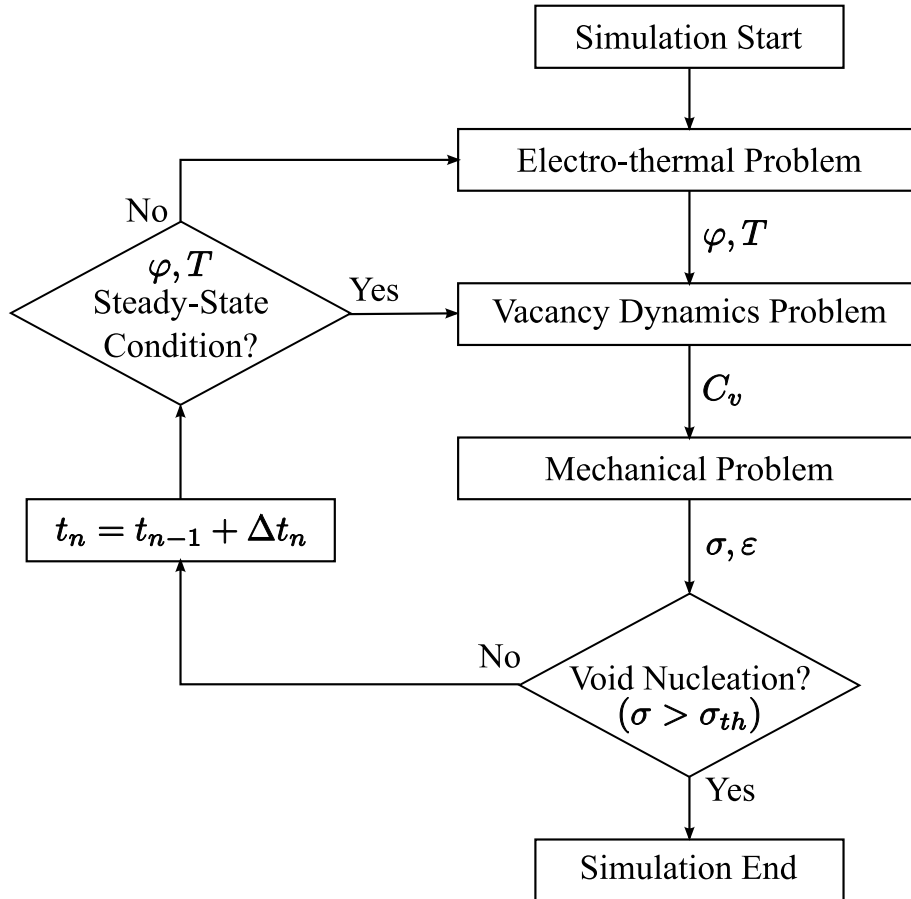

Figure 4.3: Simulation procedure of electromigration in FEDOS.

First, the solution of the electro-thermal problem determines the electric potential and temperature distribution in the interconnect. These quantities are then used to compute the vacancy concentration change due to the total mass transport occurring under electro-migration and accompanying driving forces. The rate of change of the trapped vacancy concentration at grain boundaries and other interfaces due to generation/annihilation processes is obtained. The change in vacancy concentration determines the induced strain which loads the mechanical problem. The solution of the mechanical system yields the deformation of the interconnect line, so that the mechanical stress can be calculated. If the magnitude of the developed stress reaches the threshold value for void nucleation, the simulation procedure is terminated and the corresponding time for void nucleation, and eventually interconnect failure, can be estimated. Otherwise, the time is updated and the cycle described above is repeated. Since the electric potential and temperature distribution reach a steady state condition in a time scale much shorter than that for the vacancy concentration and mechanical stress, the electro-thermal problem is typically solved only for a few initial time steps.

All subproblems are solved on the same finite element mesh. An initial mesh refinement routine may be executed in the beginning of the simulation procedure in order to appropriately solve the material transport equations at grain boundaries and material interfaces.

4.3.1 Newton's Method

The non-linear system of equations, which results from the discretization described in Section 4.2, is solved in FEDOS using the conventional Newton method [153, 154]. Generally, a non-linear system of N equations is expressed as

$$
\begin{aligned}
f_1(x_1, x_2, ..., x_N) &= 0 \\
f_2(x_1, x_2, ..., x_N) &= 0 \\
&\vdots \\
f_N(x_1, x_2, ..., x_N) &= 0
\end{aligned}
\tag{4.68}
$$

If a given solution x_j^{n-1}, $j = 1, ..., N$, is known, these equations can expanded in the vicinity of x_j^{n-1} using Taylor's series, which to the first order are approximated by

$$
f_i(x_1, ..., x_N) \approx f_i(x_1^{n-1}, ..., x_N^{n-1}) + \sum_{j=1}^{N} \frac{\partial f_i\left(x_1^{n-1}, ..., x_N^{n-1}\right)}{\partial x_j}\left(x_j - x_j^{n-1}\right) = 0,
\tag{4.69}
$$

for $i = 1, \ldots, N$. The system of equations (4.69) is written in matrix form as

$$
\mathbf{F}(\mathbf{x}^{n-1}) + \mathbf{J_N}\left(\mathbf{x} - \mathbf{x}^{n-1}\right) = 0,
\tag{4.70}
$$

where $\mathbf{J_N}$ is the so-called Jacobian matrix, for which the entries are given by

$$
J_{ij} = \frac{\partial f_i\left(x_1^{n-1}, ..., x_N^{n-1}\right)}{\partial x_j}.
\tag{4.71}
$$

Thus, the solution of (4.70) is

$$
\mathbf{x}^n = \mathbf{x}^{n-1} - \mathbf{J_N}^{-1}\ \mathbf{F}(\mathbf{x}^{n-1}).
\tag{4.72}
$$

In FEDOS, instead of using (4.72), the linear system of equations

$$\mathbf{J_N}\left(\Delta\mathbf{x}^n\right) = \mathbf{R}(\mathbf{x}^{n-1}), \tag{4.73}$$

is assembled and solved, so that the increments $\Delta\mathbf{x}^n = \mathbf{x}^n - \mathbf{x}^{n-1}$ are determined. Here, $\mathbf{R}(\mathbf{x}^{n-1}) = -\mathbf{F}(\mathbf{x}^{n-1})$ is called residual. In this way, the new approximate solution $\mathbf{x}^n$ is updated according to

$$\mathbf{x}^n = \mathbf{x}^{n-1} + \Delta\mathbf{x}^n. \tag{4.74}$$

These calculations are performed as an iterative process, where the solution of the $n-1$ iteration is used to compute the new solution. The accuracy of the new approximate solution is controlled by the conditions

$$\|\mathbf{x}^n - \mathbf{x}^{n-1}\| \leq \epsilon_{er}, \tag{4.75}$$

where ϵ_{er} is a given tolerance for the solution error, and

$$\|\mathbf{R}(\mathbf{x}^n)\| \leq \epsilon_{res}, \tag{4.76}$$

where ϵ_{res} is a given tolerance for the residual and $\|\cdot\|$ represents the Euclidean norm. The iterative procedure is terminated, if both criteria are fulfilled.

4.3.2 Assembly of the Electro-Thermal Problem

The discretization of the electrical and the thermal problem, (4.32) and (4.40), respectively, forms a non-linear system of equations for a tetrahedral element given by

$$\begin{aligned} \mathbf{F}(\boldsymbol{\varphi}, \boldsymbol{T}) &= 0 \\ \mathbf{G}(\boldsymbol{\varphi}, \boldsymbol{T}) &= 0 \end{aligned} \tag{4.77}$$

where $\mathbf{F}(\boldsymbol{\varphi}, \boldsymbol{T})$ corresponds to

$$f_p = -\gamma_E(\bar{T}) \sum_{i=1}^{4} \varphi_i^n K_{ip} = 0, \tag{4.78}$$

and $\mathbf{G}(\boldsymbol{\varphi}, \boldsymbol{T})$ to

$$\begin{aligned} g_{p+4} = \rho_m c_p \sum_{i=1}^{4} T_i^n M_{ip} - \rho_m c_p \sum_{i=1}^{4} T_i^{n-1} M_{ip} + \Delta t_n \gamma_T(\bar{T}) \sum_{i=1}^{4} T_i^n K_{ip} \\ - \Delta t_n \gamma_E(\bar{T}) \sum_{i=1}^{4} \sum_{q=1}^{4} \varphi_i^n \varphi_q^n \Theta_{iqp} = 0, \end{aligned} \tag{4.79}$$

for $p = 1, \ldots, 4$.

Applying Newton's method, the element Jacobian matrix for the electro-thermal problem has the form

$$
\mathbf{J_N} = \begin{bmatrix}
\dfrac{\partial f_1}{\partial \varphi_1^n} & \cdots & \dfrac{\partial f_1}{\partial \varphi_4^n} & \dfrac{\partial f_1}{\partial T_1^n} & \cdots & \dfrac{\partial f_1}{\partial T_4^n} \\[2mm]
\vdots & & \vdots & \vdots & & \vdots \\[2mm]
\dfrac{\partial f_4}{\partial \varphi_1^n} & \cdots & \dfrac{\partial f_4}{\partial \varphi_4^n} & \dfrac{\partial f_4}{\partial T_1^n} & \cdots & \dfrac{\partial f_4}{\partial T_4^n} \\[2mm]
\dfrac{\partial g_5}{\partial \varphi_1^n} & \cdots & \dfrac{\partial g_5}{\partial \varphi_4^n} & \dfrac{\partial g_5}{\partial T_1^n} & \cdots & \dfrac{\partial g_5}{\partial T_4} \\[2mm]
\vdots & & \vdots & \vdots & & \vdots \\[2mm]
\dfrac{\partial g_8}{\partial \varphi_1^n} & \cdots & \dfrac{\partial g_8}{\partial \varphi_4^n} & \dfrac{\partial g_8}{\partial T_1^n} & \cdots & \dfrac{\partial g_8}{\partial T_4^n}
\end{bmatrix}.
\tag{4.80}
$$

Since the global system for the electro-thermal problem is constructed following the assembly procedure described in Section 4.1.2, the Jacobian matrix is the nucleus matrix to be computed for each element of the mesh. The matrix entries for the electrical equation (4.78) are given, in general, by

$$
\frac{\partial f_p}{\partial \varphi_i^n} = \gamma_E(\bar{T}) K_{ip},
\tag{4.81}
$$

$$
\frac{\partial f_p}{\partial T_i^n} = -\frac{\partial \gamma_E(\bar{T})}{\partial T_i} \sum_{k=1}^{4} \varphi_k^n K_{kp} = \frac{1}{4} \frac{\gamma_{E0}[\alpha_E + 2\beta_E(\bar{T} - T_0)]}{[1 + \alpha_E(\bar{T} - T_0) + \beta_E(\bar{T} - T_0)^2]^2} \sum_{k=1}^{4} \varphi_k^n K_{kp},
\tag{4.82}
$$

and the entries for the thermal equation (4.79) are computed by

$$
\frac{\partial g_{p+4}}{\partial \varphi_i^n} = -2\Delta t_n \gamma_E(\bar{T}) \sum_{q=1}^{4} \varphi_q^n \Theta_{iqp},
\tag{4.83}
$$

$$
\frac{\partial g_{p+4}}{\partial T_i^n} = \rho_m c_p M_{ip} + \Delta t_n \gamma_T(\bar{T}) K_{ip} - \frac{1}{4} \Delta t_n \frac{\gamma_{T0}[\alpha_T + 2\beta_T(\bar{T} - T_0)]}{[1 + \alpha_T(\bar{T} - T_0) + \beta_T(\bar{T} - T_0)^2]^2} \sum_{k=1}^{4} T_k^n K_{kp}
$$

$$
+ \frac{1}{4} \Delta t_n \frac{\gamma_{E0}[\alpha_E + 2\beta_E(\bar{T} - T_0)]}{[1 + \alpha_E(\bar{T} - T_0) + \beta_E(\bar{T} - T_0)^2]^2} \sum_{k=1}^{4} \sum_{l=1}^{4} \varphi_k \varphi_l \Theta_{klp}, \qquad i, p = 1, \ldots, 4.
\tag{4.84}
$$

The right-hand side of the linear system (4.73) is assembled by the residuals

$$
R_p = \gamma_E(\bar{T}) \sum_{i=1}^{4} \varphi_i^{n-1} K_{ip},
\tag{4.85}
$$

$$
R_{p+4} = -\rho_m c_p \sum_{i=1}^{4} T_i^{n-1} M_{ip} + \rho_m c_p \sum_{i=1}^{4} T_i^{n-2} M_{ip} - \Delta t_n \gamma_T(\bar{T}) \sum_{i=1}^{4} T_i^{n-1} K_{ip}
$$

$$
+ \Delta t_n \gamma_E(\bar{T}) \sum_{i=1}^{4} \sum_{q=1}^{4} \varphi_i^{n-1} \varphi_q^{n-1} \Theta_{iqp}, \qquad p = 1, \ldots, 4.
\tag{4.86}
$$

4.3.3 Assembly of the Vacancy Dynamics Problem

The vacancy dynamics problem requires the solution of

$$
f_p = \sum_{k=1}^{4} C_{v,k}^n M_{kp} - \sum_{k=1}^{4} C_{v,k}^{n-1} M_{kp} + \Delta t_n D_v \left[\sum_{k=1}^{4} C_{v,k}^n K_{kp} + \frac{|Z^*|e}{k\bar{T}} \sum_{i=1}^{4} \sum_{k=1}^{4} \varphi_i^n C_{v,k}^n \Theta_{ipk} \right.
$$

$$
\left. - \frac{Q^*}{k\bar{T}^2} \sum_{j=1}^{4} \sum_{k=1}^{4} T_j^n C_{v,k}^n \Theta_{jpk} + \frac{f\Omega}{k\bar{T}} \sum_{l=1}^{4} \sum_{k=1}^{4} \sigma_l^n C_{v,k}^n \Theta_{lpk} \right] \tag{4.87}
$$

$$
+ \frac{\Delta t_n}{\tau} \left(q \sum_{m=1}^{4} C_{im,m}^n M_{mp} - C_{veq} V_p \right) = 0,
$$

and

$$
g_{p+4} = \sum_{m=1}^{4} C_{im,m}^n M_{mp} - \sum_{m=1}^{4} C_{im,m}^{n-1} M_{mp} + q\frac{\Delta t_n}{\tau} \sum_{m=1}^{4} C_{im,m}^n M_{mp} - \frac{\Delta t_n}{\tau} C_{veq} V_p = 0, \tag{4.88}
$$

for $p = 1, ..., 4$.

Applying Newton's method the Jacobian matrix has the form

$$
\mathbf{J_N} = \begin{bmatrix} \dfrac{\partial f_1}{\partial C_{v,1}^n} & \cdots & \dfrac{\partial f_1}{\partial C_{v,4}^n} & \dfrac{\partial f_1}{\partial C_{im,1}^n} & \cdots & \dfrac{\partial f_1}{\partial C_{im,4}^n} \\ \vdots & & \vdots & \vdots & & \vdots \\ \dfrac{\partial f_4}{\partial C_{v,1}^n} & \cdots & \dfrac{\partial f_4}{\partial C_{v,4}^n} & \dfrac{\partial f_4}{\partial C_{im,1}^n} & \cdots & \dfrac{\partial f_4}{\partial C_{im,4}^n} \\ \dfrac{\partial g_5}{\partial C_{v,1}^n} & \cdots & \dfrac{\partial g_5}{\partial C_{v,4}^n} & \dfrac{\partial g_5}{\partial C_{im,1}^n} & \cdots & \dfrac{\partial g_5}{\partial C_{im,4}^n} \\ \vdots & & \vdots & \vdots & & \vdots \\ \dfrac{\partial g_8}{\partial C_{v,1}^n} & \cdots & \dfrac{\partial g_8}{\partial C_{v,4}^n} & \dfrac{\partial g_8}{\partial C_{im,1}^n} & \cdots & \dfrac{\partial g_8}{\partial C_{im,4}^n} \end{bmatrix}, \tag{4.89}
$$

where the entries are computed by

$$
\frac{\partial f_p}{\partial C_{v,i}^n} = M_{ip} + \Delta t_n D_v \left[K_{ip} + \frac{|Z^*|e}{k\bar{T}} \sum_{j=1}^{4} \varphi_j^n \Theta_{jpi} \right.
$$

$$
\left. - \frac{Q^*}{k\bar{T}^2} \sum_{j=1}^{4} T_j \Theta_{jpi} + \frac{f\Omega}{k\bar{T}} \sum_{j=1}^{4} \sigma_j^n \Theta_{jpi} \right], \tag{4.90}
$$

$$
\frac{\partial f_p}{\partial C_{im,i}^n} = q\frac{\Delta t_n}{\tau} M_{ip}, \tag{4.91}
$$

and

$$
\frac{\partial g_{p+4}}{\partial C_{v,i}^n} = 0 \tag{4.92}
$$

$$
\frac{\partial g_{p+4}}{\partial C_{im,i}^n} = \left(1 + q\frac{\Delta t_n}{\tau} \right) M_{ip}, \qquad i, p = 1, \ldots, 4. \tag{4.93}
$$

The corresponding residuals are given by

$$
\begin{aligned}
R_p = & -\sum_{k=1}^{4} C_{v,k}^{n-1} M_{kp} + \sum_{k=1}^{4} C_{v,k}^{n-2} M_{kp} - \Delta t_n D_v \left[\sum_{k=1}^{4} C_{v,k}^{n-1} K_{kp} \right. \\
& + \frac{|Z^*|e}{k\overline{T}} \sum_{i=1}^{4}\sum_{k=1}^{4} \varphi_i^n C_{v,k}^{n-1} \Theta_{ipk} - \frac{Q^*}{k\overline{T}^2} \sum_{j=1}^{4}\sum_{k=1}^{4} T_j^n C_{v,k}^{n-1} \Theta_{jpk} \\
& \left. + \frac{f\Omega}{k\overline{T}} \sum_{l=1}^{4}\sum_{k=1}^{4} \sigma_l^{n-1} C_{v,k}^{n-1} \Theta_{lpk} \right] + \chi \frac{\Delta t_n}{\tau} \left(q \sum_{m=1}^{4} C_{im,m}^{n} M_{mp} - C_{veq} V_p \right),
\end{aligned}
\tag{4.94}
$$

$$
R_{p+4} = -\sum_{m=1}^{4} C_{im,m}^{n-1} M_{mp} + \sum_{m=1}^{4} C_{im,m}^{n-2} M_{mp} - q\frac{\Delta t_n}{\tau} \sum_{m=1}^{4} C_{im,m}^{n-1} M_{mp} + \frac{\Delta t_n}{\tau} C_{veq} V_p, \tag{4.95}
$$

$p = 1, \dots, 4.$

4.3.4 Calculation of the Mechanical Stress

The discretization of the mechanical problem presented in Section 4.2.4 yields the linear system of equations

$$
\mathbf{Kd} = \mathbf{f_{in}}, \tag{4.96}
$$

with

$$
\mathbf{K} = \int_T \mathbf{B}^T \mathbf{C} \mathbf{B} \, d\Omega, \tag{4.97}
$$

$$
\mathbf{f_{in}} = \int_T \mathbf{B}^T \mathbf{C} \varepsilon_0 \, d\Omega, \tag{4.98}
$$

Since $\mathbf{B}$, $\mathbf{C}$, and ε_0 are constant within an element, the assembly of (4.96) is performed in FEDOS using

$$
\mathbf{K} = \mathbf{B}^T \mathbf{C} \mathbf{B}, \tag{4.99}
$$

and

$$
\mathbf{f_{in}} = \mathbf{B}^T \mathbf{C} \varepsilon_0. \tag{4.100}
$$

The mechanical problem has to be solved each time step after the solution of the vacancy dynamics problem, as shown in Figure 4.3. Thus, for the time step n, the internal force vector is determined by the electromigration induced strain given in (3.82), so that

$$
\varepsilon_0 = \frac{1}{3} \varepsilon^{v,n} \mathbf{I}. \tag{4.101}
$$

From (3.78), the trace of the electromigration strain for each node of the tetrahedron is calculated by

$$
\varepsilon_i^{v,n} = \varepsilon_i^{v,n-1} - \Omega(1-f)\left(C_{v,i}^{n} - C_{v,i}^{n-1} \right) + \Omega\left(C_{im,i}^{n} - C_{im,i}^{n-1} \right), \qquad i = 1, \dots, 4, \tag{4.102}
$$

resulting in the element strain which is set in (4.101),

$$
\varepsilon^{v,n} = \sum_{i=1}^{4} \varepsilon_i^{v,n}. \tag{4.103}
$$

The solution of (4.96) yields the interconnect line deformation due to electromigration. Once the displacement field $\mathbf{d}$ is determined, the electromigration induced stress vector for an element is obtained using (4.60),

$$\boldsymbol{\sigma} = \mathbf{CBd} - \mathbf{C}\boldsymbol{\varepsilon}_0. \tag{4.104}$$

The mechanical stress at each node is obtained by an extrapolation from the stress calculated for the elements, given by (4.104). The stress at a particular node is calculated by performing a weighted average of the stress on all elements connected to the node. Considering a node $p \in T_h(\Omega)$ and defining the set of all elements which contain the node as $T(p)$, the mechanical stress at the node p is given by

$$\boldsymbol{\sigma}_p = \frac{1}{\sum\limits_{T \in T(p)} V_T} \sum\limits_{T \in T(p)} V_T \boldsymbol{\sigma}_T, \tag{4.105}$$

where V_T is the volume, and $\boldsymbol{\sigma}_T$ is the stress calculated by (4.104) for the element T.

4.3.5 Mesh Refinement at Material Interfaces and Grain Boundaries

In order to obtain an appropriate resolution for the local vacancy dynamics at grain boundaries and interfaces formed by the interconnect metal with the surrounding layers, an appropriately fine FEM mesh has to be provided at these locations. Therefore, a simple local mesh refinement procedure was implemented. The procedure first detects the elements with nodes connected to more than one segment. If the tetrahedron volume is larger than a given value, the corresponding tetrahedron is refined. This procedure can be executed recursively, until all tetrahedrons connected to the interface have a volume smaller than the specified one. Figure 4.4 shows the mesh refinement obtained at a grain boundary and at the metal/capping layer interface of a typical dual-damascene interconnect.
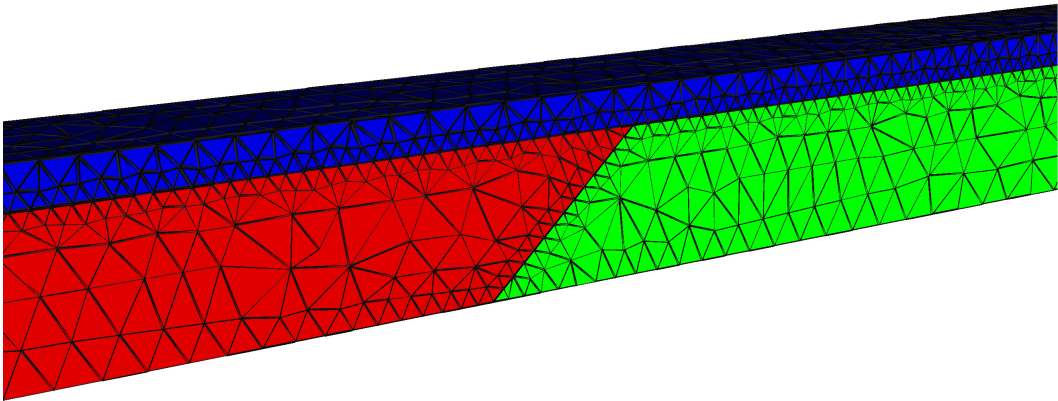

Figure 4.4: Mesh refinement at a grain boundary and at a material interface.

Chapter 5

Simulation Studies of Electromigration

In this chapter several electromigration simulation examples according to the model discussed in Chapter 3 are presented. First, the materials considered in the simulations are introduced and the corresponding set of parameters used by the models are defined. Then, the model calibration and verification by comparing it to the models described in Chapter 2 is presented. The vacancy dynamics behavior is analyzed, neglecting first the mechanical stress, which is incorporated later to clearly show the importance of the stress effect on the electromigration failure development. Also, the influence of the mechanical stress in producing anisotropic diffusivity and its effect on material transport in a dual-damascene interconnect structure is studied. Then, the importance of introducing the fast diffusivity paths into the modeling framework is shown. This enables to explain several features of failure development commonly observed in experiments, for which the simple effective diffusion models cannot cope with. Finally, the role of the copper grain distribution on electromigration lifetimes of bamboo-like interconnect lines is investigated.

5.1   Material and Simulation Parameters

The following simulations are focused on contemporary copper dual-damascene interconnect structures of the 65 nm and 45 nm technology nodes. The typical materials used in such interconnects are: copper (Cu) as conductor metal, tantalum based (TaN/Ta) barrier layers at the bottom and sides of the lines, silicon nitride based (SiN/SiCN) capping layers, and low-k interlevel dielectrics, such as SiCOH.

The tables below present the materials' parameters for the electro-thermal, vacancy dynamics and mechanical deformation problem. These parameters were chosen from the recent literature, where they were obtained either by experimental or theoretical studies. Since electromigration just takes place in the conductor line, the parameters related to the material transport equations are presented for copper only.

Electromigration experiments are carried out under accelerated test conditions, which means that the interconnect lines are normally tested at a higher current density and at

a higher temperature than that found at use conditions. Therefore, the simulation results presented in the following sections follow this trend, and were obtained for a current density of 2 MA/cm² and temperature of 300 °C, unless otherwise stated.

Table 5.1: Parameters of the electro-thermal equations.

Parameter	Cu	Ta	SiN	SiCOH	Reference
γ_{E0} (Ωm)	4.0×10^7	3.3×10^5	-	-	[81]
α_E (K^{-1})	0.0043	0	0	0	[157]
β_E (K^{-2})	0	0	0	0	-
γ_{T0} (W/mK)	379	53.65	0.8	0.35	[158, 12]
α_T (K^{-1})	0	0	0	0	-
β_T (K^{-2})	0	0	0	0	-
ρ_m (kg/m^3)	8920	16690	3100	2200	[158, 12]
c_p (J/kgK)	385	140.15	170	1000	[158, 12]

Table 5.2: Parameters of the mechanical equations.

Parameter	Cu	Ta	SiN	SiCOH	Reference
E (GPa)	130	186	265	9.2	[97, 12]
ν	0.34	0.35	0.27	0.16	[158]
α (K^{-1})	16.5×10^{-6}	6.50×10^{-6}	1.50×10^{-6}	0.68×10^{-6}	[158]

Table 5.3: Parameters of the vacancy dynamics equations.

Parameter	Cu	Reference
D_{v0} (cm^2/s)	0.52	[97]
E_a (eV)	0.89	[159]
Z^*	-5.0	[67]
Q^* (J)	1.2×10^{-20}	-
f	0.4	-
Ω (cm^3)	1.18×10^{-23}	-
C_{v0} (cm^{-3})	1.0×10^{16}	-
τ (s)	1.0	[97]

Table 5.4: Simulation conditions.

Parameter	Value
j (MA/cm^2)	2.0
T (°C)	300

5.2 Model Calibration and Verification

In this section, the developed electromigration model is calibrated and verified by comparing simulation results with analytical solutions which are available for the simple models presented in Chapter 2.

5.2.1 Vacancy Dynamics

Consider the simple model of Shatzkes and Lloyd, expressed by the equation (2.13). Given a finite line of length L, with blocking boundary conditions at both ends of the line, that is

$$J_v(0,t) = J_v(-L,t) = 0, \tag{5.1}$$

the solution of (2.13) under such boundary conditions is of the form [160]

$$\frac{C_v(x,t)}{C_{v0}} = A_0 - \sum_{n=1}^{\infty} A_n \exp\left(-B_n \frac{D_v}{L^2}t + \frac{\alpha}{2}\frac{x}{L}\right), \tag{5.2}$$

where

$$\alpha = \frac{|Z^*|e\rho j L}{kT}. \tag{5.3}$$

The steady-state solution is determined by the term

$$A_0 = \frac{\alpha}{1 - \exp(-\alpha)}\exp\left(\alpha\frac{x}{L}\right), \tag{5.4}$$

and the coefficients A_n and B_n are given, respectively, by

$$A_n = \frac{16n\pi\alpha^2[1 - (-1)^n\exp(\alpha/2)]}{(\alpha^2 + 4n^2\pi^2)^2}\left[\sin\left(n\pi\frac{x}{L}\right) + \frac{2n\pi}{\alpha}\cos\left(n\pi\frac{x}{L}\right)\right], \tag{5.5}$$

$$B_n = n^2\pi^2 + \alpha^2/4. \tag{5.6}$$

In order to compare the numerical implementation with this analytical solution, it is set $G = 0$ in (3.75) and $f = 0$ in (3.74). This makes the proposed model equivalent to equation (2.13) by removing the generation/recombination term and also neglecting the mechanical stress effects. Figure 5.1 shows the vacancy distribution next to the blocking boundary at $x = 0$ of a simple copper line of length $L = 50$ μm after a time $t = 1$ h, obtained from a numerical simulation.

The current flows from left to right, so that vacancy accumulates at the cathode end of the line. At the same time, vacancy depletion takes place at the anode side at $x = -L$. This can be seen by the vacancy concentration at the center of the line along the x direction, as shown in Figure 5.2 for different time periods. The curve for $t = 3600$ s shows the vacancy concentration distribution after the steady state is already reached. The symbols correspond to the numerical simulation results, while the solid lines correspond to the analytical solution given in (5.2). It should be pointed out that the agreement between the numerical and the analytical solution is excellent.
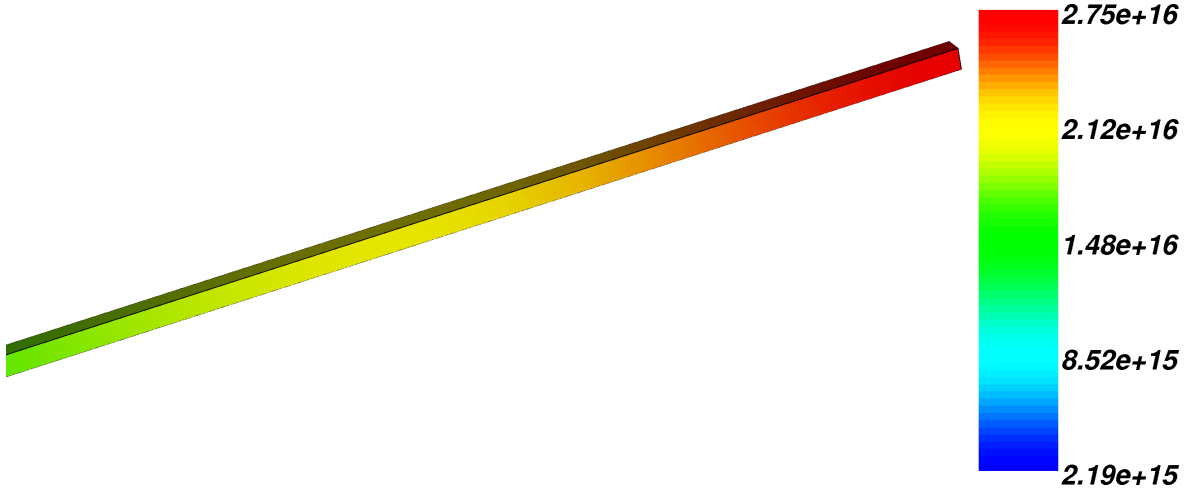
Figure 5.1: Detail of the vacancy distribution next to the cathode end of the line after $t = 3600\,\mathrm{s}$ (in cm^{-3}).
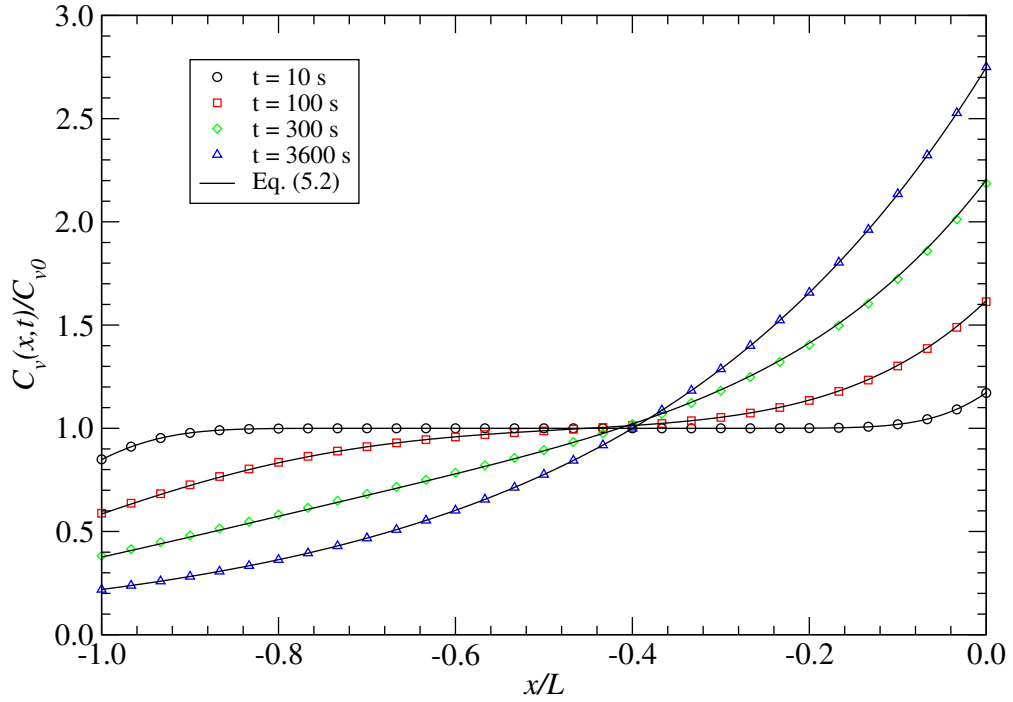

Figure 5.2: Vacancy concentration along the line at different times for $j = 2.0\ \mathrm{MA/cm^2}$. The symbols are the numerical simulation results and the solid lines are obtained by (5.2).

The accumulation of vacancies at the cathode and depletion at the anode creates a gradient of vacancy concentration along the line, which counters the electromigration flux. Once the vacancy gradient produces a back flux that equals the electromigration flux, the steady state condition is reached. The vacancy build-up with time at the boundary $x = 0$ is shown in Figure 5.3. The simulation results are presented for three values of current density, $j = 1.0$, 2.0, and 5.0 MA/cm^2. The increase of current density is accompanied by the increase of the electromigration flux, which leads to a higher vacancy concentration at the cathode end of the line. It is interesting to note that the time to reach the steady state lies in the order of minutes. After about 10 min the vacancy concentration already saturates. As it will be shown later, this is a major shortcoming of this model. Figure 5.3 shows that an excellent agreement between the numerical and the analytical solution is again observed.

Consider now the intersection of two metal grains forming a grain boundary, as shown in Figure 5.4. The model of Rosenberg and Ohring, given by equation (2.21), is used to analyze the vacancy supersaturation that can develop at such a grain boundary. The magnitude of vacancy supersaturation at the grain boundary is a function of the transport characteristics of both grains. Thus, depending on the difference of the diffusion coefficients in each grain, or on the available paths for atomic transport, different supersaturation values are expected.
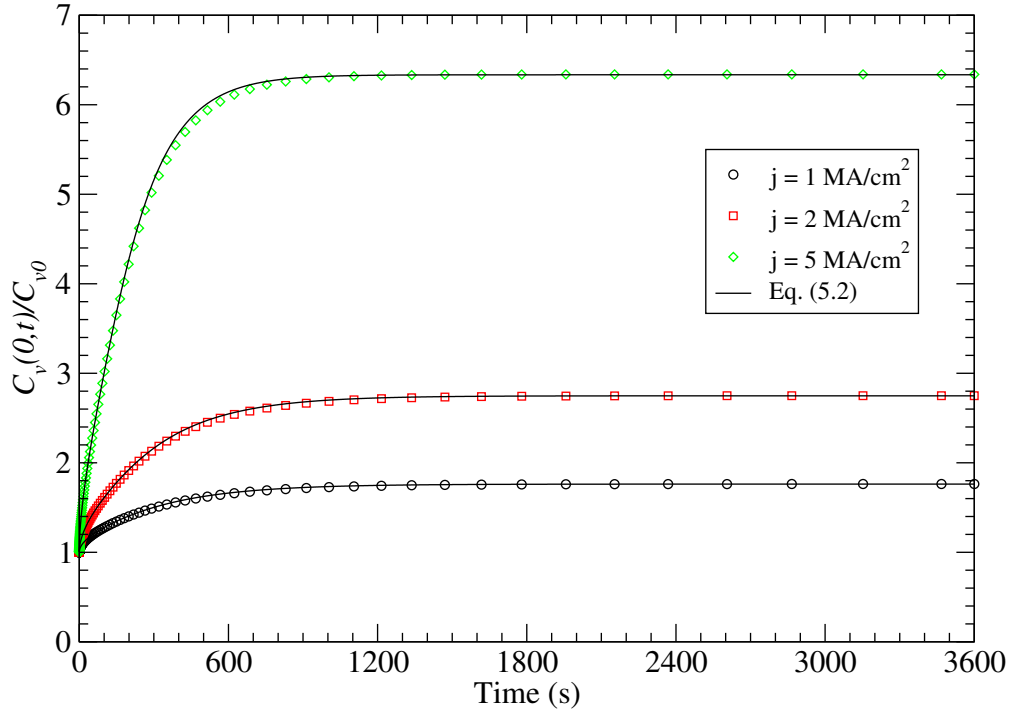

Figure 5.3: Vacancy concentration development at $x = 0$ for different magnitudes of current density. The symbols are the numerical simulation results and the solid lines are obtained by (5.2).
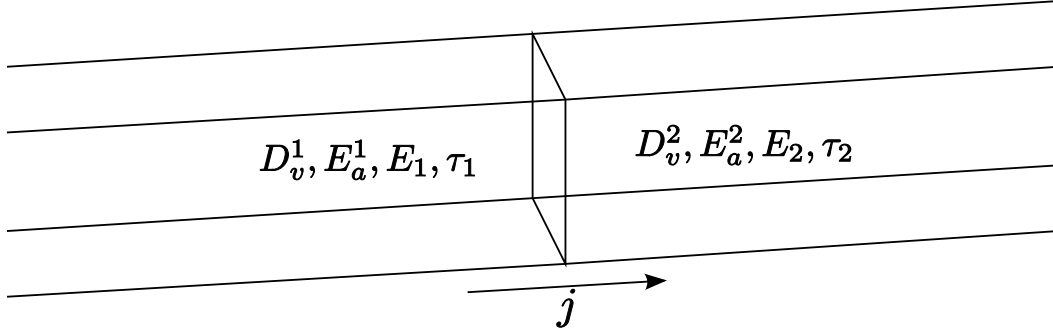
Figure 5.4: The intersection of two copper grains with different properties forming a grain boundary.

At steady state ($\partial C_v/\partial t = 0$) both, the vacancy concentration and the flux are continuous along the grain boundary interface,

$$C_v^1(x = 0) = C_v^2(x = 0) \quad \text{and} \quad J_v{}^1(x = 0) = J_v{}^2(x = 0), \tag{5.7}$$

so that the solution of (2.21) yields for each grain [72]

$$
\begin{aligned}
S_1(x) &= \frac{C_v^1(x)}{C_{v0}} - 1 = S(0)\exp(-\lambda_1 x), \quad x < 0, \\
S_2(x) &= \frac{C_v^2(x)}{C_{v0}} - 1 = S(0)\exp(-\lambda_2 x), \quad x > 0,
\end{aligned}
\tag{5.8}
$$

where $S(0)$ is the vacancy supersaturation at $x = 0$, given by

$$S(0) = \left[\left(\frac{\lambda_1 D_v^1 - \lambda_2 D_v^2}{D_v^2 E_2 - D_v^1 E_1} \right) \frac{kT}{|Z^*|e} - 1 \right]^{-1}, \tag{5.9}$$

and

$$
\begin{aligned}
\lambda_1 &= -\frac{|Z^*|eE_1}{2kT} - \left[\left(\frac{|Z^*|eE_1}{2kT} \right)^2 + \frac{1}{D_v^1 \tau_1} \right]^{1/2}, \\
\lambda_2 &= -\frac{|Z^*|eE_2}{2kT} + \left[\left(\frac{|Z^*|eE_2}{2kT} \right)^2 + \frac{1}{D_v^2 \tau_2} \right]^{1/2}.
\end{aligned}
\tag{5.10}
$$

It is assumed that the diffusion coefficient in each grain is different, so that $E_a^1 = 0.89$ eV is set for the left grain, and $E_a^2 = 1.1$ eV is set for the right grain of the line. The other paremeters are considered to be the same for both grains. The electric current flows from the left to the right grain, and since the activation energy for diffusion is smaller in the first grain, vacancies arrive at the grain boundary at a higher rate than they leave. As a result, vacancy accumulation takes place at the grain boundary, as shown in Figure 5.5.
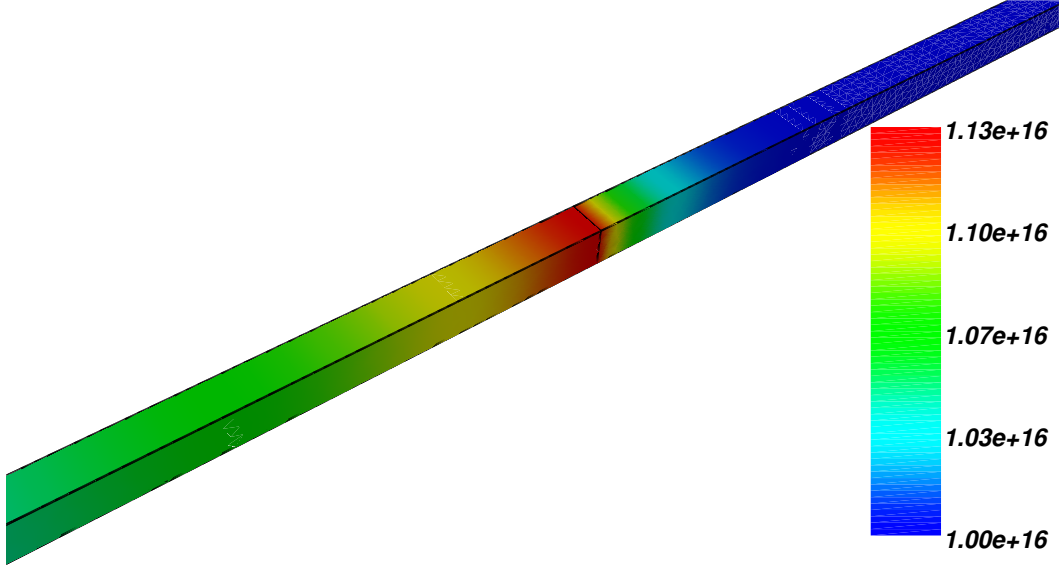
Figure 5.5: Detail of the vacancy concentration at the grain boundary formed by the intersection of two grains with different diffusion coefficients (in cm^{-3}).

The vacancy supersaturation along the grains for different vacancy relaxation times is shown in Figure 5.6. One can see that the vacancy concentration profile in each grain is quite different. The bigger diffusion coefficient leads to a smaller concentration gradient in the left grain. In turn, the smaller diffusivity in the right grain leads to a larger concentration gradient near the grain boundary. The comparison between the numerical simulations and the analytical solution, given by equation (5.8), is remarkably good.

An important observation is that the supersaturation significantly decreases as the vacancy relaxation time decreases. Furthermore, the maximum supersaturation is rather small, even for longer vacancy relaxation times. This means that the maximum supersaturation is significantly dependent on τ, that is, it is significantly dependent on the effectiveness of the vacancy sink/source. As a consequence, a high vacancy supersaturation cannot be obtained near vacancy sinks, since vacancies are annihilated as soon as the local vacancy concentration becomes higher than its equilibrium value.

The time development of the vacancy supersaturation at the grain boundary obtained from the numerical simulations is presented in Figure 5.7. Besides the aforementioned strong influence on the supersaturation magnitude, the vacancy relaxation time has a significant impact on the time to reach the steady state condition. Here again, the shorter the relaxation time is, the faster vacancy annihilation or generation processes occur, and the faster the system tends to the equilibrium condition. Moreover, the steady state is reached in a time range which lies in the order of seconds. Even for much larger vacancy relaxation times the time to reach the steady state is, at most, in the order of minutes.
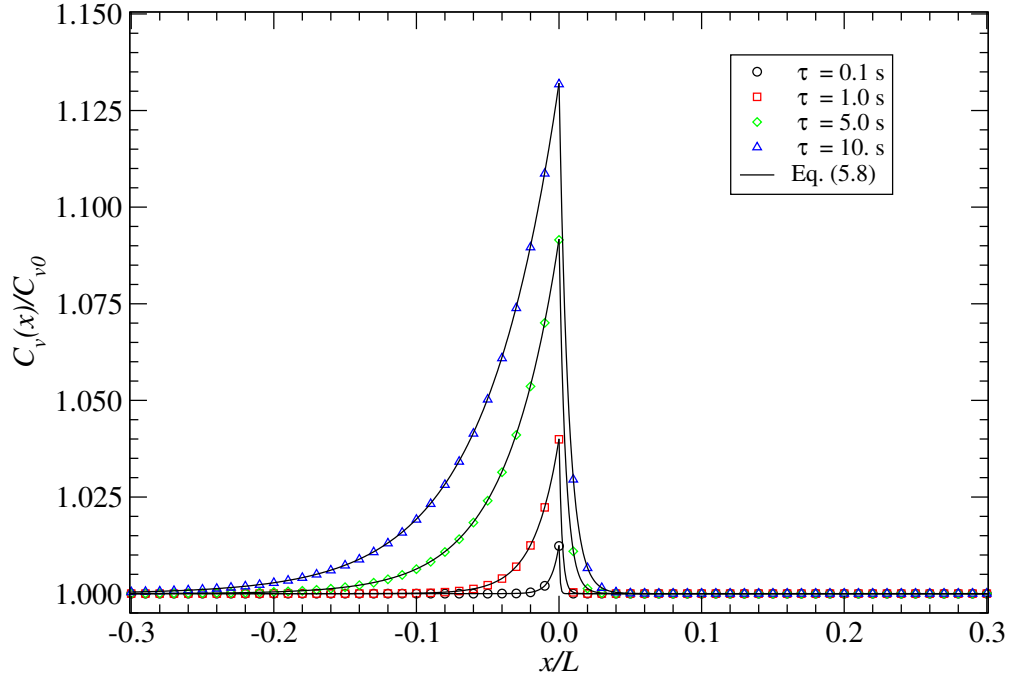
Figure 5.6: Vacancy concentration at the grain boundary for different vacancy relaxation times. The symbols are the numerical simulation results and the solid lines are obtained by (5.8).
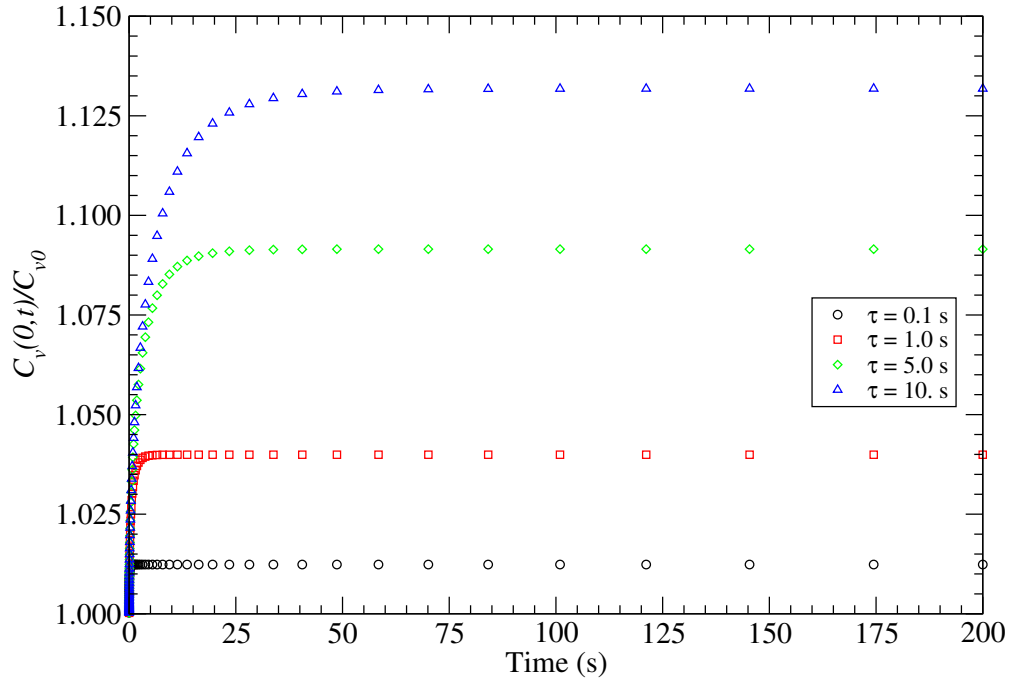

Figure 5.7: Vacancy concentration at the grain boundary as a function of time. The vacancy relaxation time, τ, is a key parameter in determining the magnitude of vacancy supersaturation and the time to reach the steady state.

73

These results show that the numerical simulations consistently recover the analytical solutions for the limiting cases studied above. At the same time, their most important features are presented. However, two critical issues appear here: first, the magnitudes of vacancy supersaturation are quite small, and second, the time to reach the steady state is too short. The first issue hinders a satisfying explanation for void nucleation observed during electromigration tests, while the latter is inconsistent with the typical time of electromigration failure development, which is in the order of several hours. As already pointed out, the introduction of the mechanical stress effect is crucial to resolve the above inconsistencies, as it is shown below.

5.2.2 The Role of Mechanical Stress

Consider a simple 50 μm Cu long line, where the mechanical deformation, and consequently mechanical stress, accompanying electromigration is determined by the solution of (3.78)–(3.82). Here, the effect of vacancy annihilation/production on the strain rate is determined by

$$G = -\frac{C_v - C_{veq}}{\tau}, \tag{5.11}$$

with C_{veq} given by (2.38). It is assumed that the line is encapsulated by a rigid passivation layer, in such a way that the displacement components of the line surfaces are set to zero as boundary condition. Applying the parameters given in Section 5.1, the hydrostatic stress distribution at the anode and cathode end of the line for a time $t = 100\,\mathrm{h}$ is depicted in Figure 5.8.
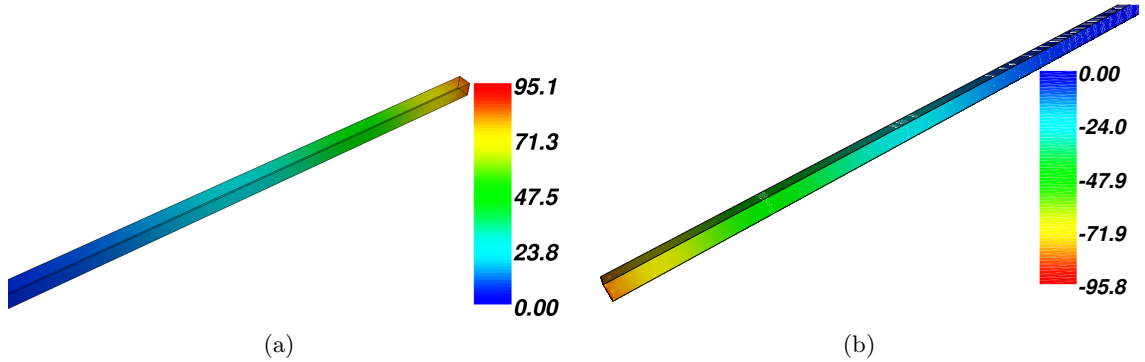

Figure 5.8: Hydrostatic stress distribution in a 50 μm long line at $t = 100\,\mathrm{h}$ (in MPa). (a) Tensile stress (positive) develops at the cathode end of the line. (b) At the anode end compressive stress (negative) develops.

At the anode end $(x = -L)$ there is a depletion of vacancies, or an excess of Cu atoms, which leads to a compressive stress (negative). In turn, accumulation of vacancies at the cathode $(x = 0)$ driven by electromigration results in a tensile stress (positive). The stress profile along the center of the line is shown in Figure 5.9. The magnitude of the stress at the ends of the line gradually increases with time, developing the stress gradient which counters electromigration. In steady state, the stress varies linearly along the line, and the electromigration flux is totally compensated by the back flux driven by the gradient of stress.
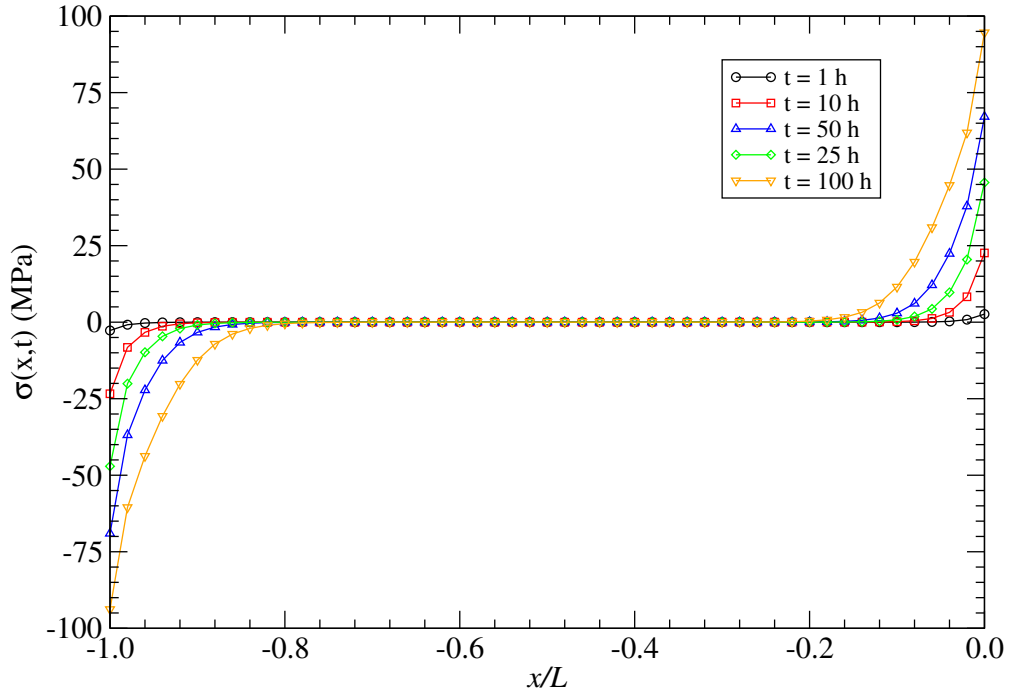
Figure 5.9: Stress profile along the line at different periods in time.
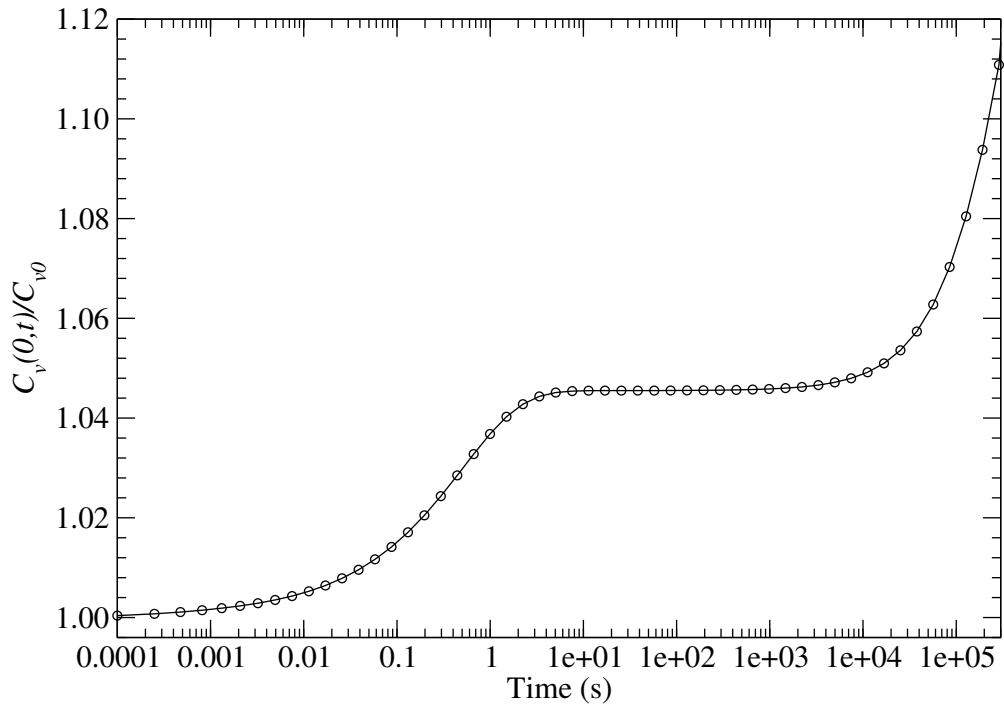

Figure 5.10: Vacancy concentration as a function of time at the cathode end of the line.

Figure 5.10 shows the development of the vacancy concentration at the cathode end with time. This curve can be divided into three regions. The first corresponds to the initial period of time, where a rapid increase in the vacancy concentration is observed. It is a quite short period and lasts about 1 s only. By this time the second period starts, where the vacancy concentration remains practically constant. This period lasts until about $t = 10^4$ s. Kirchheim [53] called this period a quasi steady state period. Finally, in the third period, the vacancy concentration increases at a low rate until the true steady state is reached. Typically, this is the longest period, lasting from hundreds until thousands of hours.

The initial stress build-up closely follows the first period of increase of the vacancy concentration. As the quasi steady state is reached, the stress grows approximately linearly with time, shown in Figure 5.11. It corresponds to a period of transition from lower to higher values of stress. At first, the low stress does not affect the equilibrium vacancy concentration. However, as the stress magnitude increases, the equilibrium vacancy concentration also increases, which, in turn, affects the stress build-up due to the generation/recombination term given in (5.11). As a consequence, the third period is characterized by a non-linear increase of the stress until the true steady state is reached, as can be seen in Figure 5.12. The correspondence between these periods of vacancy development with mechanical stress build-up was already observed by Kirchheim [53].
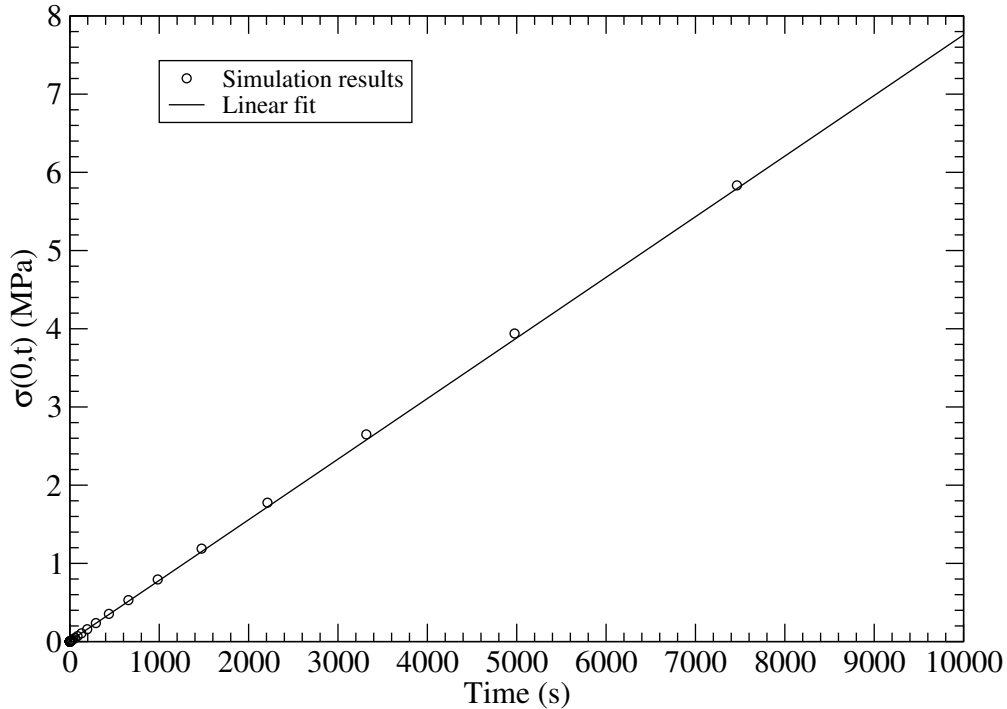

Figure 5.11: Stress evolution during the quasi steady state period. In this period the stress grows linearly with time.
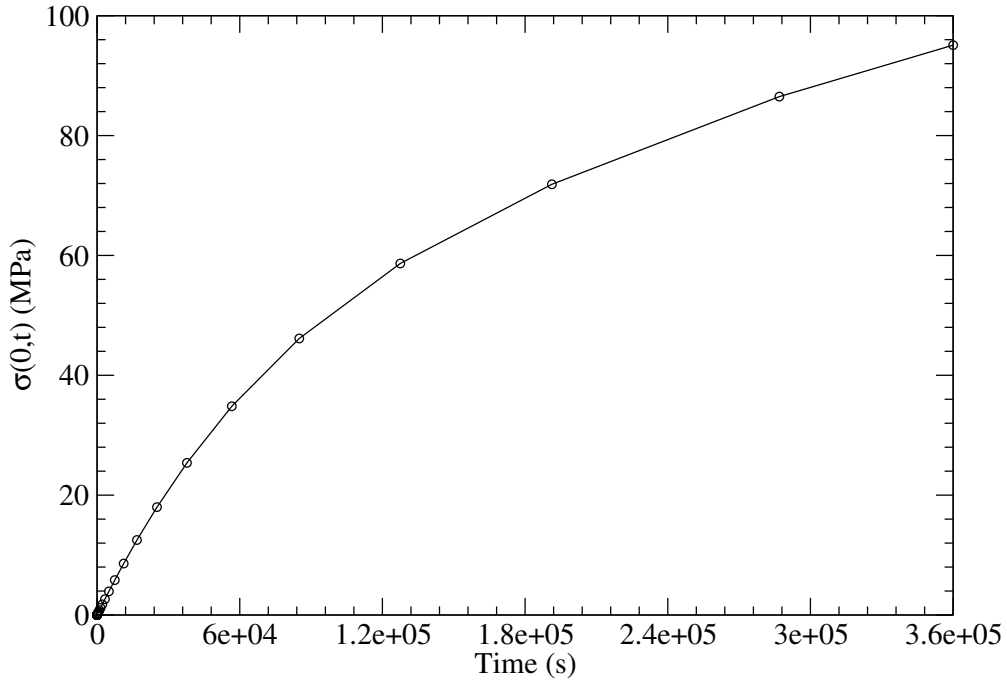
Figure 5.12: Stress build-up with time. A non-linear increase of stress is observed at longer times.

To sum up, high mechanical stresses can develop in a conductor line under electromigration. The stress build-up with time is a slow process, where high stresses develop after several hours, in contrast to the fast vacancy build-up observed in the results of Section 5.2.1. Moreover, the numerical simulation results reproduce the same characteristic behavior described by Kirchheim [53].

5.3 Stress Effect on Diffusivity

The effect of mechanical stress on the diffusivity and, consequently, on the material transport due to electromigration is analyzed. Consider the copper dual-damascene interconnect structure shown in Figure 5.13. The structure is initially at a temperature of 500 °C and then cools down to about 100 °C. Upon cooling from such a high temperature, mechanical stress develops in the copper line due to the large difference of the thermal expansion coefficients between the copper and the surrounding materials (Table 5.2). The three stress components, σ_{xx}, σ_{yy}, and σ_{zz} along the upper line, via, and lower line are shown in Figure 5.14. Here, the boundary at the bottom of the passivation is assumed to be fixed, simulating the mechanical constraint imposed by a thick substrate.
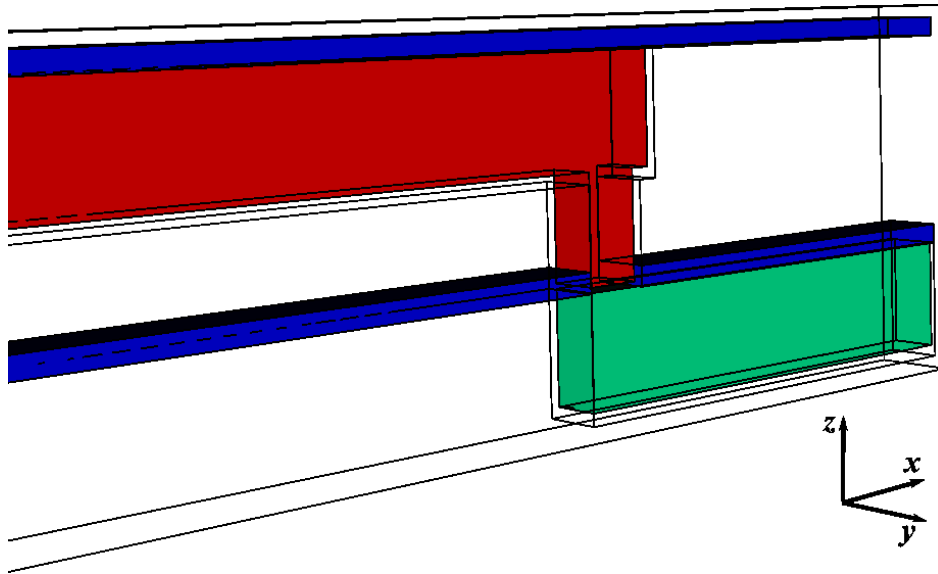
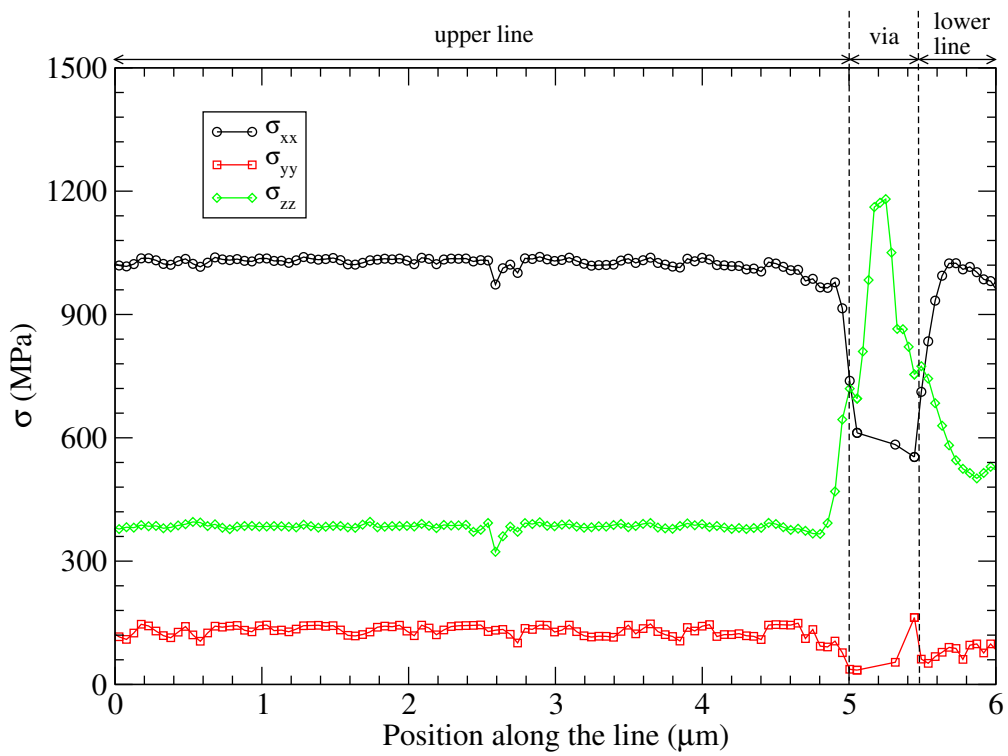**Figure 5.13:** Complete dual-damascene interconnect via.

Figure 5.14: Stress components along the upper line, via, and lower line.

One can see that the stress state in the line strip and in the via are rather different. In the line strip, the σ_{xx} component has a magnitude of about 1 GPa and is much larger than the other components, where σ_{zz} is about 360 MPa, and σ_{yy} about 120 MPa. The lower stress level for σ_{yy} is due to the small dimension of the line in this direction, so that the mechanical constraint imposed by the boundary condition at the bottom of the passivation is small [161]. In the via region σ_{xx} is reduced to 600 MPa, while the σ_{zz} component significantly increases, reaching 1.2 GPa. This behavior was already observed by Paik *et al.* [161] and Suzuki *et al.* [162]. A high value of σ_{zz} develops due to the small dimensions of the via in the x and y directions in combination with the constraints imposed in the z direction by the boundary condition at the bottom surface of the passivation, and by the barrier and capping layer, since both have larger elastic modulus than the copper.

Figure 5.15 shows the hydrostatic stress in the metal lines. The hydrostatic stress distribution has an important influence on the total material transport, as the gradient of hydrostatic
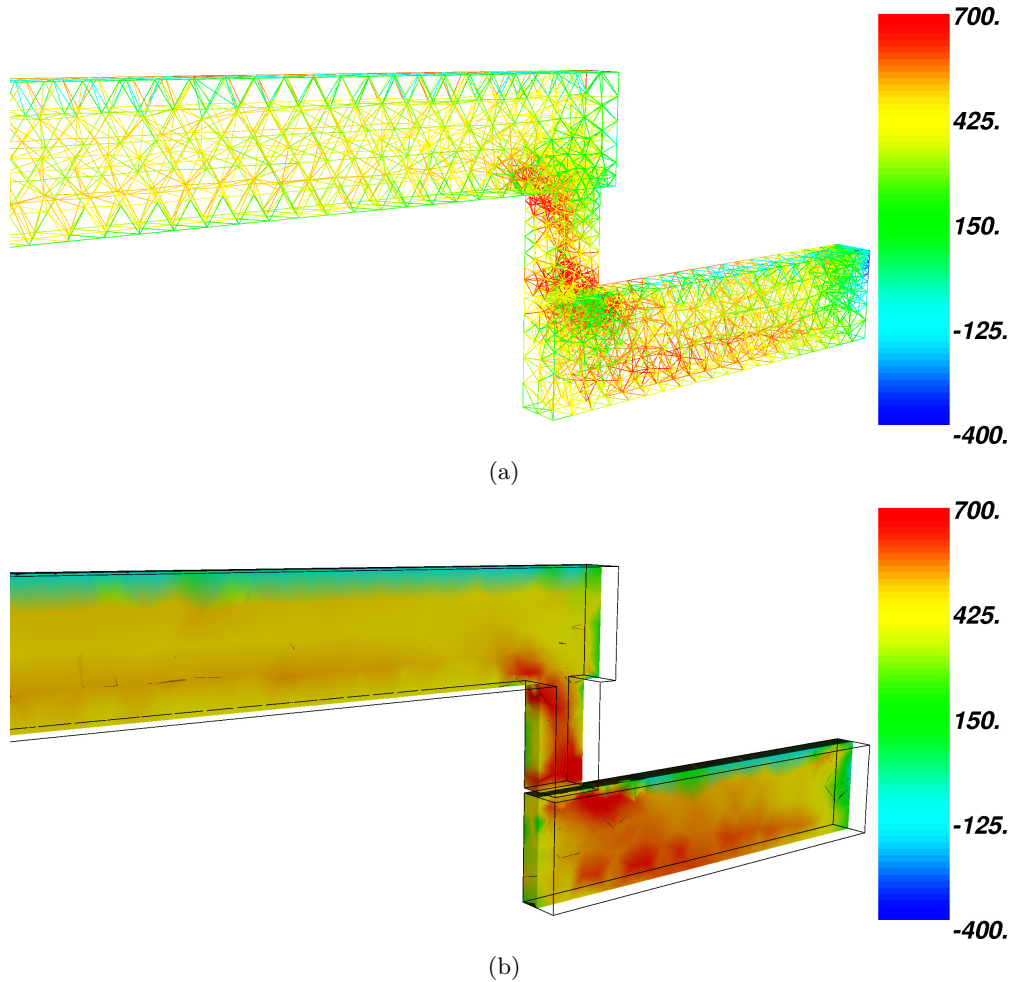

(a)

(b)

Figure 5.15: Hydrostatic stress distribution in an interconnect via after cooling from 500 °C to 100 °C (in MPa). (a) Distribution on the mesh nodes. (b) Profile in a cut through the structure.

stress is an additional driving force for atom migration. The hydrostatic stress is not uniform throughout the copper lines. High stresses develop at the bottom of the via in the top line and at the edge of the via intersecting with the capping layer in the bottom line.

The interconnect is now subjected to an electromigration test at 100 °C and 2 MA/cm^2, where the current flows from the upper to the lower line. The Ta barrier layer at the bottom of the via acts as a blocking boundary for diffusion, so that the electromigration flux leads to a build-up of vacancies at this site, as shown in Figure 5.16. An interesting observation is that the peak of the vacancy concentration is higher at the outer interfaces than in the bulk of the via. This is a consequence of the non-uniform hydrostatic stress distribution, as vacancies are driven by the high stress gradients present in the via region.
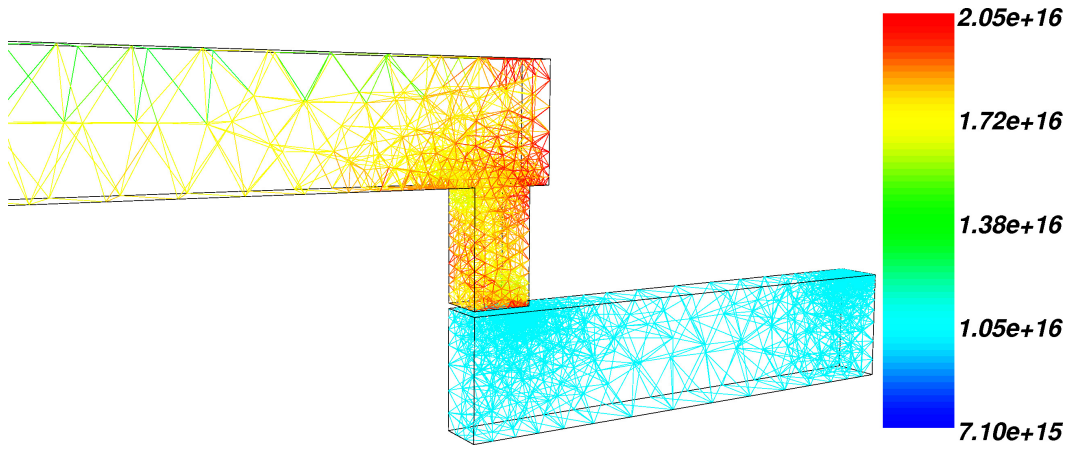

Figure 5.16: Vacancy distribution at the upper line. Vacancies concentrate at the bottom of the via, which is a blocking boundary for vacancy diffusion (in cm^{-3}).

In order to show the effect of the stress components (Figure 5.14) on the vacancy transport, three cases are considered. First, it is assumed that the vacancy diffusivity is a constant scalar quantity independent of stress, following the usual Arrhenius law (2.10), with pre-exponential factor and activation energy given in Table 5.3. Then, the diffusivity is treated as a scalar quantity which is affected by the hydrostatic stress according to equation (3.13). In the third case, the effect of the individual stress components is taken into account, yielding a tensorial diffusivity, as derived in Section 3.2.2. The vacancy build-up at the bottom of the via is shown in Figure 5.17. The simulations are carried out at a temperature commonly used in accelerated tests, 300 °C, and at a temperature close to that found at typical operating conditions, 100 °C.

One can see that, at the elevated temperature, the vacancy build-up is practically identical for all cases, that is, vacancy transport is not affected by the stress distribution. This means that the diffusivity dependence on stress is weak. Thus, the diffusivity can be considered to be isotropic and can be well described by a scalar quantity. On the other hand, at real operating conditions a clear distinction in vacancy evolution is observed. In this case, the tensile stress originated from the thermal process leads to an increased diffusivity, which, in turn leads to a higher vacancy flux along the conductor lines and a higher vacancy concentration at the via. Thus, the diffusivity dependence on stress becomes an important factor to be considered. The addition of the hydrostatic stress dependence on the scalar diffusivity represents already an

improvement in the diffusivity description. Nevertheless, the large difference in magnitudes of the individual components of the stress, as shown in Figure 5.14, certainly leads to an anisotropic diffusion process which can only be described by the tensorial diffusivity, as derived in Section 3.2.2.

The different behavior at the different temperatures is a consequence of the stress magnitude which develops in the structure after the thermal cycle. At an elevated temperature, the stresses which result from the cooling process are smaller, since the difference between the initial temperature and the test temperature is smaller. Therefore, the stress level produced at elevated temperature tests is unlikely to cause a significant variation of the diffusion coefficient. However, it is shown that a different behavior is expected as soon as the test temperature approaches the use condition, where the residual stresses from the fabrication process become large enough to influence the vacancy diffusivity.

These results have an important consequence for the extrapolation of lifetimes obtained from accelerated tests to use conditions. They indicate that the activation energy for the diffusion process obtained from accelerated tests is likely to be wrong, since the stress effect on diffusion has a different impact at the accelerated tests and at the use conditions. This situation can be partially improved by introducing a hydrostatic stress dependence on the diffusion coefficient. However, the anisotropic effect cannot be estimated, since a detailed picture of the stress components cannot be experimentally determined. Thus, the developed model provides a useful insight into this problem.
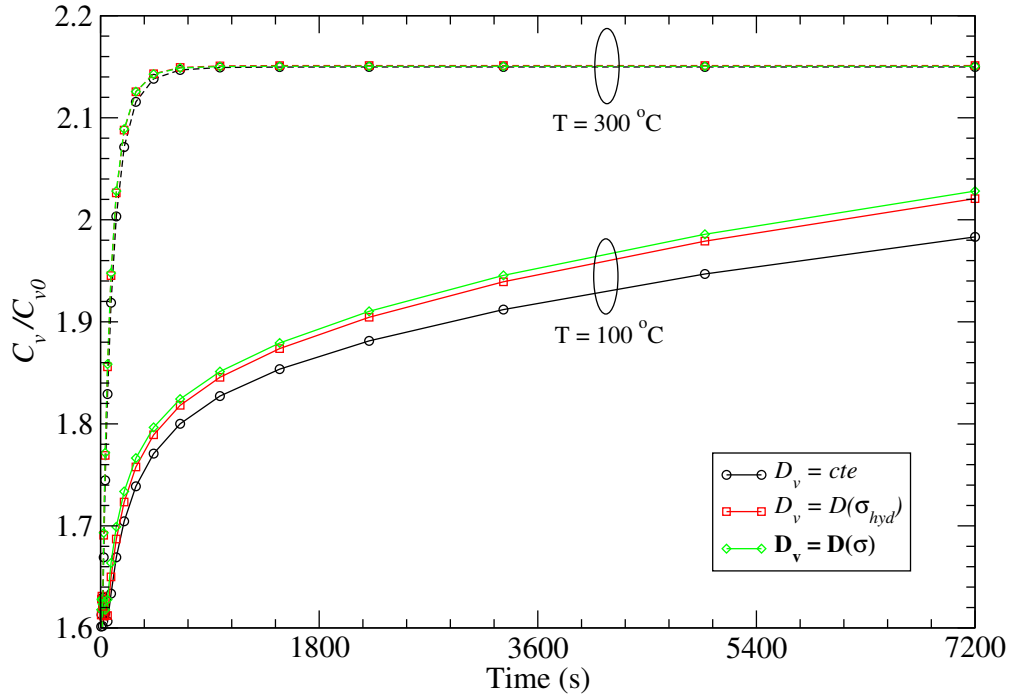

Figure 5.17: Vacancy evolution at the bottom of the via. Three cases are studied: constant diffusivity, hydrostatic stress dependent diffusivity, and stress tensor dependent diffusivity.

5.4   Fast Diffusivity Paths

Numerical simulations of electromigration are normally carried out on simple two-dimensional lines, in such a way that the effects of interfaces formed by the metal with the surrounding materials are frequently neglected. The most common example of such a case is the use of a single effective diffusion coefficient for the entire metal line, namely, for bulk, grain boundaries and interfaces.

Consider the interconnect via shown in Figure 5.18, where 0.01 V is applied at the left boundary of the upper line (M2) and 0.0 V at the right boundary of the lower line (M1). This yields a current density of 2 MA/cm^2 passing through the interconnect, and the electrons move from M1 to M2 (upstream electron flow). Figure 5.19 shows the current density in the line and via region. In this case, the electromigration development in the M2 line is studied.
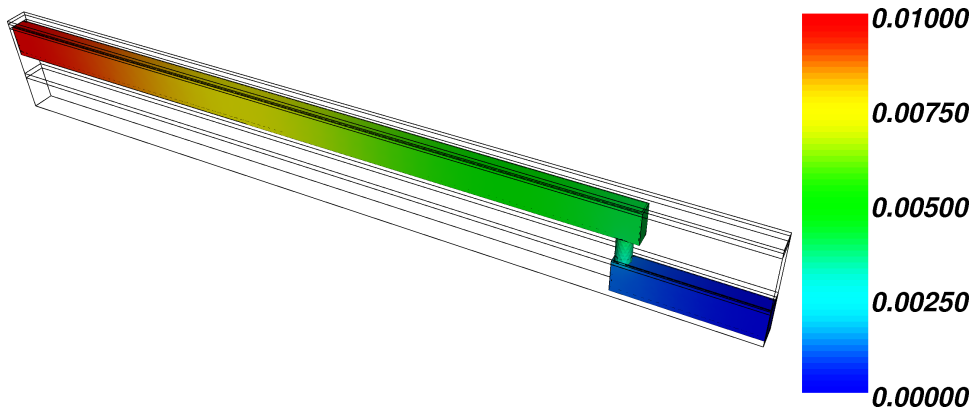
Figure 5.18: Electric potential along the interconnect line (in V).
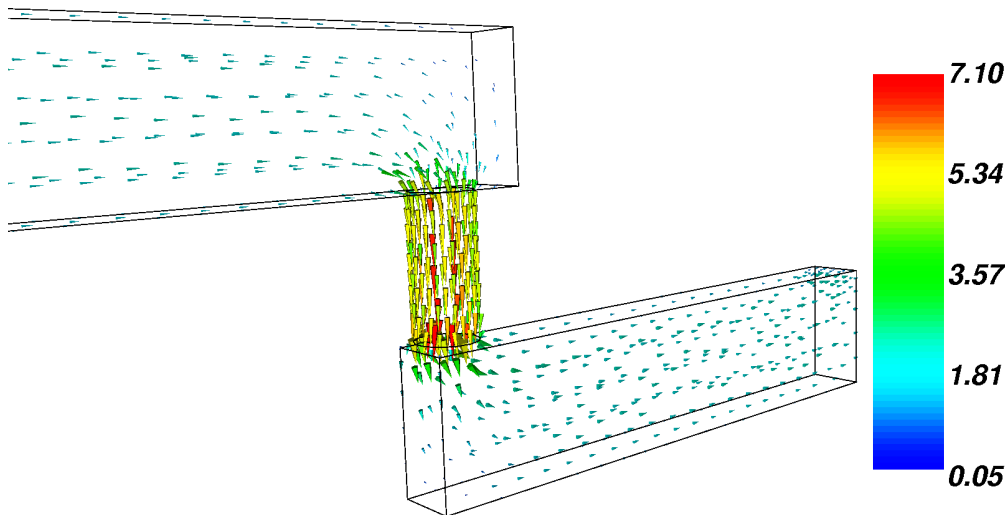
Figure 5.19: Current density distribution next to the via region (in MA/cm^2). The current density magnitude is larger in the via than in the line, since the cross section of the via is smaller than that of the line.

The current density is larger in the via than in the line, because the via has a smaller cross section than the line. This larger current density yields a higher joule heating in the via, which, in turn, leads to an increase of the temperature in this region, as shown in Figure 5.20. However, the external boundaries of the passivation are kept at the test temperature, 573 K, so that the temperature increase in the via is very small, and the entire interconnect practically remains at the same temperature. In fact, the temperature increase in the via is so small that it cannot significantly affect the vacancy transport.

Given the conditions above, vacancies are driven by electromigration from the left to the right end of the line. Since the bottom of the via is a blocking boundary, vacancies accumulate at this region, as shown in Figure 5.21. The increase in vacancy concentration at the via bottom is accompanied by the build-up of a tensile stress, shown in Figure 5.22.
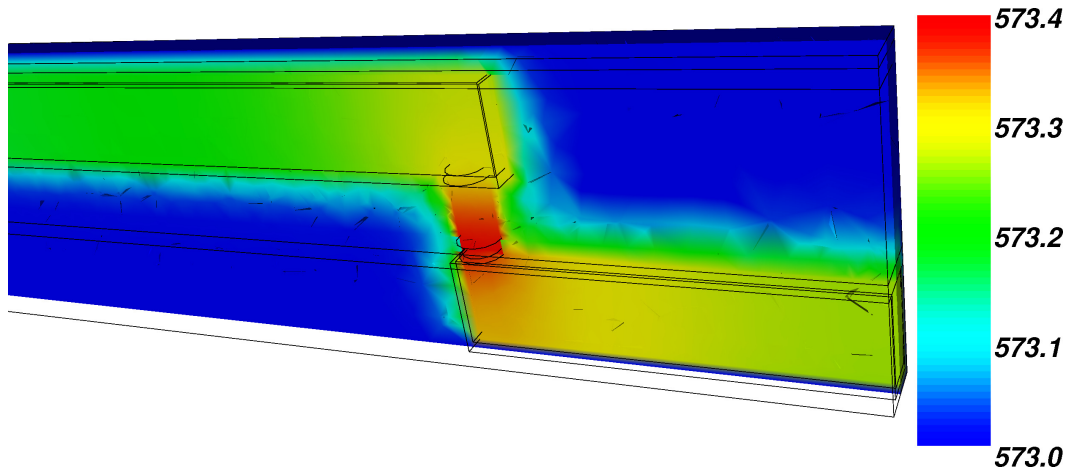

Figure 5.20: Detail of the temperature distribution in the via region through a cut along the x coordinate. A very small temperature increase in the via is caused by a higher joule heating in this region (in K).
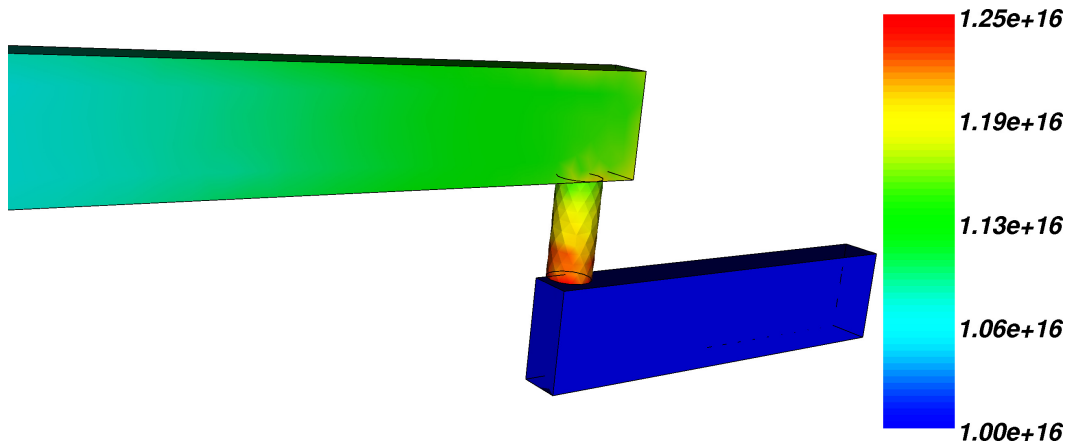

Figure 5.21: Vacancy distribution in the M2 line and via after $100\,\mathrm{h}$ of electromigration test (in cm^{-3}).
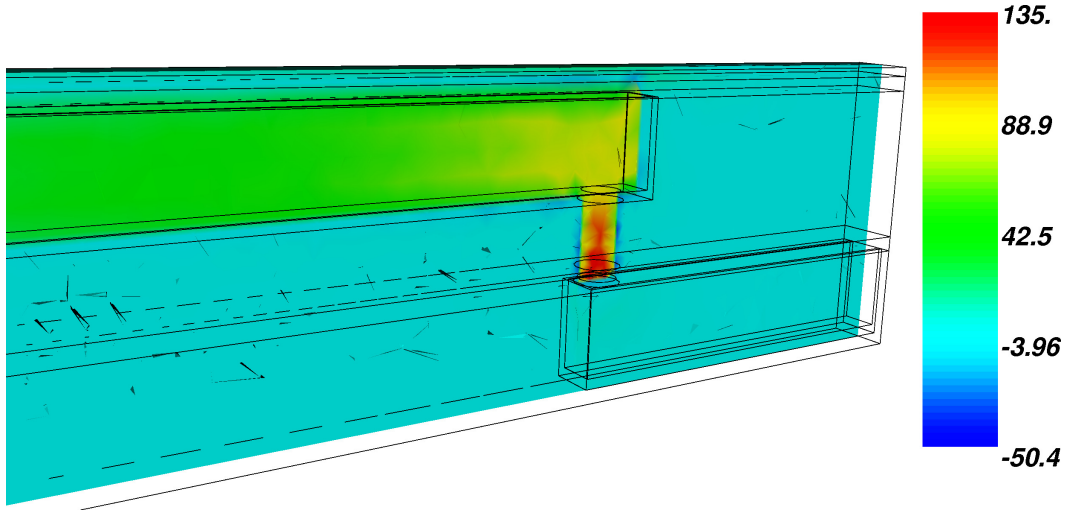
Figure 5.22: Stress distribution in the via region through a cut along the x coordinate after 100 h of electromigration test (in MPa).

From these observations one can infer that void nucleation takes place at the bottom of the via. This void can further develop and span the via bottom, which certainly leads to a significant increase of the line resistance, thus triggering the interconnect failure. This failure mechanism has been observed in electromigration experiments of copper dual-damascene interconnects [8, 114, 163], where it is frequently called via failure.

Although such a failure mechanism has been experimentally detected, several other mechanisms have been identified. For example, in a group of papers, Vairagar *et al.* [27, 31, 32, 114, 164] showed that most of the failures occurred due to growth of a void initially located at the copper/capping layer interface at the cathode end of the line. In fact, they observed that a void initially nucleates at the copper/capping layer interface at a site away from the cathode end and migrates towards the cathode end. There, this void grows by coalescence with other incoming voids. Therefore, via failure corresponds to just a fraction of an entire failure population.

A similar situation appears, when the direction of current flow (downstream electron flow) is reversed and the EM behavior in the M1 line is investigated. In this case vacancies accumulate through the whole line thickness under the via and, consequently, a high tensile stress develops, as shown in Figure 5.23 and in Figure 5.24, respectively. Thus, void nucleation is expected to occur at this site, right underneath the via. Here again, a similar trend as that for the upstream case appears. Although void nucleation at such a location has been experimentally observed [24], voids are more often seen to nucleate at a site away from the via [31, 32, 114] and also adjacent to the via [24].

From the discussion above one can see that using a single effective diffusivity value for the whole line can eventually explain some experimental findings. Nevertheless, several other observations cannot be described. For that purpose, a more meaningful and, at the same time, more realistic approach is required.
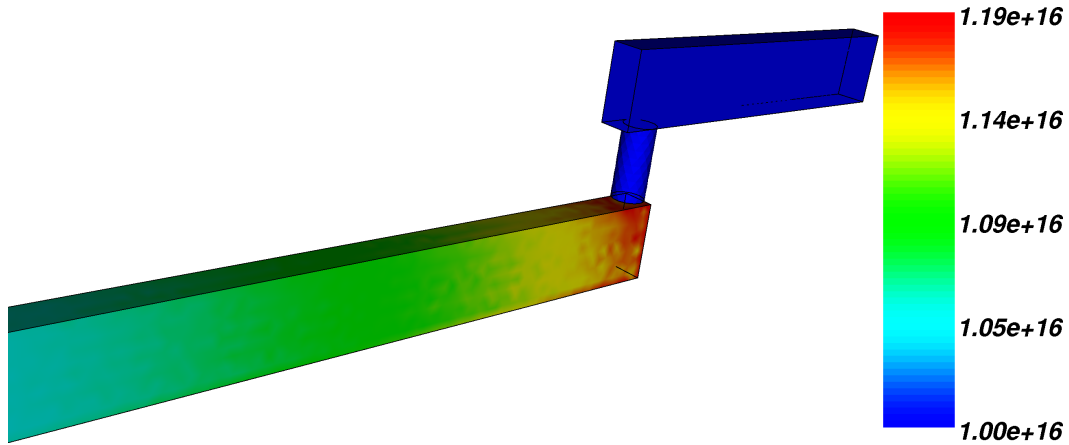
Figure 5.23: Vacancy distribution in the M1 line (downstream case) at $t = 100\,\text{h}$ (in cm^{-3}). Vacancies concentrate right underneath the via.
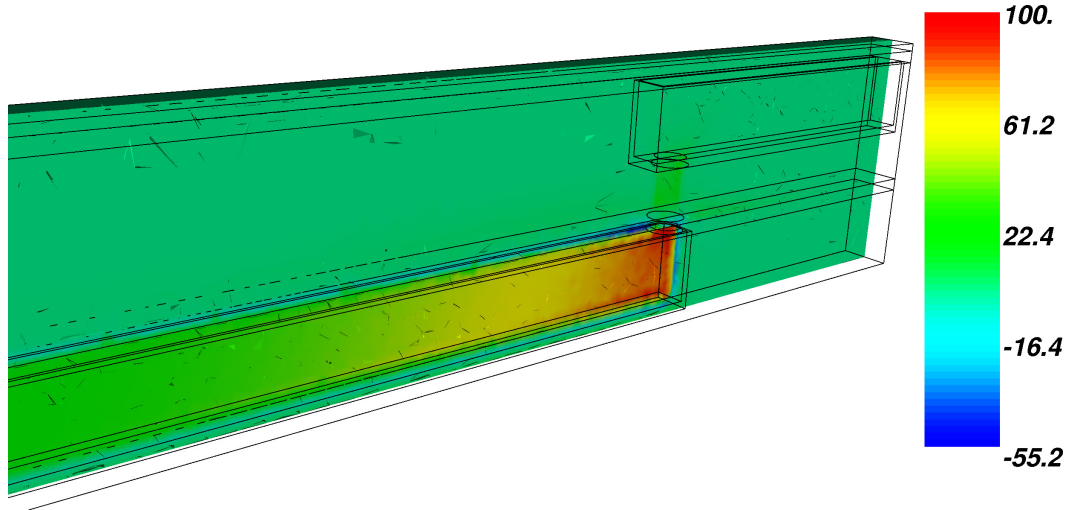
Figure 5.24: Hydrostatic stress due to downstream electromigration at $t = 100\,\text{h}$ (in MPa). The maximum stress is located right under the via.

It is widely accepted that the interfaces between the copper and the typical SiN based capping layers are the dominant paths for diffusion in copper interconnects [3, 13, 70]. Therefore, it will be shown that it is extremely important to discriminate the diffusivities for each path along the interconnect, instead of using a single effective value as done in the previous section.

For a copper dual-damascene line the activation energy for diffusion is about 0.89 eV [13, 159] along the copper/capping layer, about 1.2 eV [3, 158] for diffusion along the copper/barrier interface, and 2.1 eV [3, 158] for bulk diffusion. Applying these values in the simulations, the vacancy concentration and the stress distribution in the M2 line are shown in Figure 5.25 and in Figure 5.26, respectively.

There is a small vacancy concentration build-up at the bottom of the via, however, the

Figure 5.25: Vacancy concentration, when the copper/capping layer interface is treated as a fast diffusivity path (in cm^{-3}). Vacancies concentrate at the copper/capping layer interface at the cathode end of the line.

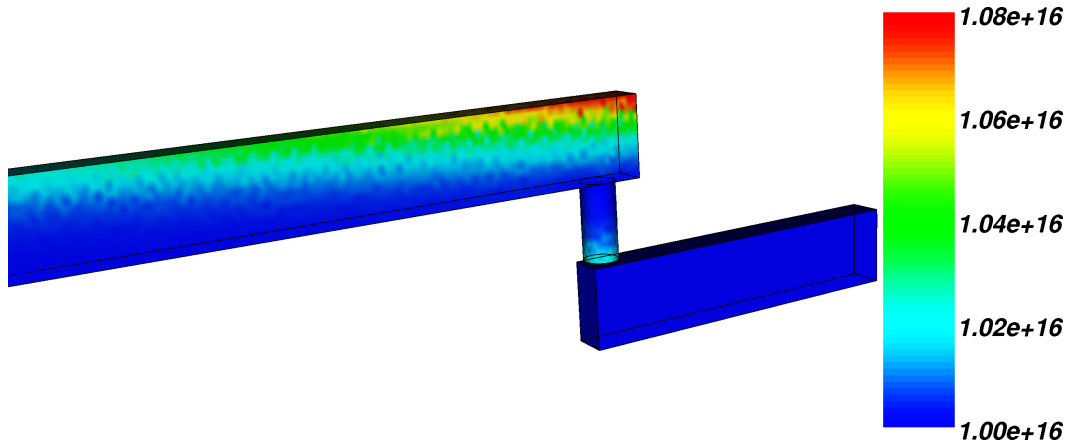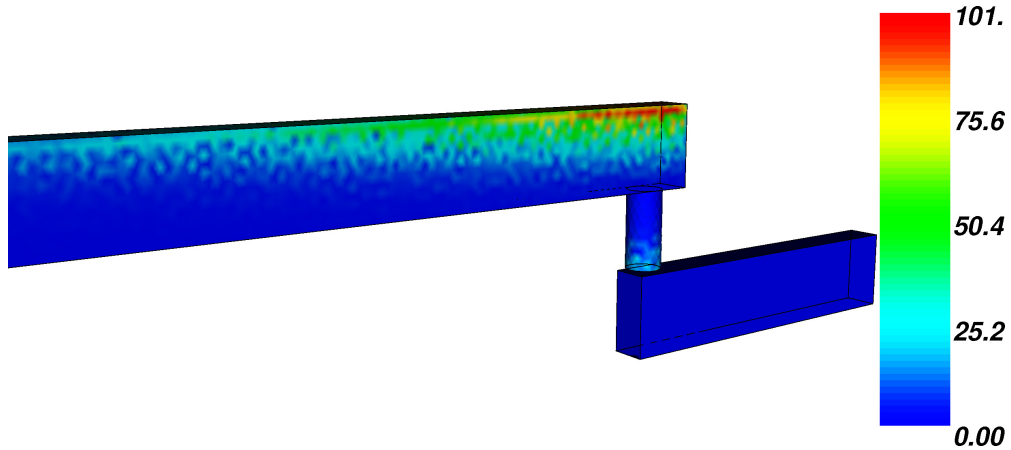**Figure 5.26:** The peak of hydrostatic stress is located at the copper/capping layer interface, when this interface acts as a fast diffusivity path (in MPa).

highest vacancy concentration is now located at the copper/capping layer interface at the cathode end of M2. The stress development follows the same trend. This is quite different compared to the results shown in the previous section, and is clearly a consequence of the higher diffusivity at the copper/capping layer interface. The high stress magnitude located at the copper/capping layer interface above the via can now explain the common experimental observation of void nucleation at such sites [8, 31, 32, 114, 164].

The vacancy concentration and the stress distribution for the downstream case are shown in Figure 5.27 and Figure 5.28, respectively. The main difference here is that the peak of the hydrostatic stress is not located right underneath the via, but is shifted to its edge, where there is an intersection between the copper, the capping layer, and the barrier layer. Since this intersection is likely to be a site of weak adhesion, void nucleation should occur at this edge, instead right underneath the via. This is in agreement with the observations commonly

86
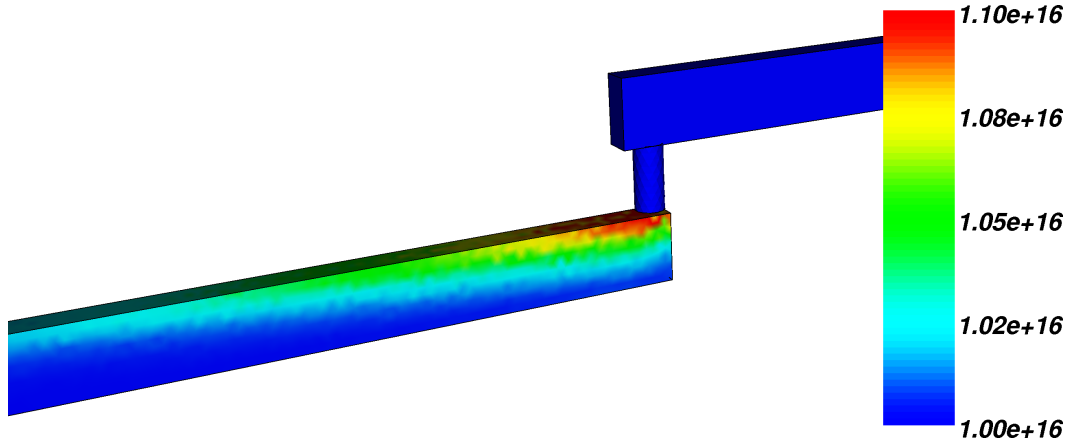
Figure 5.27: Vacancy distribution for the downstream case (in cm^{-3}).
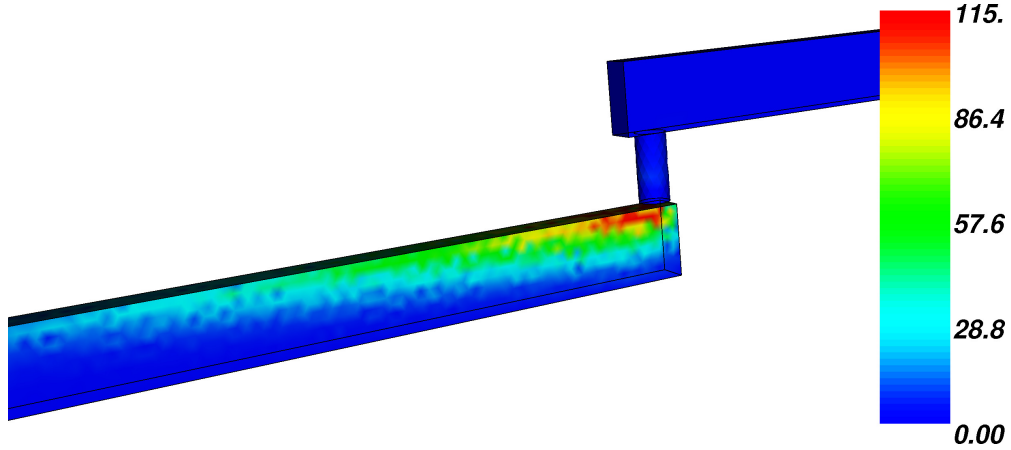
Figure 5.28: Hydrostatic stress distribution (in MPa). The peak of the stress is shifted to the left edge of the via, where copper, capping, and barrier layer intersect.

made in electromigration experiments [24].

These simulation results show the importance of incorporating the fast diffusivity paths into the modeling approach, which can be conveniently carried out by setting the correct diffusion coefficient for the copper/capping layer interface, for the copper/barrier layer interface, and for the bulk. In this way, it is demonstrated that the simulation results match some typical experimental observations regarding the void nucleation sites and, consequently, failure development. Specifically, the failure triggered by void growth at the bottom of the via, as well as by void growth at the copper/capping layer interface at the cathode end of the line can be explained. Nevertheless, the common observation of void nucleation taking place away from the cathode end of the line still cannot be reproduced. The introduction of material interfaces as fast diffusivity paths alone does not suffice. These observations can only be explained by taking into account the effect of the microstructure on electromigration, as will be shown later.

5.5 Redundant Via Structure

In order to design reliable interconnects against electromigration, a big effort has been put into investigating materials which produce preferable properties. However, another strategy which is commonly used to improve the interconnect resistance against electromigration is the introduction of specific geometrical features, such as material reservoirs [21, 165, 166] and redundant vias [19, 167]. Using two or more via contacts between interconnect levels has shown to be a very promising strategy for preventing stressmigration [19, 167] and electromigration [19]. Therefore, in this section some simulation results for interconnect structures containing two vias, as shown in Figure 5.29, are presented. In this way, the impact of the redundant via on the interconnect behavior regarding electromigration can be analyzed.
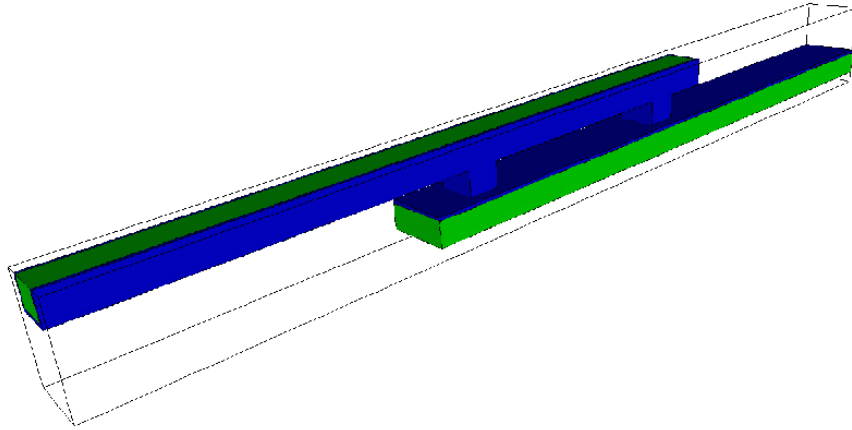
Figure 5.29: Interconnect structure with redundant via.

Figure 5.30 shows the vacancy distribution in a double via structure. Here, the simulations are carried out for a current density of 8 MA/cm^2, and the equilibrium vacancy concentration is 9.0×10^{15} cm^{-3}. The vacancy concentration is higher underneath the vias, as expected, since the electric current drives vacancies towards the vias (the current flows from right to left). Also, vacancies are concentrated at the interface between the copper and the capping layer, as this interface is the fastest diffusivity path. The vacancy concentration located under the outer (left) via is somewhat higher than the concentration under the inner (right) via, where current crowding occurs. These results indicate that, in this case, current crowding does not suffice to induce a higher vacancy flux divergence at the inner via. The higher vacancy concentration at the outer via is a consequence of a lower resistance for current flow along this path.

The corresponding stress development is shown in Figure 5.31. Note that a peak of hydrostatic stress develops at the outer via, as well as at the innermost via. The stress magnitude under the outer via is, however, somewhat higher, which is a consequence of the higher vacancy concentration at this region, as seen in Figure 5.30. These peaks are exactly located at the intersection of the copper with the capping and the barrier layer. Since the stress magnitude under both vias is similar, a void can nucleate under any of them. Void

Figure 5.30: Vacancy distribution in the double via structure (in cm^{-3}).

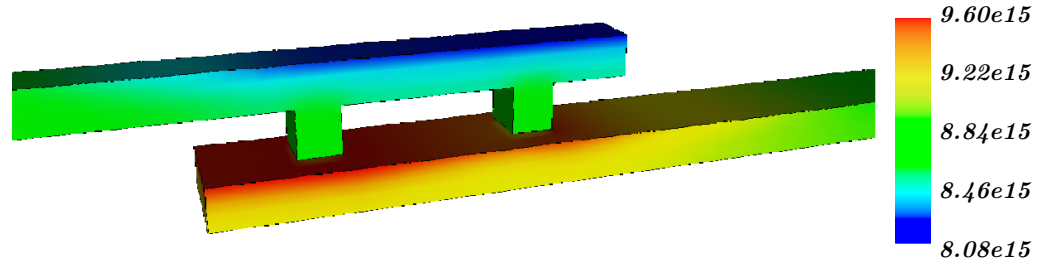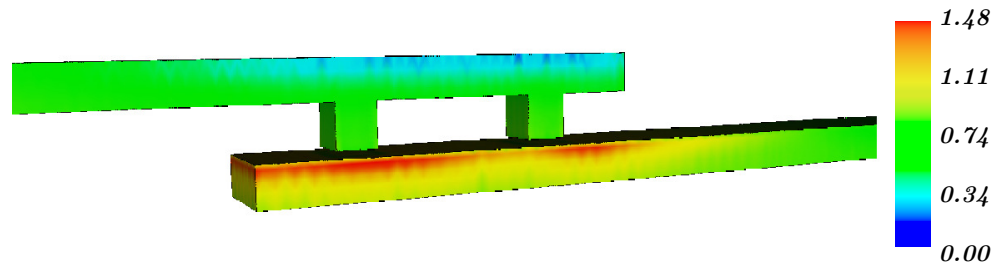**Figure 5.31:** Hydrostatic stress under the vias in a double via structure (in MPa). The stress peak is located under the outer via at the intersection between copper, capping layer, and barrier layer.

nucleation will take place, wherever the proper conditions are found, that is, at the site having the weakest adhesion between copper, capping, and barrier layer.

The impact of the distance between the vias on the maximum stress build-up is shown in Figure 5.32. The stress developed in the interconnect with redundant via is higher than that developed in the single via structure. The introduction of a second via reduces the overall interconnect resistance. As the voltage applied at the terminals of the interconnect is the same, the reduction of the interconnect resistance leads to an increase of the electric current. Consequently, the driving force for material transport along the line is increased, and more vacancies concentrate under the outer via of the redundant via structure, producing a higher stress. Another observation is that the stress also increases as the distance between the vias becomes larger. This is explained by the same argument as above. The larger is the distance between the vias, the smaller is the total line resistance, so that a higher current flows.

In order to avoid the current change, a constant current is applied to the interconnect structures. The stress build-up for the single and for the redundant via structures is presented in Figure 5.33. The second via provides an additional path for current conduction, so that the current flow through each via is smaller than the current flow through the single via. Therefore, the developed stress is smaller for the structures with the redundant via. Moreover, the stress magnitude is reduced as the distance between the vias increases. The increase of the distance between the vias corresponds to a decrease of the length between the innermost via and the end of the line, so that a smaller stress is needed to produce a gradient which counters the electromigration flux.
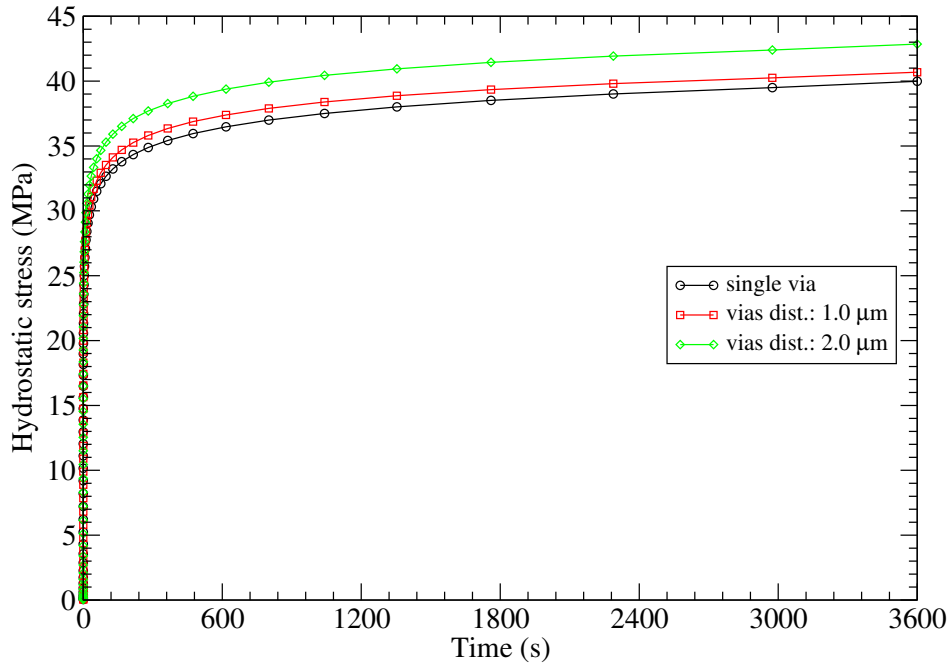
Figure 5.32: Maximum hydrostatic stress build-up under the outer via as a function of the distance between the vias for a constant voltage applied at the terminals of the interconnect.
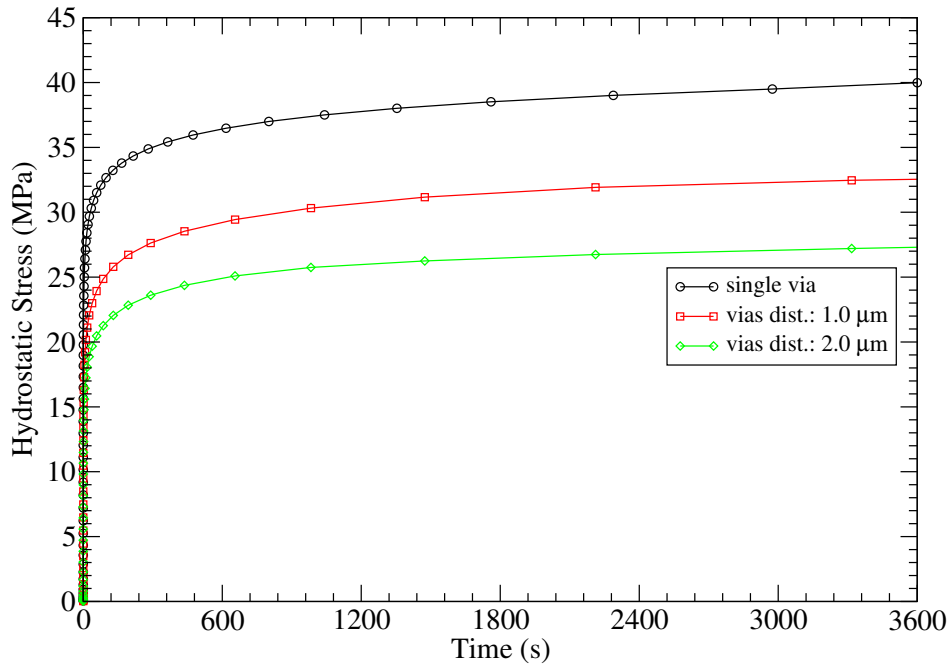

Figure 5.33: Stress development under the outer via for a constant current applied to the interconnect.

One can see that increasing the distance between the vias leads to significant changes in the stress distribution. Particularly, it is remarkable that the stress change under the inner via is more pronounced than the change of stress under the outer via, as shown in Figure 5.34. This behavior is observed for the constant voltage case, as well as for the constant current case. The main consequence of such a behavior is a change in the probable sites of void nucleation. As for small distances the stress magnitudes under both vias are likely to be similar, a void could nucleate in either the outer or innermost via, as already pointed out. However, increasing the distance the stress under the inner via is significantly reduced, which prevents void nucleation at this site. Therefore, it can be expected that a void nucleates only under the outer via.
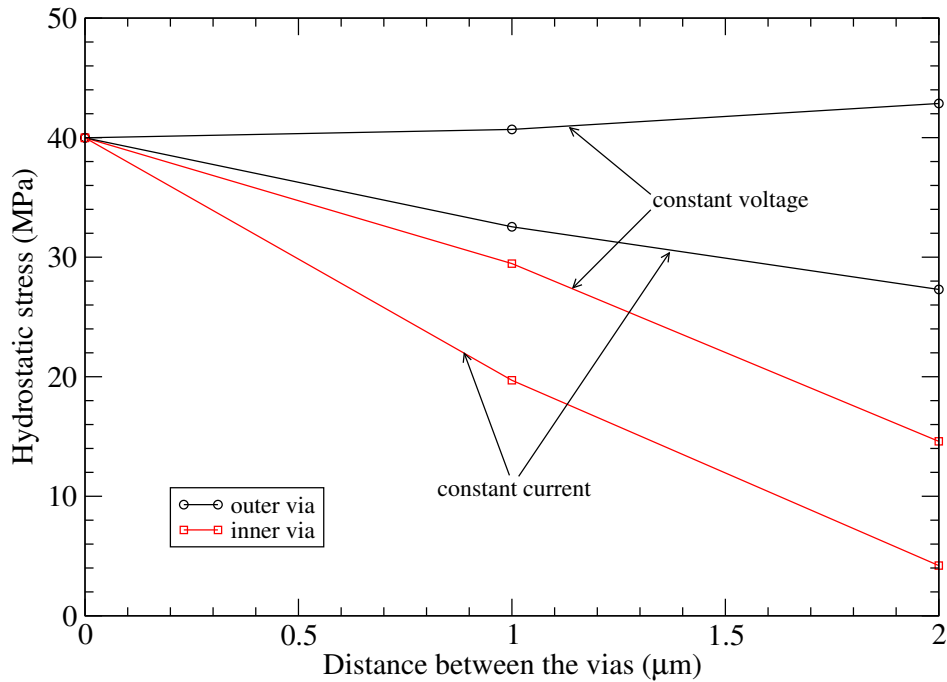
Figure 5.34: Maximum hydrostatic stress under the outer and inner via as a function of the distance between the vias. The stress for the single via case is given at zero distance between the vias.

These results indicate that the redundant via design offers only a limited ability in improving the interconnect lifetime. When a void nucleates under the inner via, it can grow through the line and span the entire cross section of the line, which interrupts the current flow along the metal. This certainly leads to an undesirable increase of the interconnect resistance and, consequently, interconnect failure. In this case, the redundancy for current flow provided by the outer via cannot help. In turn, a small increase in the distance between the vias allows void nucleation only in the outer via. Thus, even if the void grows and spans the line section, the resistance increase may not be critical, since the inner via still serves as a path for current conduction. This strategy requires, however, a larger metallization area which is not always available.

To sum up, the simulation results suggest that geometric features can have an important

impact on the ability of the interconnect to cope with electromigration, and the adequate design of a redundant via structure is crucial to effectively enhance the interconnect reliability regarding electromigration failure.

5.6 Effect of Microstructure on the Electromigration Lifetime Distribution

It has been shown that the microstructure plays a key role regarding the failure mechanisms in copper dual-damascene interconnects [71]. It affects electromigration in different ways. Grain boundaries are natural locations of atomic flux divergence, they act as fast diffusivity paths for vacancy diffusion [168], and they act as sites of annihilation and production of vacancies [148].

Electromigration data have been described by lognormal distributions [22]. Although the origin of the lognormal distribution of electromigration lifetimes is not entirely clear, it has been argued that the diffusion process in connection with the effect of microstructure on electromigration provides the basis for the lognormal distribution [20]. In copper dual-damascene interconnects the main diffusivity path is along the copper/capping layer interface. This interfacial diffusion is affected by the orientation of the grains. As the copper grain sizes seem to follow lognormal distributions in typical dual-damascene process technology [20], and due to the influence of microstructure on the electromigration process, the lognormal distribution has been used as the underlying statistics for electromigration lifetimes.

Understanding the electromigration lifetime distribution is crucial for the extrapolation of the times to failure obtained empirically from accelerated tests to real operating conditions, as performed by equation (1.23). Therefore, in this section the statistical distribution of electromigration times to failure as a function of the distribution of copper grain sizes is investigated. The discussion is focused on the impact that the variation of the standard deviation of the grain size distribution has on the electromigration lifetimes, and the consequences of the latter for reliability assessment of interconnects.

5.6.1 Microstructure Generation

In order to include the grain distribution into the numerical simulations, a microstructure generation tool has been developed. Given a specific interconnect structure and providing the tool with a median grain size, x_0, and corresponding standard deviation, σ, it generates a lognormal distribution of grain sizes according to

$$pdf(x) = \frac{1}{x\sigma\sqrt{2\pi}} \exp\left[-\frac{(\ln x - \ln x_0)^2}{2\sigma^2}\right].$$
(5.12)

The angles between the grain boundaries' planes and the line surface at the top follow a normal distribution,

$$pdf(x) = \frac{1}{\sigma\sqrt{2\pi}} \exp\left[-\frac{(x - x_0)^2}{2\sigma^2}\right],$$
(5.13)

where $x_0 = 90°$ is the median value of the angles. Taking a radom number, $y \in [0, 1]$, uniformly distributed, the grain sizes and grain boundary angles are determined by calculating z, so that the inverse relation,

$$y = \int_{-\infty}^{z} pdf(x) \ dx, \tag{5.14}$$

holds. Once the grain sizes and angles are determined, the interconnect line is cut along its length by the planes which form the grain boundaries. A typical microstructure generated by such a procedure is shown in Figure 5.35. In this way, the microstructure generation tool yields a simple bamboo-like line.
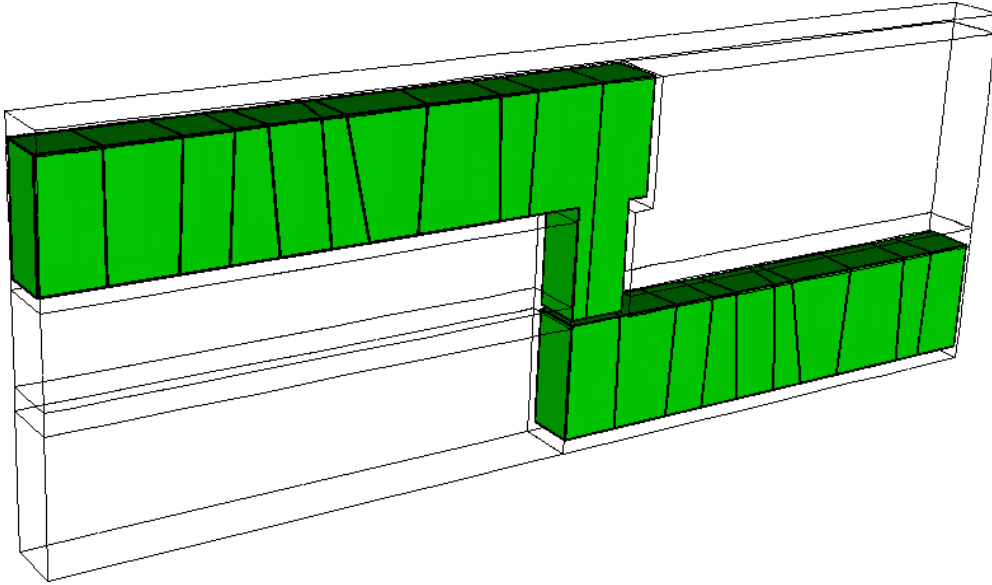
Figure 5.35: Typical microstructure generated from the procedure described above. The grain sizes follow a lognormal distribution, and the angles of the grain boundaries in relation to the top line surface follow a normal distribution.

5.6.2 Simulation Approach

In Figure 5.36 a schema of the simulation procedure used to determine the distribution of electromigration lifetimes is presented. First, several interconnects are generated, each one having a different microstructure which is produced by the microstructure generator (see Section 5.6.1). The structures are simulated and the electromigration lifetimes are determined. The lifetimes are then used for statistical analysis, from where the corresponding distribution, specified by the mean time to failure and standard deviation, is obtained.

Three standard deviations for the distribution of grain sizes are considered, namely 0.1, 0.3 and 0.6. For each of them 20 dual-damascene interconnect structures are created. As the interconnect line is assumed to present a bamboo-like structure, the median grain size is equal to the line width, 0.10 μm. The barrier, capping and interlayer dielectric layers are Ta, SiN, and SiO$_2$, respectively. The applied current density is 1.5 MA/cm^2, and the test temperature is 300 °C. A stress threshold value as failure criterion is used, which means that

the electromigration time to failure represents the time for a void nucleation to occur. Thus, the time to failure is determined by the time for the stress to reach a given threshold value at some intersection between a grain boundary and the capping layer.

It should be pointed out that the model parameters are equal for all simulated structures. Grain boundaries, and generally, every interface of the structure have to be supplied with an appropriately fine mesh. Therefore, the mesh refinement procedure described in Section 4.3.5 is used. This is necessary in order to provide sufficient resolution for the results along the grain boundaries and other interfaces.
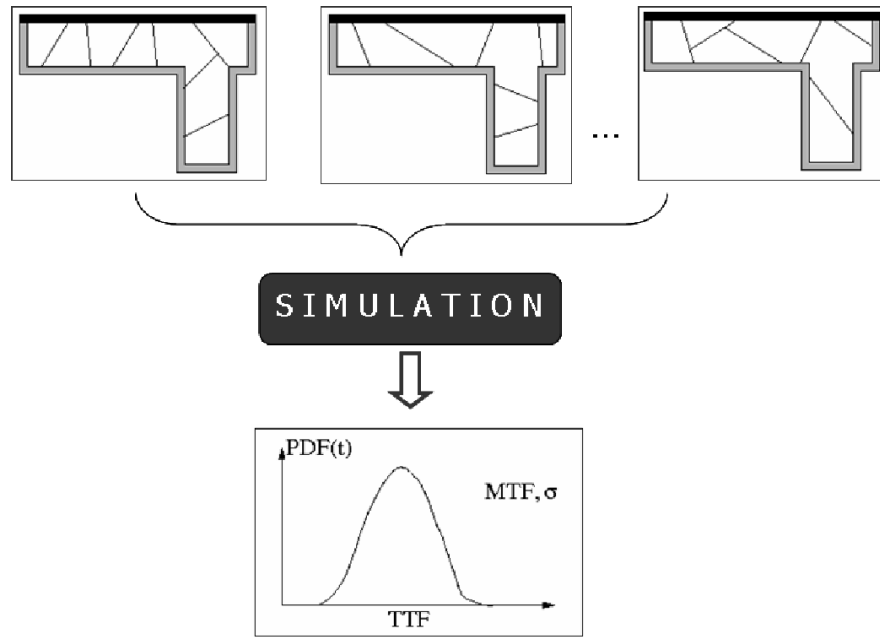
Figure 5.36: Schematic simulation procedure.

5.6.3 Sites of Void Nucleation

Figure 5.37 shows the vacancy distribution in a bamboo-like interconnect via. The current flows from right to left, driving vacancies towards the via. Vacancies concentrate at this site, because the barrier layer blocks further vacancy diffusion into the upper metal line. Thus, the maximum vacancy concentration is located underneath the via. However, as already pointed out, grain boundaries also act as fast diffusivity paths. Consequently, vacancy diffusion along grain boundaries is an important transport mechanism, which leads to higher vacancy concentration along the grain boundary planes, as shown in Figure 5.37.

According to the grain boundary model presented in Section 3.4.1, once the vacancy concentration within a grain boundary exceeds the equilibrium concentration, the grain boundary is able to trap the excess vacancies. Therefore, the trapped vacancy concentration within the grain boundaries increases, as shown in Figure 5.38.

The rate at which vacancies are trapped/released from the grain boundary corresponds to an annihilation/generation term, as given in equation (3.50). In turn, generation/annihilation
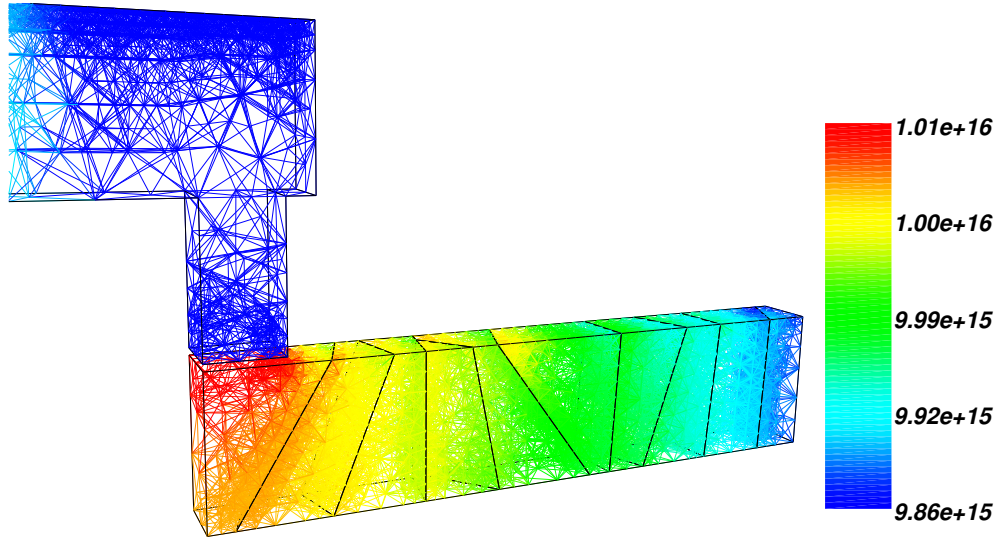
Figure 5.37: Vacancy distribution in a bamboo-like interconnect line (in cm^{-3}).
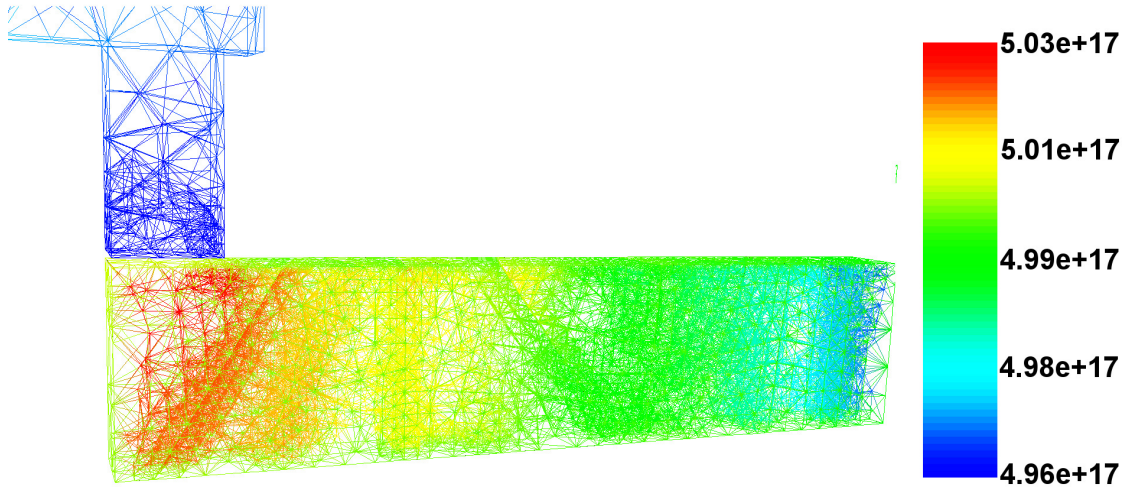
Figure 5.38: Trapped vacancy concentration (in cm^{-3}). Vacancies are trapped at grain boundaries, once the vacancy concentration within a grain boundary exceeds the equilibrium value.

processes lead to production of mechanical stress, according to (3.42). Thus, the stress build-up closely follows the trapped vacancy concentration and develops at grain boundaries, as can be seen in Figure 5.39.

These results are crucial in order to explain the void nucleation at sites away from the cathode end of the line [27]. Void nucleation observed at the copper/capping layer away from the cathode end is only possible provided there is an available site where flux divergence occurs and, at the same time, is a site of weak adhesion. Grain boundaries are the only
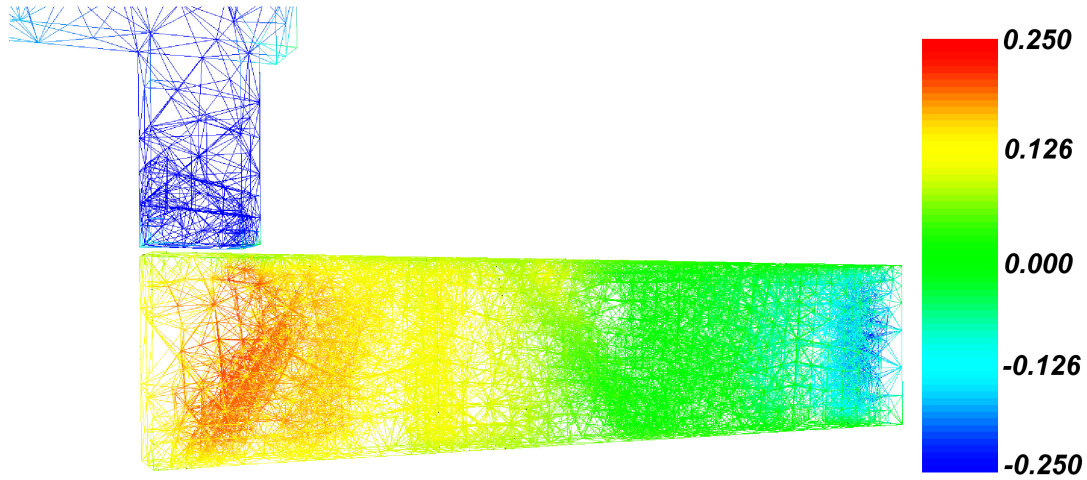
Figure 5.39: Hydrostatic stress distribution in a simulated interconnect (in MPa). Mechanical stress develops at grain boundaries as a result of vacancy trapping/release events.

features which can provide such sites. Since triple points formed by the intersection of grain boundaries with the copper/capping layer interface are natural places of flux divergence and weak adhesion [31], the development of mechanical stress at these sites, as shown in Figure 5.39, can explain void nucleation in the middle of the line.

The introduction of the grain boundary network into the simulations, together with the consideration of material interfaces as fast diffusivity paths, represents a significant improvement of the developed model, so that the most common experimental observations regarding electromigration induced void nucleation can be explained.

5.6.4 Electromigration Lifetimes Distribution

Figure 5.40 shows the hydrostatic tensile stress development for the structures with a grain size standard deviation of 0.3. The stress peak value follows the peak of the trapped vacancy concentration and is located at the intersection of grain boundaries with the capping layer, as shown in Figure 5.39.

Collecting the times to failure from Figure 5.40 and calculating the cumulative failure percentages results in the distributions of electromigration lifetimes shown in Figure 5.41. The lifetimes are fitted by lognormal distributions. The mean time to failure is determined by the 50% cumulative failure mark, and the slope of the curves corresponds to the inverse of the standard deviation of lifetimes. The obtained standard deviations are 0.0065, 0.0080, and 0.0085 for the grain size distributions with standard deviation of 0.1, 0.3, and 0.6, respectively.

When the grain size distribution exhibits a smaller standard deviation the corresponding interconnect lines have a more uniform distribution of the grains. As a consequence, the stress build-up has smaller variations yielding a smaller standard deviation of the electromigration lifetimes. On the other hand, increasing the grain size standard deviation, the lines exhibit
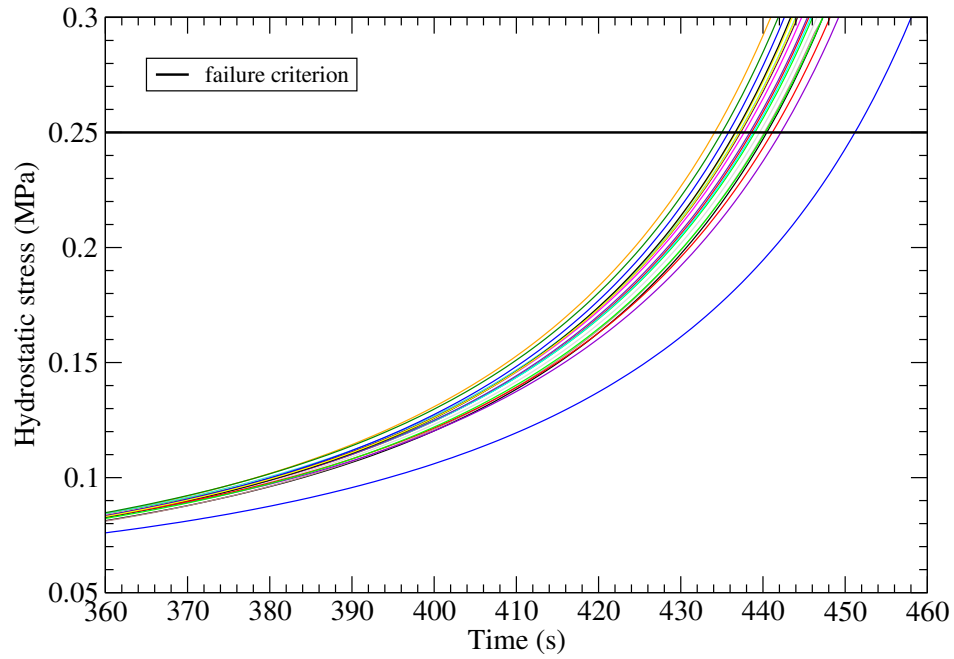
Figure 5.40: Peak of hydrostatic stress development for the set with grain size standard deviation of 0.3.
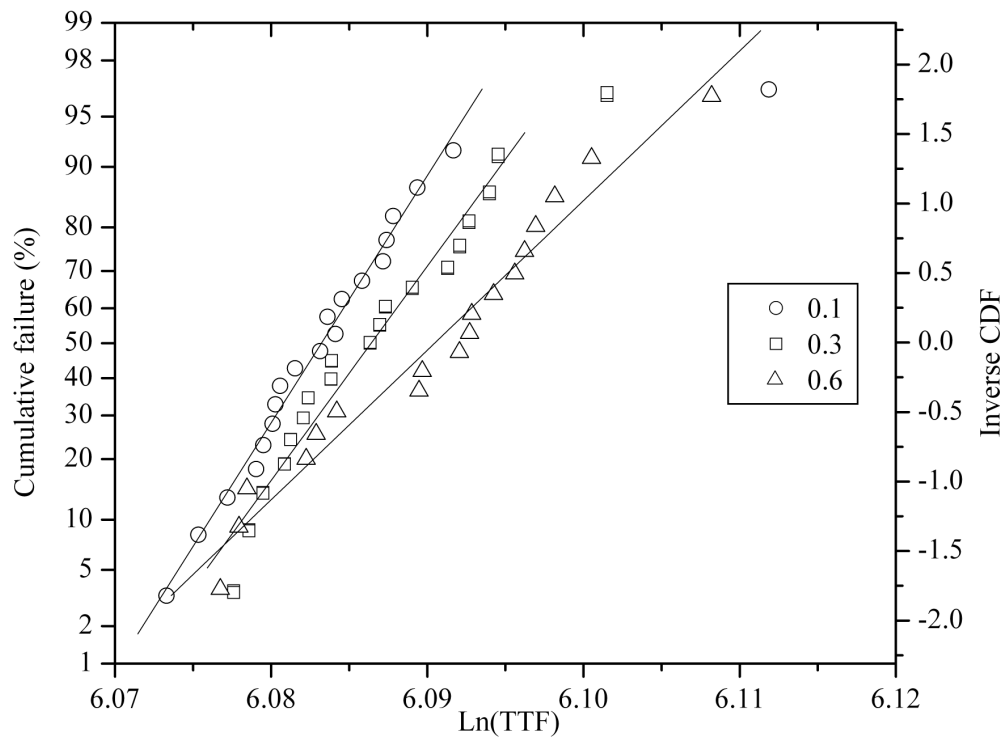
Figure 5.41: Electromigration lifetime distributions.

significant differences in the grain structures. This leads to larger variations of stress development. Thus, a bigger standard deviation of electromigration lifetimes is expected. The increase of the standard deviation of the electromigration lifetime distribution as a function of the standard deviation of the distribution of grain sizes is shown in Figure 5.42.
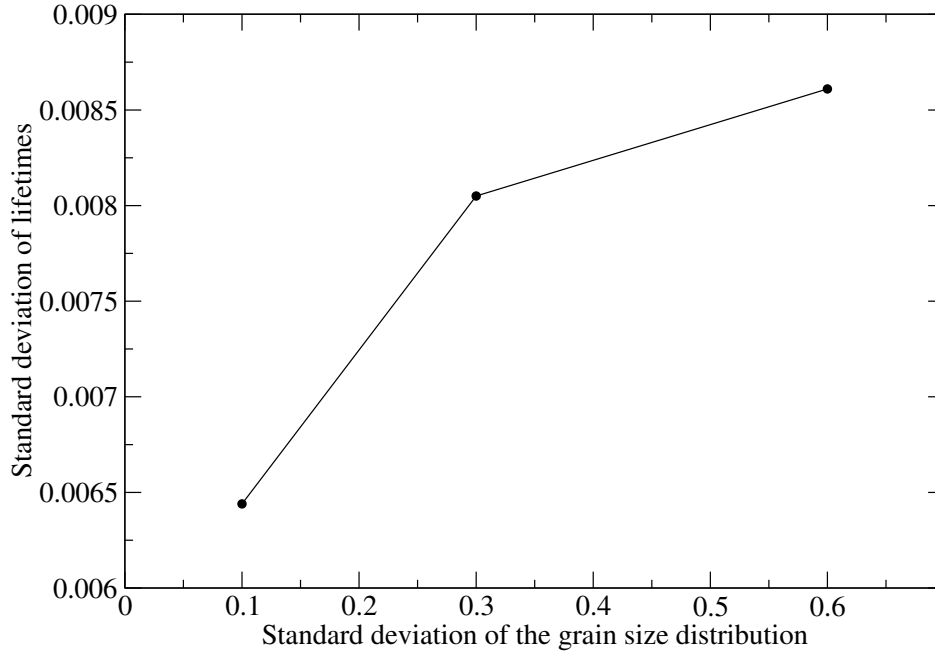
Figure 5.42: Electromigration lifetime standard deviation for different standard deviations of grain size.

The standard deviations of the electromigration lifetimes are very small compared to those frequently observed in experiments [22]. Several factors can explain this behavior. First, for convenience, a small value of stress threshold as failure criterion is used to determine the interconnect lifetime. The complexity of the physical model associated with the numerical features posed by the microstructure makes the simulations inconveniently demanding. As can be seen from Figure 5.40, the variation of the lifetimes can be more pronounced for higher stress thresholds. Second, the simulation parameters and material properties are independent of the grain distribution. This means that mechanical properties and diffusivities, for example, are equal and constant for all simulated structures. This is clearly not the case in real experiments, as it is well known that material properties vary according to the grain network. It is expected that atomic diffusion along the copper/capping layer interface changes from grain to grain, inducing a flux divergence at the corresponding grain boundary. Moreover, the diffusivities are different from line to line as the grain distribution varies. Therefore, given the above simplifications, the small standard deviations obtained from the simulations should be expected.

Nevertheless, these results present important features which are worth a careful analysis. As a consequence of the larger lifetime standard deviation for the lines with $\sigma = 0.6$, the early failures (failure percentages lower than 1% in Figure 5.41) occur at shorter times, even though the median lifetime is higher for these lines. This observation is of great importance to the

extrapolation of accelerated test results to normal use conditions. This can be readily seen from an inspection of equation (1.23), which shows that the estimation of the real lifetimes has an exponential dependence on the standard deviation of lifetimes obtained by the accelerated tests.

Considering that the reliability assessment of a given technology is determined by the early failures, the understanding of the lifetime distribution becomes crucial. This means that the improvement of processes, and the choice of adequate materials, aiming the improvement of a given interconnect technology requires not only the increase of the median lifetime of an interconnect structure, but also the reduction of the corresponding standard deviation.

Chapter 6

Conclusion and Outlook

Electromigration induced failure has been one of the major reliability issues for the microelectronic industry since its detection as a potential damage mechanism in metallization of integrated circuits. Since then, efforts have been made in order to design more resistant interconnects against electromigration damage. This has encompassed the development of new fabrication processes, the research of materials which yield adequate properties, and the design of specific geometrical features.

The continuous scaling of devices demands a continuous reduction of the metal line dimensions, which is accompanied by an increase in the density of interconnections in modern integrated circuits. Therefore, the interconnect lines have to operate at high temperatures and conduct high current densities, accentuating the electromigration transport. As a consequence, electromigration continues to be a challenge for the development of the new technological nodes, and the lifetime of interconnects have decreased from generation to generation, despite all the knowledge gained and efforts performed in the last 40 years.

The investigation of the physical phenomena behind the electromigration damage has become more and more important, because it can provide a stronger knowledge basis to counter the electromigration effect. In this context, mathematical modeling becomes an important tool which can significantly help to understand the electromigration failure. In the last decades, several continuum models have been proposed, and they have been able to partially explain several features of the electromigration damage. At the same time, the development of computational methods and resources has allowed to model complex systems and carry out numerical simulations in an efficient way.

In the scope of this work, the focus was put on developing a mathematical model suitable for implementation in a TCAD tool for numerical simulations. Electromigration modeling constitutes a complex problem due to the wide variety of physical effects which must be considered. A detailed study of the previous available models was carried out, identifying their main strengths and, at the same time, their main problems. Based on this analysis, these models were extended and further developed by taking into account the most relevant effects for electromigration simulation. As a result, a fully three-dimensional model is proposed, which connects the electromigration material transport problem with the electro-themal and mechanical problem in a general framework. The model equations were numerically described

using the finite element method. The corresponding system of algebraic equations was derived and implemented in a TCAD tool.

In order to verify the developed model and numerical implementation, simulations in a simple interconnect line were carried out and compared with the available analytical solutions. The agreement between the numerical simulation results and the analytical solutions is remarkably good. Also, the importance of taking into account the effects of mechanical stress for electromigration modeling was demonstrated. The mechanical stress significantly affects the diffusivity of vacancies and, consequently, the electromigration induced transport. The non-uniform stress distribution which appears in the interconnect structure due to thermal processes leads to an anisotropic diffusivity. This effect is not readily visible under accelerated test conditions, however, it becomes much more important at real use conditions. Therefore, the activation energies for diffusion obtained from the accelerated tests are likely to be incorrect, posing a problem for the extrapolation of lifetimes to normal operating conditions.

A key feature of the proposed model is the inclusion of material interfaces and grain boundaries as paths of higher vacancy diffusion. Instead of considering a simple effective diffusion as valid for the entire interconnect, the correct diffusion coefficient can be independently set for each path, namely, the copper/capping layer interface, the copper/barrier interface, grain boundaries and bulk. In this way, it was shown that the most common experimental observations of electromigration induced voiding can be explained. Since the copper/capping layer interface is known to be the fastest path, it was shown that void nucleation typically occurs at this interface, at the cathode end of the line.

The model was further developed by considering grain boundaries as sites capable of trapping and releasing vacancies. This allowed the connection of the local dynamics of the grain boundary with the corresponding line deformation, and consequent mechanical stress build-up. Grain boundaries are introduced by a simple microstructure generator. In this way, it was shown that the combination of material interfaces as fast diffusivity paths together with the grain boundary model can explain void nucleation away from the cathode end. Voids nucleate at triple points formed by the intersection between the copper/capping layer interface with grain boundaries.

The microstructure has a major impact on the electromigration lifetime distribution. The simulation results indicate that the lognormal distribution of copper grain sizes is a primary cause for the lognormal distribution of the electromigration lifetimes. The increase of the standard deviation of the copper grain size distribution leads not only to longer mean times to failure, but also to larger variations of lifetimes. The first is naturally a beneficial effect, the latter, however, can be harmful for the interconnect reliability assessment. The increase of the standard deviation of lifetimes has a significant impact on correct lifetime estimation, since the increase of the standard deviation of lifetimes may indicate that a given interconnect technology fails earlier than expected, even if it shows a longer median lifetime.

To sum up, a complex and robust TCAD electromigration model which takes into account a wide diversity of physical phenomena was developed. Several numerical simulations of realistic three-dimensional interconnect structures were carried out, and several features of the electromigration failure were explained.

Nevertheless, there are still several points which should be improved, and they are suggestions for future work. From the physical modeling point of view a natural extension of

this work is to develop a void evolution model also suitable for TCAD implementation and for three-dimensional simulations. This is a challenging task, since the void evolution problem requires the consideration of additional physical phenomena and, moreover, represents a moving boundary problem. This demands special numerical techniques for tracking the void surface as it evolves. Also, further investigations regarding the microstructure impact on the electromigration distribution are required. For that purpose, the use of a more realistic microstructure is needed. This will provide a more complete understanding of the underlying statistics of the electromigration lifetime distribution, which, in turn, can significantly contribute to the practical lifetime estimation and interconnect design.

Bibliography

[1] H. B. Huntington and A. R. Grone, "Current-Induced Marker Motion in Gold Wires," *J. Phys. Chem. Solids*, vol. 20, no. 1, pp. 76–87, 1961.

[2] J. Noguchi, T. Oshima, T. Matsumoto, S. Uno, and K. Sato, "Multilevel Interconnect with Air-Gap Structure for Next-Generation Interconnections," *IEEE Trans. Electron. Dev.*, vol. 56, no. 11, pp. 2675–2682, 2009.

[3] J. R. Lloyd, J. Clemens, and R. Snede, "Copper Metallization Reliability," *Microelectron. Reliab.*, vol. 39, pp. 1595–1602, 1999.

[4] C. K. Hu and J. M. E. Harper, "Copper Interconnections and Reliability," *Mater. Chem. Phys.*, vol. 52, pp. 5–16, 1998.

[5] *International Technology Roadmap for Semiconductors*, 2010.

[6] P. R. Justison, "Analysis of Electromigration in Single- and Dual-Inlaid Cu Interconnects," Dissertation, The University of Texas at Austin, 2003.

[7] F. L. Wei, C. L. Gan, T. L. Tan, C. S. Hau-Riege, A. P. Marathe, J. J. Vlassak, and C. V. Thompson, "Electromigration-Induced Extrusion Failures in Cu/Low-k Interconnects," *J. Appl. Phys.*, vol. 104, p. 023529, 2008.

[8] L. M. Gignac, C.-K. Hu, and E. G. Liniger, "Correlation of Electromigration Lifetime Distribution to Failure Mode in Dual–Damascene Cu/SiLK Interconnects," *Microelectron. Eng.*, vol. 70, pp. 398–405, 2003.

[9] T. Matrieb, P. A. Flinn, J. C. Bravman, D. Gardner, and M. C. Madden, "Observations of Electromigration Induced Void Nucleation and Growth in Polycristalline and Near-Bamboo Passivated Al Lines," *J. Appl. Phys.*, vol. 78, no. 2, pp. 1026–1032, 1995.

[10] Z. S. Choi, R. Mönig, and C. V. Thompson, "Effects of Microstructure on the Formation, Shape, and Motion of Voids during Electromigration in Passivated Copper Interconnects," *J. Mater. Res.*, vol. 23, no. 2, pp. 383–391, 2008.

[11] P. R. Besser, M. C. Madden, and P. A. Flinn, "In Situ Scanning Electron Microscopy Observation of the Dynamic Behavior of Electromigration Voids in Passivated Aluminum Lines," *J. Appl. Phys.*, vol. 72, no. 8, pp. 3792–3797, 1992.

[12] J. P. Gambino, T. C.Lee, F. Chen, and T. D. Sullivan, "Reliability Challenges for Advanced Copper Interconnects: Electromigration and Time-Dependent Dielectric Breakdown (TDDB)," *Proc. Intl. Symp. on the Physical and Failure Analysis of Integrated Circuits*, pp. 677–684, 2009.

[13] C.-K. Hu, L. M. Gignac, and R. Rosenberg, "Electromigration of Cu/Low Dielectric Constant Interconnects," *Microelectron. Reliab.*, vol. 46, pp. 213–231, 2006.

[14] C.-K. Hu, D. Canaperi, S. T. Chen, L. M. Gignac, B. Herbst, and S. Kaldor, "Effects of Overlayers on Electromigration Reliability Improvement for Cu/Low-k Interconnects," *Proc. Intl. Reliability Physics Symp.*, pp. 222–227, 2004.

[15] O. Dubreuil, M. Cordeau, T. Mourier, P. Chausse, M. Mellier, D. Bellet, and J. Torres, "Characterization of Copper Grain Growth Limitations Inside Narrow Wires Depending of Overburden Thickness," *Microelectron. Eng.*, vol. 85, pp. 1988–1991, 2008.

[16] B. Yao, T. Sun, V. Kumar, K. Barmak, and K. R. Coffey, "Grain Growth and Void Formation in Dielectric-Encapsulated Cu Thin Films," *J. Mater. Res.*, vol. 23, no. 7, pp. 2033–2039, 2008.

[17] G. C. Schwartz and K. V. Srikrishnan, "Metallization," *in Handbook of Semiconductor Interconnection Technoogy, edited by G. C. Schwartz and K. V. Srikrishnan*, pp. 311–383, 2006.

[18] C.-K. Hu, L. M. Gignac, B. Baker, E. G. Liniger, and R. Yu, "Impact of Cu Microstructure on Electromigration Reliability," *Proc. Intl. Interconnect Technology Conf.*, pp. 93–95, 2007.

[19] A. von Glasow, "Zuverlässigkeitsaspekte von Kupfermetallisierungen in Integrierten Schaltungen," Dissertation, Technische Universität München, 2005.

[20] M. Hauschildt, "Statistical Analysis of Electromigration Lifetimes and Void Evolution in Cu Interconnects," Dissertation, The University of Texas at Austin, 2005.

[21] E. T. Ogawa, K.-D. Lee, V. A. Blaschke, and P. S. Ho, "Electromigration Reliability Issues in Dual-Damascene Cu Interconnections," *IEEE Trans. on Reliability*, vol. 51, no. 4, pp. 403–419, 2002.

[22] M. Hauschildt, M. Gall, S. Thrasher, P. Justison, R. Hernandez, H. Kawasaki, and P. S. Ho, "Statistical Analysis of Electromigration Lifetimes and Void Evolution," *J. Appl. Phys.*, vol. 101, p. 043523, 2007.

[23] J. Lloyd and J. Kitchin, "The Electromigration Failure Distribution: The Fine-Line Case," *J. Appl. Phys.*, vol. 69, no. 4, pp. 2117–2127, 1991.

[24] B. Li, C. Christiansen, J. Gill, R. Filippi, T. Sullivan, and E. Yashchin, "Minimum Void Size and 3-Parameter Lognormal Distribution for EM Failures in Cu Interconnects," *Proc. Intl. Reliability Physics Symp.*, pp. 115–122, 2006.

[25] S. C. Lee and A. S. Oates, "Identification and Analysis of Dominant Electromigration Failure Modes in Copper/Low-k Dual-Damascene Interconnects," *Proc. Intl. Reliability Physics Symp.*, pp. 107–114, 2006.

[26] M. W. Lane, E. G. Liniger, and J. R. Lloyd, "Relationship Between Interfacial Adhesion and Electromigration in Cu Metallization," *J. Appl. Phys.*, vol. 93, no. 3, pp. 1417–1421, 2003.

[27] M. Y. Yan, J. O. Suh, F. Ren, K. N. Tu, A. V. Vairagar, S. G. Mhaisalkar, and A. Krishnamoorthy, "Effect of Cu_3Sn Coatings on Electromigration Lifetime Improvement of Cu Dual-Damascene Interconnects," *Appl. Phys. Lett.*, vol. 87, p. 211103, 2005.

[28] E. Zschech, H. J. Engelmann, M. A. Meyer, V. Kahlert, A. V. Vairagar, S. G. Mhaisalkar, A. Krishnamoorthy, M. Yan, K. N. Tu, and V. Sukharev, "Effect of Interface Strength on Electromigrationinduced Inlaid Copper Interconnect degradation: Experiment and Simulation," *Z. Metallkunde*, vol. 96, no. 9, pp. 966–971, 2005.

[29] N. D. McCusker, H. S. Gamble, and B. M. Armstring, "Surface Electromigration in Copper Interconnects," *Microelectron. Reliab.*, vol. 40, pp. 69–76, 2000.

[30] H. Kang, I. Asano, C. Ryu, and S. Wong, "Grain Structure amd Electromigration Properties of CVD Cu Metallization," *Proc. Intl. VLSI Multilevel Interconnection Conf.*, pp. 223–229, 1993.

[31] A. V. Vairagar, S. G. Mhaisalkar, A. Krishnamoorthy, K. N. Tu, A. M. Gusak, M. A. Meyer, and E. Zschech, "In Situ Observation of Electromigration-Induced Void Migration in Dual-Damascene Cu Interconnect Structures," *Appl. Phys. Lett.*, vol. 85, no. 13, pp. 2502–2504, 2004.

[32] A. V. Vairagar, S. G. Mhaisalkar, M. A. Meyer, E. Zschech, A. Krishnamoorthy, K. N. Tu, and A. M. Gusak, "Direct Evidence of Electromigration Failure Mechanism in Dual-Damascene Cu Interconnect Tree Structures," *Appl. Phys. Lett.*, vol. 87, no. 081909, 2005.

[33] W. Shao, S. G. Mhaisalkar, T. Sritharan, A. V. Vairagar, H. J. Engelmann, O. Aubel, E. Zschech, A. M. Gusak, and K. N. Tu, "Direct Evidence of Cu/Cap/Liner Edge Being the Dominant Electromigration Path in Dual-Damascene Cu Interconnects," *Appl. Phys. Lett.*, vol. 90, no. 052106, 2007.

[34] J. Proost, T. Hirato, T. Furuhara, and J.-P. Celis, "Microtexture and Electromigration-Induced Drift in Electroplated Damascene Cu," *J. Appl. Phys.*, vol. 87, no. 6, pp. 2792–2802, 2000.

[35] G. B. Alers, X. Lu, J. H. Sukamoto, S. K. Kailasam, J. Reid, and G. Harm, "Ifluence of Copper Purity on Microstructure and Electromigration," *Proc. Intl. Interconnect Technology Conf.*, pp. 45–47, 2004.

[36] C. Ryu, k. W. Kwon, A. L. S. Loke, H. Lee, T. Nogami, V. M. Dubin, R. A. Kavari, G. W. Ray, and S. S. Wong, "Microstructure and Reliability of Copper Interconnects," *IEEE Trans. Electron. Dev.*, vol. 46, no. 6, pp. 1113–1120, 1999.

[37] J. Y. Kim, "Investigation on the Mechanism of Interface Electromigration in Copper Thin Films," Dissertation, The University of Texas at Arlington, 2006.

[38] Z. S. Choi, R. Mönig, and C. V. Thompson, "Dependence of the Electromigration Flux on the Crystallographic Orientations of Different Grains in Polycrystalline Copper Interconnects," *Appl. Phys. Lett.*, vol. 90, p. 241913, 2007.

[39] M. Karimi, T. Tomkowski, G. Vidali, and O. Biham, "Diffusion of Cu on Cu Surfaces," *Phys. Rev. B*, vol. 52, no. 7, pp. 5364–5374, 1995.

[40] H. Wendrock, K. Mirpuri, S. Menzel, G. Schindler, and K. Wetzig, "Correlation of Electromigration Deffects in Small Damascene Cu Interconnects with their Microstructure," *Microelectron. Eng.*, vol. 82, pp. 660–664, 2005.

[41] T. G. Koetter, H. Wendrock, H. Schuehrer, C. Wenzel, and K. Wetzig, "Relationship between Microstructure and Electromigration Damage in Unpassivated PVD Copper Damascene Interconnects," *Microelectron. Reliab.*, vol. 40, pp. 1295–1299, 2000.

[42] O. Kraft and E. Arzt, "Current Density and Line Width Effects in Electromigration: A New Damage-Based Lifetime Model," *Acta Mater.*, vol. 46, no. 11, pp. 3733–3743, 1998.

[43] C. T. W.R. Fayad, V.K. Andleigh, "Modeling of the Effects of Crystallographic Orientation on Electromigration-Limited Reliability of Interconnects with Bamboo Grain Structures," *J. Mater. Res.*, vol. 16, no. 2, pp. 413–416, 2001.

[44] M. Gall, C. Capasso, D. Jawarani, R. Hernandez, H. Kawasaki, and P. S. Ho, "Statistical Analysis of Early Failures in Electromigration," *J. Appl. Phys.*, vol. 90, no. 2, pp. 732–740, 2001.

[45] J. R. Black, "Mass Transport of Aluminum by Momentum Exchange with Conducting Electrons," *Proc. of 6th Annual Reliability Physics Symp.*, pp. 148–159, 1967.

[46] J. R. Black, "Electromigration-A Brief Survey and Some Recent Results," *IEEE Trans. Electron. Dev.*, vol. 16, no. 4, pp. 338–347, 1969.

[47] J. R. Black, "Electromigration Failure Modes in Aluminum Metallization for Semiconductor Devices," *Proc. IEEE*, vol. 57, no. 9, pp. 1578–1594, 1969.

[48] J. C. Blair, P. G. Ghate, and C. T. Haywood, "Concerning Electromigration in Thin Films," *Proc. IEEE*, vol. 59, pp. 1023–1024, 1971.

[49] G. L. Hofman and H. M. Breitling, "On the Current Density Dependence of Electromigration in Thin Films," *Proc. IEEE*, vol. 58, p. 833, 1970.

[50] M. Shatzkes and J. Lloyd, "A Model for Conductor Failure Considering Diffusion Concurrently with Electromigration Resulting in a Current Exponent of 2," *J. Appl. Phys.*, vol. 59, no. 11, pp. 3890–3893, 1986.

[51] J. Lloyd, "Electromigration Failure," *J. Appl. Phys.*, vol. 69, no. 11, pp. 7601–7604, 1991.

[52] R. Kirchheim and U. Kaeber, "Atomistic and Computer Modeling of Metallization Failure of Integrated Circuits by Electromigration," *J. Appl. Phys.*, vol. 70, no. 1, pp. 172–181, 1991.

[53] R. Kirchheim, "Stress and Electromigration in Al-Lines of Integrated Circuits," *Acta Metall. Mater.*, vol. 40, no. 2, pp. 309–323, 1992.

[54] M. A. Korhonen, P. Borgesen, K. N. Tu, and C.-Y. Li, "Stress Evolution due to Electromigration in Confined Metal Lines," *J. Appl. Phys.*, vol. 73, no. 8, pp. 3790–3799, 1993.

[55] J. J. Clement and C. V. Thompson, "Modeling Electromigration-Induced Stress Evolution in Confined Metal Lines," *J. Appl. Phys.*, vol. 78, no. 2, pp. 900–904, 1995.

[56] J. R. Lloyd, "Black's Law Revisited – Nucleation and Growth in Electromigration Failure," *Microelectron. Reliab.*, vol. 47, pp. 1468–1472, 2007.

[57] Z. S. Choi, R. Mönig, and C. V. Thompson, "Activation Energy and Prefactor for Surface Electromigration and Void Drift in Cu Interconnects," *J. Appl. Phys.*, vol. 102, p. 083509, 2007.

[58] R. S. Sorbello, "Microscopic Driving Forces for Electromigration," *Proc. Mater. Research Soc. Symp.*, vol. 427, pp. 73–81, 1996.

[59] M. E. Glicksman, *Diffusion in Solids.* John Wiley and Sons, Inc., 2000.

[60] J. R. Lloyd, "Electromigration in Thin Film Conductors," *Semicond. Sci. Technol.*, vol. 12, pp. 1177–1185, 1997.

[61] K. N. Tu, "Electromigration in Stressed Thin Films," *Phys. Rev. B*, vol. 45, no. 3, pp. 1409–1413, 1992.

[62] R. S. Sorbello, A. Lodder, and S. J. Hoving, "Finite-Cluster Description of Electromigration," *Phys. Rev. B*, vol. 25, no. 10, pp. 6178–6187, 1982.

[63] R. S. Sorbello, "Theory of the Direct Force in Electromigration," *Phys. Rev. B*, vol. 31, no. 2, pp. 798–804, 1985.

[64] P. R. Rimbey and R. S. Sorbello, "Strong-Coupling Theory for the Driving Force in Electromigration," *Phys. Rev. B*, vol. 21, no. 6, pp. 2150–2161, 1980.

[65] P. S. Ho and T. Kwok, "Electromigration in Metals," *Rep. Prog. Phys.*, vol. 52, no. 3, pp. 301–348, 1989.

[66] J. P. Dekker, A. Lodder, and J. van Ek, "Theory for the Electromigration Wind Force in Dilute Alloys," *Phys. Rev. B*, vol. 56, no. 19, pp. 12 167–12 177, 1997.

[67] A. Lodder and J. P. Dekker, "The Electromigration Force in Metallic Bulk," *Proc. of the Stress Induced Phenomena in Metallization: 4th International Workshop*, vol. 418, pp. 315–329, 1998.

[68] J. J. Clement, "Electromigration Modeling for Integrated Circuit Interconnect Reliability Analysis," *IEEE Trans. Dev. Mat. Rel.*, vol. 1, no. 1, pp. 33–42, 2001.

[69] A. S. Budiman, C. S.Hau-Riege, P. R. Besser, A. Marathe, Y.-C. Joo, N. Tamura, J. R. Patel, and W. D. Nix, "Plasticity–Amplified Diffusivity: Dislocation Cores as Fast Diffusion Paths in Cu Interconnects," *Proc. Intl. Reliability Physics Symp.*, pp. 122–127, 2007.

[70] E. G. Liniger, L. M. Gignac, C.-K. Hu, and S. Kaldor, "In Situ Study of Void Growth Kinetics in Electroplated Cu Lines," *J. Appl. Phys.*, vol. 92, no. 4, pp. 1803–1810, 2002.

[71] L. Arnaud, T. Berger, and G. Reimbold, "Evidence of Grain-Boundary Versus Interface Diffusion in Electromigration Experiments in Copper Damascene Interconnects," *J. Appl. Phys.*, vol. 93, no. 1, pp. 192–204, 2003.

[72] R. Rosenberg and M. Ohring, "Void Formation and Growth During Electromigration in Thin Films," *J. Appl. Phys.*, vol. 42, no. 13, pp. 5671–5679, 1971.

[73] J. R. Lloyd and K. P. Rodbell, "Reliability," *in Handbook of Semiconductor Interconnection Technoogy, edited by G. C. Schwartz and K. V. Srikrishnan*, pp. 471–520, 2006.

[74] J. R. Lloyd and J. J. Clement, "Electromigration in Copper Conductors," *Thin Solid Films*, vol. 262, no. 1, pp. 135–141, 1995.

[75] I. A. Blech, "Electromigration in Thin Aluminum Films on Titanium Nitride," *J. Appl. Phys.*, vol. 47, no. 4, pp. 1203–1208, 1976.

[76] I. A. Blech and C. Herring, "Stress Generation by Electromigration," *Appl. Phys. Lett.*, vol. 29, no. 3, pp. 131–133, 1976.

[77] I. A. Blech and K. L. Tai, "Measurement of Stress Gradients Generated by Electromigration," *Appl. Phys. Lett*, vol. 30, no. 8, pp. 387–389, 1977.

[78] C. Herring, "Diffusional Viscosity of a Polycrystalline Solid," *J. Appl. Phys.*, vol. 21, pp. 437–445, 1950.

[79] E. T. Ogawa, A. J. Bierwag, K.-D. Lee, H. Matsuhashi, P. R. Justinson, and *et al.*, "Direct Observation of a Critical Length Effect in Dual–Damascene Cu/Oxide Interconnects," *Appl. Phys. Lett.*, vol. 78, no. 18, pp. 2652–2645, 2001.

[80] D. Ney, X. Federspiel, V. Girault, O. Thomas, and P. Gergaud, "Stress–Induced Electromigration Backflow Effect in Copper Interconnects," *Trans. Dev. Mater. Reliab.*, vol. 6, no. 2, pp. 175–180, 2006.

[81] L. Doyen, E. Petitprez, P. Waltz, X. Federspiel, L. Arnaud, and Y. Wouters, "Extensive Analysis of Resistance Evolution due to Electromigration Induced Degradation," *J. Appl. Phys.*, vol. 104, p. 123521, 2008.

[82] A. S. Oates and M. H. Lin, "Void Nucleation and Growth Contributions to the Critical Current Density for Failure in Cu Vias," *Proc. Intl. Reliability Physics Symp.*, pp. 452–456, 2009.

[83] J. R. Lloyd, "Electromigration and Mechanical Stress," *Microelectron. Eng.*, vol. 49, pp. 51–64, 1999.

[84] R. W. Balluffi and A. V. Granato, "Dislocations, Vacancies and Interstitials," *in Dislocation in Solids, edited by F. N. R. Nabarro*, pp. 1–133, 1979.

[85] J. J. Clement, "Reliability Analysis for Encapsulated Interconnect Lines Under DC and Pulsed DC Current Using a Continuum Electromigration Transport Model," *J. Appl. Phys.*, vol. 82, no. 12, pp. 5991–6000, 1997.

[86] P. G. Shewmon, *Diffusion in Solids.* McGraw-Hill, New York, 1963.

[87] H. S. Carslaw and J. C. Jaeger, *Conduction of Heat in Solids.* Clarendon Press, Oxford, 1947.

[88] P. A. Flinn, "Mechanical Stress in VLSI Interconnections: Origins, Effects, Measurement, and Modeling," *MRS Bulletin*, pp. 70–73, 1995.

[89] R. J. Gleixner, B. M. Clemens, and W. D. Nix, "Void Nucleation in Passivated Interconnect Lines: Effects of Site Geometries, Interfaces, and Interface Flaws," *J. Mater. Res.*, vol. 12, pp. 2081–2090, 1997.

[90] G. L. Povirk, "Numerical Simulations of Electromigration and Stress-Driven Diffusion in Polycristalline Interconnects," *Proc. Mater. Research Soc. Symp.*, vol. 473, pp. 337–342, 1997.

[91] S. Rzepka, M. A. Korhonen, E. R. Weber, and C.-Y. Li, "Three-Dimensional Finite Element Simulation of Electro and Stress Migration Effects in Interconnect Lines," *Proc. Mater. Research Soc. Symp.*, vol. 473, pp. 329–335, 1997.

[92] M. E. Sarychev, Y. V. Zhitnikov, L. Borucki, C.-L. Liu, and T. M. Makhviladze, "General Model for Mechanical Stress Evolution During Electromigration," *J. Appl. Phys.*, vol. 86, no. 6, pp. 3068–3075, 1999.

[93] H. Ye, C. Basaran, and D. C. Hopkins, "Numerical Simulation of Stress Evolution During Electromigration in IC Interconnect Lines," *IEEE Trans. Compon. Pack. Technol.*, vol. 26, no. 3, pp. 673–681, 2003.

[94] M. Lin and C. Basaran, "Electromigration Induced Stress Analysis Using Fully Coupled Mechanical–Diffusion Equations with Nonlinear Material Properties," *Computational Materials Science*, vol. 34, pp. 82–98, 2005.

[95] C. Basaran and M. Lin, "Damage Mechanics of Electromigration in Microelectronics Copper Interconnects," *Intl. J. Materials and Structural Integrity*, vol. 1, pp. 16–39, 2007.

[96] R. V. Goldstein, M. E. Sarychev, D. B. Shirabaikin, A. S. Vladimirov, and Y. V. Zhitnikov, "Modeling Electromigration and the Void Nucleation in Thin-Film Interconnects of Integrated Circuits," *Intl. Journal of Fracture*, vol. 109, pp. 91–121, 2001.

[97] V. Sukharev, E. Zschech, and W. D. Nix, "A Model for Electromigration-Induced Degradation Mechanisms in Dual-Inlaid Copper Interconnects: Effect of Microstructure," *J. Appl. Phys.*, vol. 102, p. 053505, 2007.

[98] V. Sukharev, R. Choudhury, and C. W. Park, "Physically-Based Simulation of the Early and Long-Term Failures in Copper Dual-Damascene Interconnects," *Proc. Intl. Integrated Reliability Workshop*, pp. 80–85, 2003.

[99] V. Sukharev and E. Zschech, "A Model for Electromigration-Induced Degradation Mechanisms in Dual-Inlaid Copper Interconnects: Effect of Interface Bonding Strenght," *J. Appl. Phys.*, vol. 96, no. 11, pp. 6337–6343, 2004.

[100] V. Sukharev, "Physically Based Simulation of Electromigration-Induced Degradation Mechanisms in Dual-Damascene Copper Interconnects," *IEEE Trans. Computer-Aided Design of Integrated Circuits and Systems*, vol. 24, no. 9, pp. 1326–1335, 2005.

[101] D. Dalleau and K. Weide-Zaage, "Three–Dimensional Voids Simulation in Chip Metallization Structures: A Contribution to Reliability Evaluation," *Microelectron. Reliab.*, vol. 41, pp. 1625–1630, 2001.

[102] D. Dalleau, K. Weide-Zaage, and Y. Danto, "Simulation of Time Depending Void Formation in Copper, Aluminum and Tungsten Plugged Via Metallization Structures," *Microelectron. Reliab.*, vol. 43, pp. 1821–1826, 2003.

[103] P. J. Marcoux, P. P. Merchant, V. Naroditsky, and W. D. Rehder, "A New 2d Simulation Model of Electromigration," *Hewlett-Packard Journal*, pp. 79–84, 1989.

[104] J. J. Clement and J. R. Lloyd, "Numerical Investigations of the Electromigration Boundary Value Problem," *J. Appl. Phys.*, vol. 71, no. 4, pp. 1729–1731, 1992.

[105] W. D. Nix and E. Arzt, "On Void Nucleation and Growth in Metal Interconnect Lines under Electromigration Conditions," *Metall. Trans. A*, vol. 23, pp. 2007–2013, 1992.

[106] D. Hull and D. E. Rimmer, "The Growth of Grain–Boundary Voids under Stress," *Phil. Mag.*, vol. 4, pp. 673–687, 1959.

[107] J. E. Harris, "Nucleation of Creep Cavities in Magnesium," *Trans. Met. AIME*, vol. 233, pp. 1509–1516, 1965.

[108] R. Raj and M. F. Ashby, "Intergranular Fracture at Elevated Temperatures," *Acta Metall.*, vol. 23, pp. 653–666, 1975.

[109] J. P. Hirth and W. D. Nix, "Analysis of Cavity Nucleation in Solids Subjected to External and Internal Stresses," *Acta Metall.*, vol. 33, pp. 359–368, 1985.

[110] H. Ceric, R. L. de Orio, J. Cervenka, and S. Selberherr, "A Comprehensive TCAD Approach for Assessing Electromigration Reliability of Modern Interconnects," *IEEE Trans. Mat. Dev. Rel.*, vol. 9, no. 1, pp. 9–19, 2009.

[111] J. W. Christian, *The Theory of Transformations in Metal and Alloys.* 3rd ed., Pergamon, 2002.

[112] B. M. Clemens, R. J. Gleixner, and W. D. Nix, "Void Nucleation On a Contaminated Patch," *J. Mater. Res.*, vol. 12, pp. 2038–2042, 1997.

[113] S. P. Hau-Riege, "Probabilistic Immortality of Cu Damascene Interconnects," *J. Appl. Phys*, vol. 91, no. 4, pp. 2014–2022, 2002.

[114] A. V. Vairagar, S. G. Mhaisalkar, and A. Krishnamoorthy, "Electromigration Behavior of Dual-Damascene Cu Interconnects – Structure, Width, and Length Dependences," *Microelectron. Reliab.*, vol. 44, pp. 747–754, 2004.

[115] W. W. Mullins, "Mass Transport at Interfaces in Single Component Systems," *Metall. Mater. Trans. A*, vol. 26, pp. 1918–1929, 1995.

[116] D. N. Bhate, A. Kumar, and A. F. Bower, "Diffuse Interface Model for Electromigration and Stress Voiding," *J. Appl. Phys.*, vol. 87, no. 4, pp. 1712–1721, 2000.

[117] D. N. Bhate, A. F. Bower, and A. Kumar, "A Phase Field Model for Failure in Interconnect Lines due to Coupled Diffusion Mechanisms," *J. Mech. Phys. Solids*, vol. 50, pp. 2057–2083, 2002.

[118] P. S. Ho, "Motion of Inclusion Induced by a Direct Current and a Temperature Gradient," *J. Appl. Phys.*, vol. 41, no. 1, pp. 64–68, 1970.

[119] Z. Suo, W. Wang, and M. Yang, "Electromigration Instability: Transgranular Slits in Interconnects," *Appl. Phys. Lett.*, vol. 64, no. 15, pp. 1944–1946, 1994.

[120] Z. Suo and W. Wang, "Diffusive Void Bifurcation in Stressed Solid," *J. Appl. Phys.*, vol. 76, no. 6, pp. 3410–3421, 1994.

[121] W. Wang, Z. Suo, and T.-H. Hao, "A Simulation of Electromigration-Induced Transgranular Slits," *J. Appl. Phys.*, vol. 79, no. 5, pp. 2394–2403, 1996.

[122] T. V. Zaporozhets, A. M. Gusak, K. N. Tu, and S. G. Mhaisalkar, "Diffuse Interface Model for Electromigration and Stress Voiding," *J. Appl. Phys.*, vol. 98, p. 103508, 2005.

[123] D. T. Castro, R. J. O. Hoofman, J. Michelon, D. J. Gravesteijn, and C. Bruynseraede, "Void Growth Modeling upon Electromigration Stressing in Narrow Copper Lines," *J. Appl. Phys.*, vol. 102, p. 123515, 2007.

[124] E. Arzt, O. Kraft, W. D. Nix, and J. J. E. Sanchez, "Electromigration Failure by Shape Change of Voids in Bamboo Lines," *J. Appl. Phys.*, vol. 76, no. 3, pp. 1563–1571, 1994.

[125] O. Kraft and E. Arzt, "Electromigration Mechanisms in Conductor Lines: Void Shape Changes and Slit-Like Failure," *Acta Mater.*, vol. 45, no. 4, pp. 1599–1611, 1997.

[126] L. Xia, A. F. Bower, Z. Suo, and C. F. Shih, "A Finite Element Analysis of the Motion and Evolution of Voids due to Strain and Electromigration Induced Surface Diffusion," *J. Mech. Phys. Solids*, vol. 45, no. 9, pp. 1473–1493, 1997.

[127] D. R. Fridline and A. F. Bower, "Influence of Anisotropic Surface Diffusivity on Electromigration Induced Void Migration and Evolution," *J. Appl. Phys.*, vol. 85, no. 6, pp. 3168–3174, 1999.

[128] A. F. Bower and S. Shankar, "Finite Element Model of Electromigration Induced Void Nucleation, Growth and Evolution in Interconnects," *Modelling Simul. Mater. Sci. Eng.*, vol. 15, pp. 923–940, 2007.

[129] H. Ceric and S. Selberherr, "An Adaptive Grid Approach for the Simulation of Electromigration Induced Void Migration," *IEICE Trans. Electronics*, no. 3, pp. 421–426, 2002.

[130] H. Ceric and S. Selberherr, "Simulative Prediction of the Resistance Change due to Electromigration Induced Void Evolution," *Microelectron. Reliab.*, vol. 42, pp. 1457–1460, 2002.

[131] H. Ceric, R. Sabelka, S.Holzer, W.Wessner, S. Wagner, T. Grasser, and S. Selberherr, "The Evolution of the Resistance and Current Density During Electromigration," *Proc. Intl. Conf. on Simulation of Semiconductor Processes and Devices*, pp. 331–334, 2004.

[132] M. Mahadevan and R. M. Bradley, "Simulations and Theory of Electromigration-Induced Slit Formation in Unpassivated Single-Crystal Metal Lines," *Phys. Rev. B*, vol. 59, no. 16, pp. 11 037–11 046, 1999.

[133] M. Mahadevan and R. M. Bradley, "Phase Field Model of Surface Electromigration in Single Crystal Metal Thin Films," *Physica D*, vol. 126, pp. 201–213, 1999.

[134] J. A. Sethian, *Level Set Methods and Fast Marching Methods: Evolving Interfaces in Computational Geometry, Fluid Mechanics, Computer Vision and Materials Science.* Cambridge University Press, 1999.

[135] M. Khenner, A. Averbuch, M. Israeli, M. Nathan, and E. Glickman, "Level Set Modeling of Transient Electromigration Grooving," *Comp. Mater. Sci.*, vol. 20, pp. 235–250, 2001.

[136] M. Khenner, A. Averbuch, M. Israeli, and M. Nathan, "Numerical Simulation of Grain-Boundary Grooving by Level Set Method," *J. Comp. Phys.*, vol. 170, pp. 764–784, 2001.

[137] F. Cacho, V. Fiori, L. Doyen, C. Chappaz, C. Tavernier, and H. Jaouen, "Electromigration Induced Failure Mechanism: Multiphysics Model and Correlation with Experiments," *Proc. Intl. Conf. on Thermal, Mechanical and Multi-Physics Simulation and Experiments in Microelectronics and Micro-Systems*, pp. 1–6, 2008.

[138] H. Ceric, R. L. de Orio, J. Cervenka, and S. Selberherr, "Copper Microstructure Impact on Evolution of Electromigration Induced Voids," *Proc. Intl. Conf. on Simulation of Semiconductor Processes and Devices*, pp. 178–181, 2009.

[139] K. Garikipati, L. Bassman, and M. Deal, "A Lattice–Based Micromechanical Continuum Formulation for Stress–Driven Mass Transport in Polycrystalline Solids," *J. Mech. Phys. Solids*, vol. 49, pp. 1209–1237, 2001.

[140] C. K. Hu, R. Rosenberg, and K. Y. Lee, "Electromigration Path in Cu Thin-Film Lines," *Appl. Phys. Lett.*, vol. 74, no. 20, pp. 2945–2947, 1999.

[141] S. H. Rhee, Y. Du, and P. S. Ho, "Thermal Stress Characteristics of Cu/Oxide and Cu/Low-k Submicron Interconnect Structures," *J. Appl. Phys.*, vol. 93, no. 7, pp. 3926–3933, 2003.

[142] P. H. Dederichs and K. Schroeder, "Anisotropic Diffusion in Stress Fields," *Phys. Rev. B*, vol. 17, no. 6, pp. 2524–2536, 1978.

[143] C. P. Flynn, *Point Defects and Diffusion*. Clarendon Press, Oxford, 1972.

[144] D. A. Porter and K. E. Easterling, *Phase Transformations in Metals and Alloys*. Stanley Thornes (Publishers) Ltd, 2000.

[145] M. Diebel and S. T. Dunham, "Ab-*initio* Calculations to Predict Stress Effects on Defects and Diffusion in Silicon," *Proc. Intl. Conf. on Simulation of Semiconductor Processes and Devices*, pp. 147–150, 2003.

[146] C. Kittel, *Introduction to Solid State Physics*. John Wiley and Sons, Inc., 1996.

[147] H. Ceric, R. Heinzl, C. Hollauer, T. Grasser, and S. Selberherr, "Microstructure and Stress Aspects of Electromigration Modeling," *Proc. of the Stress Induced Phenomena in Metallization: 8th International Workshop*, pp. 262–268, 2006.

[148] R. W. Balluffi, "Grain Boundary Diffusion Mechanisms in Metals," *Metall. Trans. A*, vol. 13, pp. 2069–2095, 1982.

[149] J. C. Fisher, "Calculation of Diffusion Penetration Curves for Surface and Grain Boundary Diffusion," *J. Appl. Phys.*, vol. 22, no. 1, pp. 74–77, 1951.

[150] F. Lau, C. Mazure, C. Werner, and M. Orlowski, "A Model for Phosphorus Segregation at the Silicon–Silicon Dioxide Interface," *Appl. Phys. A*, vol. 49, pp. 671–675, 1989.

[151] O. C. Zienkiewicz and R. L. Taylor, *The Finite Element Method for Solid and Structural Mechanics*. Elsevier Butterworth Heinemann, 2005.

[152] C. Johnson, *Numerical Solution of Partial Differential Equations by The Finite Element Method*. Cambridge University Press, 1987.

[153] R. E. White, *An Introduction to The Finite Element Method with Applications to Nonlinear Problems*. John Wiley and Sons, Inc., 1985.

[154] P. Knabner and L. Angermann, *Numerik partieller Differential–gleichungen*. Springer, 2000.

[155] H. Ceric, "Numerical Techniques in Modern TCAD," Dissertation, Technische Universität Wien, 2005.

[156] C. Hollauer, "Modeling of Thermal Oxidation and Stress Effects," Dissertation, Technische Universität Wien, 2007.

[157] W. Li, M. Tan, and Y. Hou, "Dynamic Simulation of Electromigration in Polycrystalline Interconnect Thin Film Using Combined Monte Carlo Algorithm and Finite Element Modeling," *J. Appl. Phys.*, vol. 101, p. 104314, 2007.

[158] W. Li and M. Tan, "Enhanced Finite Element Modeling of Cu Electromigration Using Ansys and Matlab," *Microelectron. Reliab.*, vol. 47, pp. 1497–1501, 2007.

[159] L. Doyen, X. Federspiel, L. Arnaud, F. Terrier, Y. Wouters, and V. Girault, "Electromigration Multistress Pattern Technique for Copper Drift Velocity and Black's Parameters Extraction," *Proc. Intl. Integrated Reliability Workshop*, pp. 74–78, 2007.

[160] S. R. de Groot, "Theorie Phenomenologique de L'Effet Soret," *Physica*, no. 7, pp. 699–707, 1942.

[161] J.-M. Paik, H. Park, and Y.-C. Joo, "Effect of Low-k Dielectric on Stress-Induced Damage in Cu Interconnects," *Microelectron. Eng.*, vol. 71, pp. 348–357, 2004.

[162] T. Suzuki, S. O. A. Yamanoue, T. Hosoda, T. Khono, Y. Matsuoka, K. Yanai, H. Matsuyama, H. Mori, N. Shimizu, T. Nakamura, S. Sugatani, K. Shono, and H. Yagi, "Stress Induced Failure Analysis by Stress Measurements in Copper Dual Damascene Interconnects," *Proc. Intl. Interconnect Technology Conf.*, pp. 229–230, 2002.

[163] M. Y. Yan, K. N. Tu, A. V. Vairagar, S. G. Mhaisalkar, and A. Krishnamoorthy, "Confinement of Electromigration Induced Void Propagation in Cu Interconnect by a Buried Ta Diffusion Barrier Layer," *Appl. Phys. Lett.*, vol. 87, p. 261906, 2005.

[164] M. A. Meyer, M. Herrmann, E. Langer, and E. Zschech, "In Situ SEM Observation of Electromigration Phenomena in Fully Embedded Copper Interconnect Structures," *Microelectron. Eng.*, vol. 64, pp. 375–382, 2002.

[165] E. T. Ogawa, J. W. McPherson, J. A. Rosal, K. J. Dickerson, T. C. Chiu, L. Y. Tsung, M. K. Jain, T. D. Bonifiled, J. C. Ondrusek, and W. R. McKee, "Stress-Induced Voiding under Vias Connected to Wide Cu Metal Leads," *Proc. Intl. Reliability Physics Symp.*, pp. 312–321, 2002.

[166] H. Matsuyama, M. Shiozu, T. Kouno, T. Suzuki, H. Ehara, S. Otsuka, T. Hosoda, T. Nakamura, Y. Mizushima, M. Miyajima, and K. Shono, "New Degradation Phenomena of Stress-Induced Voiding Inside Via in Copper Interconnects," *Proc. Intl. Reliability Physics Symp.*, pp. 638–639, 2007.

[167] K. Yoshida, T. Fujimaki, T. Miyamoto, T. Honma, H. Kaneko, H. Nakazawa, and M. Morita, "Stress-Induced Voiding Phenomena for an Actual CMOS LSI Interconnects," *Digest Intl. Electron Devices Meeting*, pp. 753–756, 2002.

[168] M. R. Sorensen, Y. Mishin, and A. F. Voter, "Diffusion Mechanisms in Cu Grain Boundaries," *Phys. Rev. B*, vol. 62, no. 6, pp. 3658–3673, 2000.

List of Publications

[18] R. L. de Orio, H. Ceric, and S. Selberherr, "Physically Based Models of Electromigration: From Black's Equation to Modern TCAD Models", *Microelectron. Reliab.*, 2010 (in press).

[17] H. Ceric, R. L. de Orio, J. Cervenka, and S. Selberherr, "A Comprehensive TCAD Approach for Assessing Electromigration Reliability of Modern Interconnects", *IEEE Trans. Mat. Dev. Rel.*, vol. 9, no. 1, pp. 9–19, 2009.

[16] R. L. de Orio, H. Ceric, J. Cervenka, and S. Selberherr, "Analysis of Electromigration in Dual-Damascene Interconnect Structures", *J. Integrated Circuits and Systems*, vol. 4, no. 2, pp. 67–72, 2009.

[15] R. L. de Orio, H. Ceric, and S. Selberherr, "Effect of Strains on Anisotropic Material Transport in Copper Interconnect Structures under Electromigration Stress", *J. Comput. Electron.*, vol. 7, no. 3, pp. 128–131, 2008.

Oral and Poster Presentations with Proceedings:

[14] R. L. de Orio, H. Ceric, J. Cervenka, and S. Selberherr, "Electromigration Failure Development in Modern Dual-Damascene Interconnects", *Proc. Intl. Conf. on Very Large Scale Integration*, vol. 15, 5 pages, 2009.

[13] R. L. de Orio, H. Ceric, J. Cervenka, and S. Selberherr, "The effect of Copper Grain Size Statistics on the Electromigration Lifetime Distribution", *Proc. Intl. Conf. on Simulation of Semiconductor Processes and Devices*, pp. 182–185, 2009.

[12] H. Ceric, R. L. de Orio, J. Cervenka, and S. Selberherr, "Copper Microstructure Impact on Evolution of Electromigration Induced Voids", *Proc. Intl. Conf. on Simulation of Semiconductor Processes and Devices*, pp. 178–181, 2009.

[11] R. L. de Orio, H. Ceric, J. Cervenka, and S. Selberherr, "The Effect of Microstructure on Electromigration-Induced Failure Development", *Proc. Intl. Symp. on Microelectronics Technology and Devices*, pp. 345–352, 2009.

[10] R. L. de Orio, H. Ceric, J. Cervenka, and S. Selberherr, "The Effect of Microstructure on the Electromigration Lifetime Distribution", *Proc. Intl. Symp. on the Physical and Failure Analysis of Integrated Circuits*, pp. 731–734, 2009.

[9] H. Ceric, R. L. de Orio, J. Cervenka, and S. Selberherr, "The Effect of Microstructure on Electromigration Induced Voids", *Proc. Intl. Symp. on the Physical and Failure Analysis of Integrated Circuits*, pp. 694–697, 2009.

[8] H. Ceric, R. L. de Orio, J. Cervenka, and S. Selberherr, "Stress-Induced Anisotropy of Electromigration in Copper Interconnects", *Proc. of the Stress Induced Phenomena in Metallization: 10th International Workshop*, pp. 56–62, 2008.

[7] H. Ceric, R. L. de Orio, J. Cervenka, and S. Selberherr, "Analysis of Microstructure Impact on Electromigration", *Proc. Intl. Conf. on Simulation of Semiconductor Processes and Devices*, pp. 241–244, 2008.

[6] R. L. de Orio, H. Ceric, S. Carniello, and S. Selberherr, "Analysis of Electromigration in Redundant Vias", *Proc. Intl. Conf. on Simulation of Semiconductor Processes and Devices*, pp. 237–240, 2008.

[5] R. L. de Orio, S. Carniello, H. Ceric, and S. Selberherr, "Analysis of Electromigration in Dual-Damascene Interconnect Structures", *Proc. Intl. Symp. on Microelectronics Technology and Devices*, pp. 337–348, 2008.

[4] H. Ceric, R. L. de Orio, J. Cervenka, and S. Selberherr, "TCAD Solutions for Submicron Copper Interconnect", *Proc. Intl. Symp. on the Physical and Failure Analysis of Integrated Circuits*, pp. 78–81, 2008.

[3] H. Ceric, R. L. de Orio, and S. Selberherr, "Comprehensive Modeling of Electromigration Induced Interconnect Degradation Mechanisms", *Proc. Intl. Conf. on Microelectronics*, pp. 69–76, 2008.

[2] R. L. de Orio, H. Ceric, and S. Selberherr, "Strain-Induced Anisotropy of Electromigration in Copper Interconnect", *Proc. Intl. Semiconductor Device Research Symp.*, TA4-01, pp. 1–2, 2007.

[1] R. L. de Orio, H. Ceric, and S. Selberherr, "Effect of Strains on Anisotropic Material Transport in Copper Interconnect Structures under Electromigration Stress", *Proc. Intl. Workshop on Computational Electronics*, pp. 62–63, 2007.

Curriculum Vitae

April 24th, 1981
> Born in São Paulo, Brazil.

December 1999
> High school graduation as technician in electronics at Federal Technical School of São Paulo, Brazil.

January 2005
> Graduation in Electrical Engineering at State University of Campinas, Campinas, Brazil.

September 2006
> Received the degree of M.Sc. in Microelectronics from State University of Campinas.

October 2006
> Entered doctoral program at the Institute for Microelectronics, TU Wien.

May 2008 – July 2008
> Internship at Intel Corporation, Hillsboro, OR, USA.